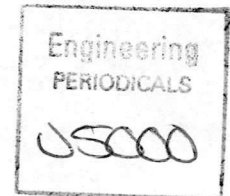# System Identification Methods for Aeroelastic Rotor Models

DRA Strategic Research Item - AS021Q18

Final Contract Report - March 1995

by

J.S.G. McVicar   S.S. Houston   D. Murray-Smith   R. Bradley

1. Introduction

This report will describe research carried out in the formulation of a strategy by which an aeroelastic rotor simulation can be validated against data measured in flight. Validation is a vital stage in the development of any model from mathematical formulation through to practical maturity as this process calibrates the fidelity of the simulation and sets boundaries to the regimes where it can be used with confidence. The progressive development of rotor models from early rotor disc to relatively recent rigid blade formulations have attracted associated induced flow models of corresponding simplicity and have been validated by established techniques (eg AGARD 1991) often based on a system identification approach. The latest generation of rotor simulations aspire to higher levels of fidelity by considering the blade aeroelastic response in conjunction with refined modelling of the rotor induced flow. The inherent complexities of such models have, until recently, precluded their development as the primary component of real time helicopter flight simulation, and consequently few are in regular use. Accordingly, techniques for their validation have not been fully developed and this situation must be rectified if such models are to yield the full benefits in fidelity which they promise. As a first stage in establishing the framework for validation, work has focused on the development of a methodology by which salient rotor states such as thrust, aerodynamic moments, blade deformations and induced flow distributions can be estimated from experimental data. These estimated states can then be validated directly against their simulated counterparts or used in the identification of, for example, blade structural parameters or elements of the induced flow model. The resulting methodology is shown in Figure 1 and this report will open by describing the strategy shown in this figure.

2. The Validation Strategy

The methodology used to gather experimental data is vital when determining the structure of any model validation strategy as the approach adopted at this stage will dictate the nature of any state estimation which has to be performed. In this project, the flight test data which will be used to support the model validation is being gathered at DRA Bedford using their Westland Lynx research vehicle. This vehicle carries an extensive range of instrumentation and a detailed description of the apparatus installed is given by Tartellin (1989). Of particular interest to this project are the two instrumented main rotor blades, one with an array of strain gauges, the Strain Gauged Blade (SGB), and the other with an array of pressure gauges, the Pressure Instrumented Blade (PIB). This chosen technique for measuring the rotor behaviour has essentially driven the validation methodology toward the structure shown in Figure 1. In fact, the work described in this report is mainly focused on

the estimation of the following rotor states from pressure and strain distributions measured using the PIB and SGB respectively:-

1. blade displacements
2. blade angle of attack distributions
3. blade thrust and moments
4. rotor induced flow distribution
5. rotor thrust and aerodynamic moments.

The techniques used in the estimation of each of these states will now be summarised in turn.

2.1 Estimation of Blade Displacements

With reference to Figure 1 it is perhaps evident that accurate estimation of the blade displacements is essential if the validation is to be performed successfully. In this strategy, blade displacements occurring in flight are estimated using the Strain Pattern Analysis (SPA) technique (Riley et al 1988) which was developed at the DRA. In this approach, the non-rotating blade is excited at the natural frequency of several modes and the strain patterns and corresponding displacements recorded - these are the calibration strain patterns and displacements. The strain distribution produced in flight is then measured and a least squares fitting technique used to ascertain the required blend of calibration strains necessary to reconstruct this measured strain distribution. The distorted blade shape is then synthesised using the same blend of modal displacements as was evaluated by the least squares fit.

2.2 Estimation of the Blade Angle of Attack Distributions

The aerodynamic contribution to the blade angle of attack is evaluated using the Incidence Indicator Method (IIM), Riley et al 1988, developed at the DRA. In this technique, look-up tables gathered from wind tunnel testing, are used to relate the pressure distribution (measured along the 2% chordline of the blade) to the corresponding aerodynamic angle of attack distribution.

The kinematic angle of attack is obtained by numeric differentiation of the blade structural displacements estimated using SPA processing.

2.3 Estimation of Rotor Induced Flow

Once the kinematic and aerodynamic angles of attack have been ascertained, the induced angle of attack an be extracted and the rotor induced flow estimated using a suitable model structure.

2.4 Estimation of Blade Thrust and Aerodynamic Moments

The thrust and aerodynamic moments generated by the instrumented blade are obtained by integration of the normal pressure distribution as depicted in Figure 1. During the course of this research project, techniques have been developed to estimate the overall rotor thrust and aerodynamic moments using measurements taken from the single pressure instrumented blade.

In order to develop the validation methodology described above (and also to establish its characteristics) a full emulation of the proposed technique was formulated. The structure of this emulation is shown in Figure 2. With reference to this figure, it is evident that the "measured" strain and pressure distributions are now generated by means of an elastic rotor model. This approach allows direct comparison between estimated and simulated rotor states and therefore provides an opportunity for a highly quantitative appraisal of the capabilities of the validation methodology. In particular, the sensitivity of the strategy to noise on the measured data can be determined, also, its ability to estimate the rotor thrust and moments from pressure measurements taken along a single blade can be assessed.

The major content of this report is contained within 4 appendices each of which describes one significant phase in the development of the full emulation shown in Figure 2. The contents of these appendices can be summarised as follows:-

Appendix 1   1. development of baseline model
                        2. development of SPA emulation.

Appendix 2   1. inclusion of aerodynamic forcing to baseline model
                        2. enhancement of SPA emulation
                        3. investigation of SPA's sensitivity to noise and strain gauge failure
                        4. development of IIM emulation
                        5. estimation of rotor induced flow field.

Appendix 3   1. estimation of rotor states from Puma flight test data.

Appendix 4   1. extension of single elastic blade model to form rotor simulation
2. inclusion of dynamic inflow modelling to the simulation model
3. development of techniques for the estimation of rotor thrust and aerodynamic moments form the pressure distribution measured along a single blade
4. development of techniques for the identification of the dynamic gains and apparent mass matrices of the Peters-HaQuang (1988) inflow model
5. estimation of rotor states form Puma flight test data and subsequent identification of the dynamic gains matrix.

A brief description of the work contained within these appendices is now provided.

3.   Emulation of the Validation Strategy

3.1   Summary of Appendix 1 - The Baseline Elastic Model and SPA Emulation

As SPA is central to the overall validation methodology, it was recognised that a simulation of SPA processing would form a good point to start the development of the full emulation shown in Figure 2. In order to support an emulation of SPA, a baseline model is formulated in Appendix 1 to generate representative displacements and strains when a spanwise and time varying force distribution is applied to a single rotating cantilever beam. These simulated displacements and strain distributions are then used as part of the SPA emulation to investigate the capability of this technique to estimate blade displacements when forcing is applied at various frequencies.

3.2   Summary of Appendix 2 - Enhancement of the Baseline Model and IIM Emulation

The next natural step toward the full emulation is the extension of the baseline model to encompass all the elements necessary to support an emulation of the IIM technique. In order to achieve this goal the following elements are added in Appendix 2 to the existing work:-

1. aerodynamic forcing is applied to the rotating blade, hence, the spanwise force distribution is now dependent on the local angle of attack
2. the baseline model now generates representative "measurements" of the pressure distribution occurring at 2% chord, C_{p02}
3. post processing routines are written in FORTRAN to estimate the kinematic contribution to the local angle of attack and to perform C_{p02} to alpha processing to emulate the IIM

4. the local angle of attack generated as a consequence of the induced flow through the rotor can now be extracted and hence the induced velocity distribution estimated.

5. the "measured" strain and pressure distributions are corrupted with noise and the influence of this noise on the quality of the estimated states is investigated

3.3 Summary of Appendix 3 - Estimation of Rotor States From Puma Flight Test Data

In order to gain confidence in the state estimation methodologies described in Sections 3.1 and 3.2, Puma flight test data are processed in Appendix 3 using the SPA and IIM emulations. In this case, blade displacements and angle of attack distributions are estimated for the Puma rotor in hover. This work reveals that the SPA and IIM emulations are capable of processing real flight test data and are therefore functioning satisfactorily. However, in this implementation, the technique used to filter noise from the blade kinematic angle of attack introduces a lag which adversely affects the estimated induced flow distribution; this problem is addressed in Appendix 4.

3.4 Summary of Appendix 4 - Completion of the Full Validation Emulation

Having successfully estimated blade displacements and angle of attack distributions using the SPA and IIM emulations derived in Appendices 1 and 2 it is now possible to complete the emulation of the full validation strategy depicted in Figure 2. Appendix 4 describes how the following items are added to the existing framework in order to achieve this objective:-

1. The single elastic blade model is enhanced to form a rotor simulation ELROT. The Peters-HaQuang inflow model is included in this algorithm to generate representative induced flow distributions

2. A technique is developed to estimate the rotor thrust and aerodynamic moments (in both trimmed and manoeuvring flight) from pressure measurements taken along a single blade

3. The FORTRAN suite of software written in Appendices 1 and 2 is restructured as part of a single autonomous MATLAB m-file, ROTEST, which performs all the state estimation shown in Figure 2. Hence, ROTEST is capable of estimating the blade displacements, angle of attack distribution, rotor induced flow distribution, rotor thrust and aerodynamic moments using pressure and strain measurements gathered from the two instrumented blades. Therefore, in its current form, ROTEST is suitable for rotor state estimation using data gathered from the flight test vehicle.

The work described in Appendix 4 demonstrates that ROTEST can be used with considerable success in the estimation of rotor states using simulated pressure and strain distributions generated by ELROT. These estimated states are subsequently used to develop a strategy by which the apparent mass and dynamic gains matrices of the Peters-HaQuang inflow model (1988) can be identified.

ROTEST is then exercised using Puma flight test data (as described in Appendix 3) and is found to produce a much better estimate to the induced flow distribution than was previously obtained. This improvement is attributed to the zero phase shift filtering now used in the estimation of the blade structural velocities.

Appendix 4 concludes by utilising the rotor states estimated from the Puma flight test data in order to identify the Peters-HaQuang dynamic gains matrix. Results from this work suggest that some inadequacy may be present in the model structure for either the induced flow distribution or for the model used to extract the induced angle of attack - it is felt that this anomaly merits further attention.

4. Development of Six Degree of Freedom System Identification Software Within the MATLAB Environment

Previous research contracts have yielded a suite of 6 DOF system software, KINEMOD (state estimation) and OUTMOD (system identificaton), written in FORTRAN. Both KINEMOD and OUTMOD have been used with considerable success at both DRA Bedford and the University of Glasgow. This software was found to incorporate a cumbersome user interface and, in light of this fact, part of the current research programme has been the development of an equivalent suite of software within the MATLAB environment. This new implementation has been written to exploit the benefits offered by the MATLAB environment and hence yield an improved user interface. The resulting software KINEMAT and FOSR has been used with some success on flight test data and, in particular, the states estimated by KINEMAT have been verified against those of KINEMOD. Furthermore, the system identification software, FOSR, is used successfully in Appendix 4 to identify the structure of the Peters-HaQuang apparent mass matrix.

A detailed description of the work carried out in the development of the 6 DOF Sytem Identification Suite is provided in Appendix 5.

5. Conclusions

Research during the course of this project has produced the following major items:-

1. A strategy for validating aeroelastic rotor models against flight test data has been established.

2. A full emulation of this strategy has been formulated and used with considerable success in the estimation of salient rotor states from simulated measurements of blade strain and pressure distributions.

3. The characteristics of the validation strategy have been investigated and its sensitivity to noise on the measured parameters established.

4. A strategy has been developed for use in the identification of the dynamic gains and apparent mass matrices of the Peters-HaQuang (1988) dynamic inflow model. This strategy has been used with considerable success using states estimated form simulated measurements within the emulation framework.

5. In its current form, the software implementation of the validation methodology, ROTEST, is capable of processing flight test data. To exercise ROTEST using experimental data, measurements taken from the Puma rotor in hover have been processed. This exercise produced consistent estimates to the rotor states and promoted confidence that ROTEST will be capable of processing data gathered from the Westland Lynx.

6. The Puma data were used to identify the Dynamic Gains matrix of the Peters-HaQuang dynamic inflow model. This work uncovered an apparent inadequacy in either the model structure of the induced flow distribution or the model structure used to estimate the induced angle of attack.

7. Six degree of freedom software has been written within the MATLAB environment. This software exploits the benefits offered by MATLAB and provides an improved user interface over that previously offered by the existing FORTRAN system identification suite.

6.   References

1.   AGARD, "Rotorcraft System Identification", Lecture Series 178, October 1991

2   Tarttelin, P. C., "Rotor Aeromechanics with the RAE Research Lynx - The Experimental Facility and Test Programme", Proceedings of the 16th European Rotorcraft Forum, Glasgow, UK, 1989

3.   Riley, J., Padfield G., Smith, J., "Estimation of Rotor Blade Incidence and Blade Deformation from the Measurement of Pressures and Strains Measured in Flight",

Proceedings of the 14th European Rotorcraft Forum, Milano, Italy, 1988

4.   Peters, D. A., HaQuang N., "Dynamic Inflow for Practical Applications", Journal of
the American Helicopter Society, Technical Note, 1988

Appendix 1

This appendix will describe work carried out in the development of the baseline elastic blade model and its subsequent use in an emulation of the SPA processing technique.

A1.1. The Baseline Elastic Blade Model

When developing the baseline model it was important to select a technique that would yield appropriate levels of modelling fidelity in order to capture the behaviour of the full simulation without incurring the penalties of prohibitive complexity. In an attempt to achieve this goal, a number of options were considered and initially the work of Houbolt and Brooks (1957) and Hodges and Dowell (1974) was investigated. These models are based on a virtual work approach and incorporate flapwise bending, chordwise bending, torsion and a spanwise blade twist distribution. High levels of modelling fidelity are therefore obtained with phenomena such as flap/torsion coupling being depicted in addition to the inclusion of realistic aerodynamic forcing. However, such high levels of fidelity are not necessary for the current application and the complexity incurred eliminates models of this type from selection as the baseline model. It was felt that a more suitable technique is exhibited in the modal approach described by Bisplinghoff (1955) whereby the displacements and strains of a rotating cantilever beam are evaluated through a weighted summation of the set of natural vibrating modes. This approach is more straightforward than that of Houbolt and Brooks (1957) and Hodges and Dowell (1974) as it only models flapwise bending and does not therefore include flap/torsion coupling. However, such a technique is suitable for supporting a SPA emulation as it does produce a set of strains and displacements in response to an applied force distribution. It was therefore decided to adopt a technique similar to that quoted by Bisplinghoff (1955) in order to model the elastic displacements produced on a forced rotating cantilever beam.

To gain confidence and familiarity in the use of this technique a simpler problem was first addressed. In this exercise, the modal approach was utilised to solve the elastic deformations produced on a non-rotating cantilever beam subject to a periodic point load. No major problems were encountered during this exercise with the results obtained being consistent and qualitatively valid - this confirmed the suitability of the modal approach for application to the baseline model. It is, however, felt inappropriate to enter into a detailed discussion of this non-rotating exercise because its derivation and all of the observations made would subsequently be repeated in the more significant rotating case.

A1.2. Evaluation of the Natural Modes for a Rotating Cantilever

The Partial Differential Equation (PDE) which describes the free vibration of a rotating cantilevered beam is given by Bisplinghoff (1955) as:-

$$EIw^{iv} + m\ddot{w} + \Omega^2 \left\{ mrw' - w'' \int_r^R m\eta \, d\eta \right\} = 0 \qquad (A1.1)$$

Equation (A1.1) is a separable PDE and therefore has a solution of the form:-

$$w(r,t) = q(t) W(r)$$

and, if one assumes that the time varying function q(t) is of the form:-

$$q(t) = A_n \, Sin(\omega_n t + \phi)$$

also, if the beam is uniform, then Equation (A1.1) becomes:-

$$EIW^{iv} - m\omega_n^2 W - \frac{m\Omega^2}{2}\left(R^2 - r^2\right)W'' + m\Omega^2 rW' = 0 \qquad (A1.2)$$

Non-dimensionalising Equation (A1.2) by putting:-

$$\psi = \frac{W}{R} \qquad \text{and} \qquad \eta = \frac{r}{R}$$

gives:-

$$\frac{d^4\psi}{d\eta^4} - \left(\frac{\omega_n}{\Omega}\right)^2 K\psi + K\eta\frac{d\psi}{d\eta} - \frac{K}{2}\left(1 - \eta^2\right)\frac{d^2\psi}{d\eta^2} = 0 \qquad (A1.3)$$

where K is the dimensionless parameter:-

$$K = \frac{m\Omega^2 R^4}{EI}$$

The deformed rotating beam can be represented by the series:-

$$\psi(\eta) = \sum_{j=1}^m \gamma_j(\eta) \xi_j$$

where:-

$\gamma_j(\eta)$ - is a trial function defining a deformed beam shape which conforms to a suitable set of boundary conditions.

ζ_j - defines the contribution of the jth trial function to the overall deformed beam shape.

Hence, Equation A1.3 now yields a characteristic equation in the following matrix form:-

$$\left(\frac{\omega_n}{\Omega}\right)^2 [m_{ij}]\{\mu_n\}=[k_{ij}]\{\mu_n\}$$ (A1.4)

where:-

$[m_{ij}]$ - is the modal mass matrix.

$[k_{ij}]$ - is the stiffness matrix.

Equation A1.4 takes the form of a classic Eigenvalue problem where the nth Eigenvalue provides the ratio of natural frequency of the nth mode to the angular velocity of the rotor. Also, the nth Eigenvector gives the relative weightings of the prescribed trial functions $\gamma(\eta)$ necessary to form the nth mode shape. Therefore the nth rotating mode shape, W_n, is given by :-

$$W_n =[\Gamma]\{\mu_n\}$$

where:-

$$[m_{ij}]=\begin{bmatrix} \gamma_1(0) & \gamma_2(0) & \cdots & \cdots & \gamma_m(0) \\ \cdots & \cdots & \cdots & \cdots & \cdots \\ \cdots & \cdots & \cdots & \cdots & \cdots \\ \cdots & \cdots & \cdots & \cdots & \cdots \\ \gamma_1(R) & \gamma_2(R) & \cdots & \cdots & \gamma_m(R) \end{bmatrix}$$

When solving Equation A1.4, suitable boundary conditions must be selected for the m trial functions and, in the case of a cantilever beam, these are:-

$\gamma(0) = 0$	zero deflection at root
$\gamma'(0) = 0$	zero slope at root
$\gamma''(R) = 0$	zero moment at tip
$\gamma'''(R) = 0$	zero shear at tip.

In the software implementation of this theory, three types of functions are available for use as trial functions:-

1) The Non-Rotating Modes
2) Duncan Trial Functions
3) Bisplinghoff Trial Function

- 14 -

where the form of the Duncan and Bisplinghoff trial functions are quoted by Bisplinghoff (1955). Essentially, the Bisplinghoff Trial functions are an extension of the Duncan Trial Functions and are formulated so that the first mode assumes a rigid body mode shape with a natural frequency $\omega_1 = \Omega$. When using either of the options 1 or 2, an iteration scheme is included to ascertain the required blade stiffness, EI, necessary to tune the natural frequency of the first mode, ω_r, to some user defined value. If the beam is configured with representative Lynx data:-

$$R = 6.4 \text{ m}$$
$$m = 6.0 \text{ kg/m}$$
$$\Omega = 35.63 \text{ rads}^{-1}$$
$$\left(\frac{\omega_1}{\Omega}\right)^2 = 1.2$$

then the converged stiffness EI is found to be 85480 Nm^2 which lies within the range of quoted spanwise values (25825 Nm^2 to 729550 Nm^2). It is therefore felt that this rotating beam model can be used to satisfactorily emulate the Lynx blade.

Using this technique, 12 trial functions have been utilised to generate the first 6 rotating mode shapes. A comparison of the modes produced when using Duncan and non-rotating modes as trial functions is given in Figure A1.1. As can be seen both sets of trial functions produce the same rotating modes and this promoted confidence that the mode shapes were being accurately evaluated. This confidence was further increased by the fact that good convergence was evident in the Eigenvectors $\{\mu\}$ when the non-rotating modes were used as trial functions, for example, the Eigenvector for the first rotating mode is given by:-

$$\{\mu_1\} = \begin{bmatrix} 0.9931 \\ 0.1141 \\ 0.0250 \\ 0.0074 \\ 0.0028 \\ 0.0012 \\ 0.0006 \\ 0.0003 \\ 0.0002 \\ 0.0001 \\ 0.0001 \\ 0.0000 \end{bmatrix}$$

It can be seen that the major contribution to this mode shape comes from the first trial function (the 1st static mode) with progressively decreasing weightings being associated with the subsequent trial functions until negligible contribution is made by the 12th trial function (or 12th static mode).

In order to investigate the orthogonality of the predicted rotating modes the modal mass matrix, m_{ij}, of the first 6 modes was investigated. This was found to be:-

$$m_{ij} = \begin{bmatrix} 0.8702 & 0.0000 & 0.0000 & 0.0000 & 0.0000 & 0.0000 \\ 0.0000 & 0.6121 & 0.0000 & 0.0000 & 0.0000 & 0.0000 \\ 0.0000 & 0.0000 & 0.7048 & 0.0000 & 0.0000 & 0.0000 \\ 0.0000 & 0.0000 & 0.0000 & 0.7444 & 0.0000 & 0.0000 \\ 0.0000 & 0.0000 & 0.0000 & 0.0000 & 0.7654 & 0.0000 \\ 0.0000 & 0.0000 & 0.0000 & 0.0000 & 0.0000 & 0.7581 \end{bmatrix}$$

As this matrix is diagonal it shows that the predicted rotating modes are orthogonal and this, in addition to the preceding observations, led to the conclusion that the first 6 rotating mode shapes had been accurately evaluated.

A1.2.2. Forced Vibrations of a Rotating Cantilever

The equation of motion for a forced uniform cantilever is an extension of its free vibration counterpart and is given by Bisplinghoff (1955) as:-

$$EIw^{iv} - m\ddot{w} - \frac{m\Omega^2}{2}\left(R^2 - r^2\right)w'' + m\Omega^2 rw' = F_z(r,t) \tag{A1.5}$$

This is again a separable PDE and the following modal approximation is used in its solution:-

$$w(r,t) = \sum_{n=1}^{\infty} q_n(t)W_n(r) \tag{A1.6}$$

with the corresponding strain distribution given by:-

$$\varepsilon(r,t) = -yw'' \tag{A1.7}$$

Where:-

$W_n(r)$ are the natural mode shapes evaluated in the preceding section.
$q_n(t)$ is a time varying parameter which weights the contribution from each natural mode.

Substituting the modal approximation into Equation A1.5 gives:-

$$mW_n \ddot{q}_n + \left\{ EIW_n^{iv} + \Omega^2 \left(mrW_n' - \frac{m}{2}(R^2 - r^2)W_n'' \right) \right\} q_n + = F_z(r,t)$$

Multiplying through by an arbitrary mode, W_m, integrating from 0 to R and remembering that W_n is the free vibration mode shape of the nth mode produces:-

$$\ddot{q}_n \int_0^R W_n W_m \, dr + \int_0^R m\omega_n^2 W_n W_m \, dr = \int_0^R W_m F_z(r,t) \, dr$$

Remembering that the natural modes are orthogonal gives:-

$$\ddot{q}_n + \omega_n^2 q_n = \frac{Q_n(t)}{M_n} \tag{A1.8}$$

where:-

The modal mass, M_n, is given by $\displaystyle\int_0^R mW_n^2 \, dr$

The modal work, Q_n, is given by $\displaystyle\int_0^R W_n F_z(r,t) \, dr$

The PDE given by Equation A1.5 has now been reduced to an Ordinary Differential Equation defining the parameter, q_n, (Equation A1.8) which weights the contribution made by the nth natural mode to the overall displacement of the beam. In the software implementation, a time history describing the modal weightings, q_n, is obtained using a Fourth Order Runge-Kutta scheme and the blade elastic displacements subsequently evaluated using Equation A1.6.

A1.3. Results Obtained Using Baseline Model

A1.3.1. Validation of the Baseline Model

To obtain a realistic validation of the baseline model, a force distribution was designed to represent the variations in lift experienced by a helicopter blade as it advances round the rotor azimuth. In order to model this effect, the forcing function consists of a spanwise increasing trapezoidal force distribution whose amplitude varies sinusoidally with time -

$$F_z(r,t) = \frac{A_{tip} r}{R} Sin(\omega_{fz} t)$$

where:-

A_{tip} is the maximum force per unit length at the blade tip

ω_{fz} is the angular velocity of the applied force.

To ascertain that the correct modes were being excited by the applied forcing, the model was forced at several frequencies, ω_{fz}, and the distorted shape investigated; some specimen results of this exercise are shown in Figures A1.2, A1.3 and A1.4. In each case the beam was forced by a maximum amplitude, A_{tip}, of 500N/m with a 0.5 second time history being portrayed at 5 evenly spaced time slices. In the first instance, the forcing was applied at 35.63 rads^{-1} as this was felt to be representative of the once per rev forcing experienced by a Lynx blade. From Figure A1.2 it can be seen that the beam distortion is mainly formed by contributions from the first mode and this is accurate because the forcing frequency is close to the natural frequency of the first mode. Figures A1.3 and A1.4, show corresponding time histories produced when the beam is forced at the natural frequency of the second and third modes respectively and, in each case, the correct mode was excited. From these results it was felt that the model was performing correctly and providing representative predictions of the elastic distortions produced on a rotating beam when acted upon by a time varying force distribution.

To further increase confidence in the model's fidelity, the beam was again forced at 35.63 rads^{-1} with a maximum amplitude of 500 N/m and now a 10 second time history of the modal weighting q_1 examined with the resulting trajectory being shown in Figure A1.5. From this figure, it can be seen that q_1 appears to 'beat' with the high frequency component having a period of approximately 0.15 seconds and this is consistent with the first mode's natural frequency of 42.756 rads^{-1}. The lower frequency 'beating' has a period of approximately 0.8 seconds and this effect is attributable to the applied forcing frequency being different to the natural frequency of vibration.

As the results obtained from these exercises were valid and explicable it was concluded that the model was performing correctly and could be used with confidence to support a SPA emulation.

A1.3.2. Strain Pattern Analysis (SPA) Emulation

In order to validate the latest generation, Level 2, simulation models it is of vital importance that the instantaneous blade angle of attack and rotor induced flow can be ascertained; an essential component of this process is the accurate determination of the deformed blade shape. One methodology which has been derived to evaluate instantaneous blade deformations is the SPA technique Riley et al (1988). Central to this methodology is that the measured strain distribution can be reconstructed from a set of calibration mode strains

measured on the non-rotating blade. The resulting relationship can the be used to recreate the distorted blade shape produced in flight. The SPA procedure is summarised by (Kosteletos 1990) as follows:-

1) Excite the natural modes of the non-rotating blade.
2) Measure the strain patterns of the non-rotating blade and the corresponding displacements (ie evaluate the calibration modes).
3) Measure the strain patterns of the rotating blade in flight.
4) Use the least-squares fitting technique to fit a linear summation of the calibration strain patterns to the strain patterns measured in flight.
5) Synthesise the shape of the rotating blade from the same linear sum of the calibration displacement patterns.

In this project, the SPA technique is emulated in the following manner:-

1) The displacements and strains for the calibration (non-rotating) modes are evaluated analytically according the standard expressions quoted by Bisplinghoff (1955).
2) The baseline model is used to generate strain distributions which represent the strain patterns measured from the rotating blade in flight.
3) The 'measured' strain pattern produced by the baseline model is reconstructed using the set of calibration strain patterns which minimised a least squares cost function.
4) The 'measured' blade shape is synthesised using the same combination of calibration mode displacements.

The emulated SPA analysis has been used to recreate several blade displacements and three examples of this are given in Figures A1.6 to A1.11. Figures A1.6 and A1.7 depict the reconstruction of the deformed shape produced at t = 0.5 seconds when the beam is subject to a forcing frequency of 35.63 rads^{-1}. The reconstructed strain distribution is shown in Figure A1.6 and it can be seen that the least squares fit has satisfactorily established the required blend of modal strains necessary to rebuild the 'measured' strain distribution. The same blend of modal displacements was then used to recreate the 'measured' blade shape and, from Figure A1.7, it is evident that the deformed shape has been accurately synthesised. Two further examples of this process are depicted in Figures A1.8 to A1.11 where the cantilever was forced at the natural frequencies of the second and third modes. From these figures it can be seen that this technique is capable of accurately synthesising 'measured' blade displacements regardless of the applied forcing frequency.

A1.4. Conclusions Drawn From Appendix 1

The research discussed in this appendix produced the following:-

1.   A strategy for validating aeroelastic rotor models has been presented. As a first stage towards realising this strategy, the requirement for a rudimentary elastic beam model capable of supporting a SPA emulation was highlighted.
2.   A baseline elastic model of a rotating cantilever beam has been developed. This model produces results which are consistent and qualitatively valid when exposed to a time varying force distribution that is representative of the forcing experienced by a helicopter blade.
3.   The baseline model has been used to satisfactorily support an emulation of the SPA technique for estimating blade deformations.

A1.5. References Used in Appendix 1

1.   Bisplinghoff, R. L., "Aeroelasticity", Addison-Wessley Publishing Company, Massachusetts, 1955

2.   Hodges, D. H., Dowell, E. H., "Nonlinear Equations of Motion for the Elastic Bending and Torsion of Twisted Nonuniform Rotor Blades", NASA Technical Note TN D-7818, December 1974

3.   Houbolt, J. C., Brooks, G. W., "Differential Equations of Motion for Combined Flapwise Bending, Chordwise Bending and Torsion of Twisted Nonuniform Rotor Blades", NACA Technical Note TN 3905, February 1957

4.   Riley, J., et al "Estimation of Rotor Blade Incidence and Blade Deformation from the Measurement of Pressures and Strains in Flight", Proceedings of the 14th European Rotorcraft Forum, Milan 1988

5.   Kosteletos, S., "The Indicator Method, the Strain Pattern Analysis Method and the RAE Bedford Research Lynx Helicopter",University of Glasgow, Department of Aerospace Engineering, Internal Report No. 9017, November 1990

Appendix 2

This appendix will describe the manner by which the elastic blade model and SPA emulation derived in Appendix 1 were developed to provide a more complete emulation of the proposed validation process. In particular the following items of research will be considered:-

1. The inclusion of aerodynamic forcing to the elastic blade model.
2. The enhancement of the SPA emulation to include a more representative spanwise distribution of "strain gauges".
3. The emulation of the Incidence Indicator method to estimate the spanwise aerodynamic angle of attack distribution.
4. The estimation of the induced flow distribution from simulated pressure and strain distributions.

A detailed description of each of these items will now be provided in turn.

A2.1. Inclusion of Aerodynamic Forcing

From Figure 2, it can be seen that the time-varying spanwise angle of attack experienced by the rotating blade is central to the proposed validation strategy. Aerodynamic forcing, specified as a function of local angle of attack, must therefore be applied to the elastic model derived in Appendix 1 if it is to produce results which are of true value in the proposed emulation. Also, if this aerodynamic forcing to be representative of that experienced by the real blade, the influence of control displacements, induced velocity and structural deformation must be considered when evaluating the angle of attack distribution. An aerodynamic forcing function containing these key elements has been devised and its derivation will now be presented.

For the purposes of subsequent modal decomposition, it is convenient to assume that $u_t \gg u_p$, therefore the local angle of attack is given by:-

$$\alpha = \frac{u_p}{u_t} + \theta$$

where the velocity component normal to the blade surface, u_p, has been approximated by:-

$$u_p = -\left\{ v_0 + \frac{r}{R}\left(v_{1c} \cos\psi + v_{1s} \sin\psi \right) + \dot{w}_n \right\}$$

$$= -\left(v_{if} + \dot{w}_n \right)$$

and the velocity component tangential to the blade surface, u_t, has been approximated by:-

$$u_t = \Omega r.$$

The blade root pitch displacement, θ, produced by inputs to the three conventional control states θ_0, θ_{1c}, θ_{1s} is given by:-

$$\theta = \theta_0 + \theta_{1c}\cos\psi + \theta_{1s}\sin\psi$$

For convenience, the lifting force has been assumed to act normal to the blade surface, therefore:-

$$F_z = \frac{1}{2}\rho Ca_0 u_t^2 \alpha$$

or:-

$$F_z = \frac{1}{2}\rho C u_t^2 a_0 \left(\frac{u_p}{u_t}+\theta\right). \tag{A2.1}$$

where a_0 is the lift curve slope for the normal force which is obtained by wind tunnel testing (Riley et al 1988) and is given in Figure A2.18.

The equation of motion describing the bending response of a forced uniform cantilever is given by Bisplinghoff (1955) and is quoted in Appendix 1 as:-

$$EIw^{iv} - m\ddot{w} - \frac{m\Omega^2}{2}\left(R^2 - r^2\right)w'' + m\Omega^2 r w' = F_z(r,t) \tag{A2.2}$$

Recalling that this is a separable Partial Differential Equation (PDE), its solution will take the form:-

$$w(r,t) = \sum_{n=1}^{\infty} q_n(t)W_n(r) \tag{A2.3}$$

hence:-

$$\dot{w}(r,t) = \sum_{n=1}^{\infty} \dot{q}_n(t)W_n(r).$$

It is now convenient to rewrite Equation A2.1 in the following form:-

$$F_z = \frac{1}{2}\rho Ca_0\left[u_t^2\left(\theta - \frac{v_{if}}{u_t}\right) - u_t\sum_{n=1}^{\infty}W_n(r)\dot{q}_n(t)\right]$$

as this can then be substituted into Equation A2.2 to give:-

- 22 -

$$\sum_{n=1}^{\infty}\left\{mW_n\ddot{q}_n+\left\{EIW_n^{iv}+\Omega^2\left(mrW_n{}'-\frac{m}{2}\left(R^2-r^2\right)W_n{}''\right)\right\}q_n+\frac{1}{2}\rho\,Ca_0\,u_t\,W_n(r)\dot{q}_n(t)\right\}$$

$$=\frac{1}{2}\rho\,Ca_0\,u_t^2\left(\theta-\frac{v_{if}}{u_t}\right).$$

Multiplying through by an arbitrary mode, W_m, integrating from 0 to R and remembering that W_n is the free vibration mode shape of the nth mode produces:-

$$\sum_{n=1}^{\infty}\left\{m\ddot{q}_n\int_0^R W_n W_m\,dr+\frac{1}{2}\rho\,C\,a_0\,\dot{q}_n\int_0^R W_n W_m\,u_t\,dr+\int_0^R m\omega_n{}^2W_n W_m\,u_t\,dr\right\}$$

$$=\frac{1}{2}\rho\,Ca_0\int_0^R W_m u_t^2\left(\theta-\frac{v_{if}}{u_t}\right)dr.$$

Recalling that the natural modes are orthogonal gives:-

$$M_n\ddot{q}_n+C_n\dot{q}_n+M_n\omega_n{}^2q_n=Q_n(t)$$

where:-

The modal mass, M_n, is given by $\int_0^R mW_n{}^2\,dr$

The modal work, Q_n, is given by $\dfrac{1}{2}\rho\,C\,a_0\int_0^R W_n\,u_t{}^2\left(\theta-\dfrac{v_{if}}{u_t}\right)dr$

the modal damping, C_n, is approximated by $\dfrac{1}{2}\rho\,C\,a_0\int_0^R W_n{}^2\,u_t\,dr$

which provides an adequate representation of the aerodynamic damping for the purposes of this simulation.

Therefore the ODE defining the modal weighting parameter, q_n, becomes:-

$$\ddot{q}_n+\frac{C_n}{M_n}\dot{q}_n+\omega_n{}^2q_n=\frac{Q_n(t)}{M_n}\,. \tag{A2.4}$$

Integration of Equation A2.4 yields the response of the of the nth modal weighting parameter, q_n, when aerodynamic forcing is applied to the cantilever. Once time histories defining these n modal weighting parameters have been obtained, subsequent application of Equation A2.3 will produce the corresponding history for the overall bending of the cantilever.

It is evident that Equation A2.4 takes a similar form to its counterpart derived Appendix 1 (Equation A1.8), where a less sophisticated force distribution was applied. However, it should be noted that a damping term, C_n, is now present, therefore, it will be possible to achieve a steady trim state when a fixed set of inputs are applied to the model.

A2.1.1. Results Produced when Aerodynamic Forcing is Applied to Elastic Cantilever Model

Before continuing with the development of the emulation, it was first necessary to establish the validity of the cantilever model when aerodynamic forcing is applied. In order to achieve such validation, the response to a wide range of inputs was appraised qualitatively and the following examples will be used to highlight the salient observations made during this exercise:-

1. 4 degrees of collective
2. 0.4 degrees of longitudinal cyclic
3. 4 degrees of collective and 5m/s uniform inflow.

A2.1.1a. Four Degrees of Collective

The response of the cantilever to a step input of 4 degrees in collective applied at t = 0 is shown in Figure A2.1. As can be seen, the beam rapidly deflects from its initial, zero deflection, condition to a new steady state of approximately 0.56m tip deflection with a small, heavily damped, overshoot to 0.60m tip deflection occurring in the first 0.10 seconds. This modelled response is felt to be representative of that exhibited by a rotating blade when a similar control input is applied. It should be noted that the presence of modal damping in Equation A2.4 has made it possible to achieve a new trim state after the control displacement is injected and this was not the case when simpler forcing was applied in Appendix 1.

Time histories of the first three modal weighting parameters, q_n, are given in Figures A2.2, A2.3 and A2.4 respectively. From these figures it is evident that the major contribution to the deformed blade shape comes from the first mode whose modal weighting in the steady state is 0.54. Progressively lesser contributions are seen to come from the higher modes until the third exerts negligible influence with a steady state modal weighting in the order of 8.0×10^{-4}. Also, the transients produced by the control input are of higher frequency as the mode number increases and this is attributable to the increasing natural frequency of these modes. Hence, the response of the cantilever (as characterised by the time histories shown in Figures A2.2, A2.3 and A2.4) is consistent with the applied forcing.

A2.1.1b. Four Degrees of Collective and 0.4 Degrees of Longitudinal Cyclic

Figure A2.5 depicts the response to a step input of 0.4 degrees in longitudinal cyclic. As in the previous case, the fundamental mode is dominant in determining the nature of this response and therefore, the time history of its modal weighting is provided in Figure A2.6. With reference to these figures it is apparent that the response again contains a heavily damped transient which decays after approximately 0.15 seconds to produce the steady state. From Figure A2.6, the frequency of oscillation in this steady state can be deduced as once per rev and this is consistent with the applied forcing. Also, the lag between root pitch displacement and maximum blade deflection is approximately 81° of azimuth and this agrees well with the 75° lag measured on the Westland Lynx. It is felt that this level of agreement is attained because the natural frequency of the fundamental mode has been tuned to provide a flap frequency ratio which is the same as that of a Lynx blade.

A2.1.1c. Four Degrees of Collective and 5m/s Uniform Inflow

Figure A2.7 depicts the bending response produced by an input of 4 degrees collective in conjunction with 5m/s uniform inflow with Figure A2.8 showing the time history for the weighting of the dominant fundamental mode. With reference to these figures it can be seen that the response is very similar to that witnessed in Section A2.1.1a, however, the steady state blade tip deflection has been reduced to 0.34m. This effect is attributable to the spanwise angle of attack having been reduced by the induced flow and is therefore qualitatively valid.

A2.2. Enhancement of SPA Emulation

The following enhancements are now made to the SPA emulation described in Appendix 1:-

1. the facility for a user defined distribution of strain gauges
2. the facility to superimpose noise on the "measured" strain distribution
3. the capability to fail one strain gauge

and each of these will now be discussed.

A2.2.1. The Inclusion of a User Defined Distribution of Strain Gauges

As defined in Appendix 1, the local strain at time, t, and spanwise location, r, is given by:-

$$\varepsilon(r,t) = -y \, w(r,t)''$$

where:-

y is the distance from the flexural axis to the fibre

and:-

$$w''(r,t)=\sum_{n=1}^{\infty} W_n''(r)q_n(t).$$

Recalling that the natural mode shapes, $W_n(r)$, are constructed using a weighted summation of trial functions, $\gamma_j(r)$, then:-

$$\varepsilon(r,t)=-y\sum_{n=1}^{\infty} q_n(t)\sum_{j=1}^{\infty} \gamma_j''(r)\zeta_j. \qquad (A2.5)$$

Hence, the strain distribution can be ascertained with minimal computational overhead because the parameters q_n, γ_j'' and ζ_j are all evaluated at earlier points in the simulation (q_n from Equation A2.4; $\gamma_j''(r)$ and ζ_j when obtaining the natural rotating mode shapes).

In the SPA emulation described in Appendix 1, the local strain was output at all spanwise locations where a value for γ_j'' was available and hence the resultant strain distribution was defined by a large set of evenly spaced "measurements". In practice, it is not possible to obtain this amount of data because only a limited number of gauges can feasibly be used to measure the strain distribution. It was therefore felt that the SPA emulation was not wholly representative of the real case and, in order to rectify this, the user should be able to position an arbitrary number of "gauges" at strategic locations along the span. This facility has been included in the software implementation by using linear interpolation on the full strain distribution given by Equation A2.5 to evaluate the strain occurring at a specified locations along the span.

The locations of the strain gauges on the instrumented Lynx blade are quoted by Tartellin (1990) as:-

Number	Radius (% span)	Radius (m)
1	3.2	0.2048
2	5.0	0.3200
3	6.8	0.4352
4	14.2	0.9088
5	17.0	1.0880
6	19.6	1.2544
7	25.0	1.6000
8	31.0	1.9840
9	41.0	2.6240
10	48.0	3.0720
11	64.0	4.0960
12	74.0	4.7360
13	85.0	5.4400
14	96.0	6.1440

Table A2.1 - Strain Gauge Locations on Instrumented Lynx Blade

The 14 strain gauges whose spanwise locations are defined by Table A2.1 have been used in the enhanced SPA emulation and the results obtained will now be discussed by means of an example.

Figures A2.9 and A2.10 depict specimen results produced by a SPA emulation which incorporates the strain gauge distribution specified by Table A2.1. The following data are shown in each of these figures:-

1. the solid line represents the actual strain/displacement distribution as it has been evaluated along the span
3. the triangles show the strain/displacement evaluated (or "measured") at each spanwise location where a strain gauge is situated
2. the crosses show the reconstructed strain/displacement at each strain gauge location.

With reference to Figure A2.9 it can be seen that the least squares cost function, described in Appendix 1, has obtained the blend of calibration modes necessary to accurately reconstruct the "measured" strain distribution. In this case the maximum error is encountered at the fourth gauge from the blade root where the reconstructed strain differs from the "measured" value by approximately 7.5%.

A comparison between synthesised and actual blade displacements is provided in Figure A2.10 and from this it is apparent that the SPA emulation has accurately recreated the deformed blade shape. However, the best level of agreement occurs towards the blade root as a slight over prediction in the reconstructed displacement becomes increasingly

visible from 3m span outwards. It is felt that this characteristic is generated as a direct consequence of the boundary conditions experienced by a rotating cantilever. Firstly, the root conditions of zero deflection and zero slope tend to produce good agreement between reconstructed and actual displacements along this portion of the blade. Secondly, the zero moment and zero shear conditions encountered at the blade tip force W'' to be approximately zero along the outboard section of the blade (in this case the tipmost 3.5m), hence, this region will deflect with constant slope. Any error in the curvature of the blade where W'' becomes small will produce an incorrect slope for the tip section and hence lead to a linearly increasing error in the displacement. However, the resulting error is small (approximately 1.5% of the actual value in this case) and it can be concluded that the SPA emulation is capable of accurately recreating distorted blade shapes using "measurements" from the distribution of strain gauges given in Table A2.1.

A2.2.1. SPA Emulation in the Presence of Noise on the "Measured" Strain Distribution

The second addition made to the SPA emulation has been the inclusion of noise on the measured strain distribution. In the software implementation, this noise takes the form of pseudo-random real numbers taken from a Gaussian distribution with a user specified mean and standard deviation (taken as a percentage of either the local or averaged strain "measured" along the span).

The affects of superimposing noise on the strain distribution are shown by the example depicted in Figures A2.11 and A2.12. In this case, the noise is represented by random numbers with a 5% standard deviation (measured relative to the local strain) and is clearly visible on the "measured" strain distribution which is no longer smooth. It is evident that the blend of calibration modes selected by the SPA emulation has produced a strain distribution which closely represents the "measured" values with only small errors occurring at all gauge locations. With reference to Figure A2.12 it can be seen that the comparison between synthesised and actual blade shape follows the same general trend as was witnessed in the previous case, that is, good agreement at the root with a linearly increasing error towards the blade tip. Hence, the most significant affect of the noise has been to change the curvature of the reconstructed blade at the point where W'' reaches zero and, by the mechanism previously described, has influenced the magnitude of error in the tip displacement. It should be noted that, in some cases, the noise can favourably affect the synthesised blade curvature and hence improve correlation at the blade tip. Hence, Figure A2.12 shows that the SPA emulation is capable of producing good approximations to the deformed blade shape when noise has been superimposed on the "measured" strain distribution.

A2.2.2. Inclusion of the Facility to Fail an Arbitrary Strain Gauge

Walker (1987) highlights that it is not possible to guarantee 100% reliability in the operation of the strain gauges, consequently, some redundancy should be present in their spanwise distribution. Hence, the pattern of strain gauges quoted in Table 1 is devised so that successful SPA processing will still be possible after any single gauge fails. Strain gauge failure has been included in the SPA emulation by setting the output of a user defined "gauge" to zero and subsequently neglecting it form the least squares fit of the calibration modes. The effect of strain gauge failure can therefore be ascertained using the SPA emulation and this is highlighted by the example provided in Figures A2.13 and A2.14 which depict the results obtained when the 4th strain gauge has failed.

From Figure A2.13, it is evident that the least squares fitting routine has established an appropriate blend of calibration modes necessary to produce good agreement with the strain distribution "measured" by the functioning gauges. However, the subsequent reconstruction of the distorted blade shape, shown in Figure A2.14, reveals that the error at the blade tip has increased from that witnessed when the full array of sensors is operating. It is also evident that an error has been introduced in the displacement predicted at the location of the 4th strain gauge and this leads to the increase in the discrepancy at the blade tip. As discussed in Section A2.2., the accuracy of the tip displacement is strongly dependant on the synthesised blade curvature at the point where the stress reduces to zero (in this case at 3m span). The failure of the 4th strain gauge has adversely affected the blade curvature at this point and consequently the prediction of the tip displacement has worsened from that produced when all gauges are operating. It should be noted that, in some cases, the failure of an inboard gauge can favourably affect the synthesised blade curvature and hence improve correlation at the blade tip.

The results produced by a SPA emulation when the 14th gauge has been failed are given in Figures A2.15 and A2.16. From these figures it can be seen that the failure of this gauge has had negligible impact on the reconstructed blade shape.

The preceding observations made in this Section are consistent with those of Walker (1987) who identifies the inboard gauges as being most significant for SPA processing. However, it has been ascertained that the effect of a single gauge failure is minimal and this supports the claim that there is redundancy in the number of gauges located along the span.

A2.3. Determination of the Kinematic Contribution to the Local Angle of Attack

The kinematic angle of attack is strongly dependant on the local velocity component produced by structural deformations of the blade as it advances round the rotor azimuth. This angle of attack is therefore a function of $\dot{w}_n(r,t)$ and is represented in the aerodynamic forcing function derived in Section A2.1 by the following expression:-

$$\alpha_{kin} = -\frac{\dot{w}_n(r,t)}{u_t(r,t)}.$$

In the validation methodology proposed in Appendix 1, SPA processing is used to synthesise a time history of blade displacements, $w_n(r,t)$, from the strain distributions measured in flight. Numeric differentiation techniques are then used to ascertain the corresponding set of structural velocity components, $\dot{w}_n(r,t)$. Hence, the kinematic contribution to the blade angle of attack can be extracted.

The method by which this process has been emulated can be seen in Figure 2. As can be seen, the "measured" strain distributions are now generated by the previously derived elastic blade model and the SPA emulation is used to reconstruct the corresponding history of blade displacements, $w_n(r,t)$. Numeric differentiation then yields the structural velocity components, $\dot{w}_n(r,t)$, from which the kinematic angle of attack is evaluated. The characteristics of this technique, particularly its sensitivity to noise, have been examined and are discussed in Section A2.6 where the capability to extract the induced flow is appraised.

A2.4. Emulation of the Incidence Indicator Method

The Incidence Indicator Method (IIM) is a technique derived to determine the blade angle of attack from data measured in flight and a detailed description is provided by Riley et al (1988). Essentially the procedure can be summarised as follows:-

1. upper surface pressure co-efficients, C_{p02}, are measured in flight at strategic locations along the 2% chord line of the blade
2. these C_{p02} data are related to the normal pressure co-efficient C_N by means of Figure A2.17
3. spanwise C_N is converted to the required angle of attack distribution through Figure A2.18.

Where the data presented in Figures A2.17 and A2.18 are obtained from wind tunnel testing and are corrected for compressibility effects. However, these data are only valid for

attached flow and therefore additional sensors are located at 90% chord to check for flow separation. The spanwise distribution of pressure sensors along the 2% chord line of the Lynx blade is given by Tartellin (1990) and is quoted in Table A2.2.

Number	Radius (% span)	Radius (m)
1	35.0	2.24
2	40.0	2.56
3	45.0	2.88
4	50.0	3.20
5	55.0	3.52
6	60.0	3.84
7	65.0	4.16
8	70.0	4.48
9	72.0	4.61
10	75.0	4.80
11	78.0	4.99
12	81.0	5.18
13	83.0	5.31
14	85.0	5.44
15	87.0	5.57
16	89.0	5.70
17	91.0	5.82
18	93.0	5.95
19	96.0	6.14
20	98.0	6.27

Table A2.2 - Pressure Gauge Locations Along 2% Chordline of Instrumented Lynx Blade

In the emulation of IIM, C_{p02} could not be "measured" directly because there is no practical analytic technique available for the evaluation of this parameter. However, the applied aerodynamic forcing, described in Section A2.2, is assumed to act normal to the blade surface, therefore, Equation A2.6 yields the radial distribution of normal pressure co-efficients:-

$$C_N = a_0 \left(\frac{u_p}{u_t} + \theta \right) \qquad \text{(A2.6)}$$

This equation is used to obtain the normal pressure co-efficient at the spanwise location of each pressure gauge, from which, application of Figure A2.17 yields the corresponding surface pressures as they would have occurred along the 2% chordline. Noise, in the form of Gaussian distributed random numbers, is superimposed on this C_{p02} data and hence the surface pressure distribution "measured" in flight has been emulated. Figures A2.17 and A2.18 are then employed in the manner described above to produce the reconstructed angle of attack.

Comparison between the actual angle of attack, $\left(\dfrac{u_p}{u_t}+\theta\right)$, and that reconstructed from the "measured" data provides useful information about the IIM's sensitivity to noise and this will now be discussed by means of an example. Figure A2.19 depicts a comparison between the reconstructed and actual angle of attack when noise with a standard deviation of 5% has been injected onto the "measured" C_{p02} distribution. As can be seen, good correlation exists between the two sets of data for the first 4m of the blade span. However, agreement degrades toward the outboard section of the blade where the effects of noise are clearly visible on the reconstructed data. It is felt that this characteristic is consistent with the nature of the compressibility correction included in Figure A2.17 where the gradient of the constant Mach Number lines is seen to steepen as Mach Number increases. This trend implies that the conversion between C_{p02} and C_N becomes more sensitive to noise as Mach Number increases and hence correlation between actual and reconstructed angle of attack deteriorates towards the outboard section of the blade. It should be noted that the maximum error is only approximately 8% of the actual value and hence the IIM is capable of satisfactorily reconstructing the angle of attack along the length of the blade span.

A2.5. Extraction of the Rotor Induced Flow

The local angle of attack is defined in Section A2.1 as:-

$$\alpha = \left(\frac{u_p}{u_t}+\theta\right)$$

or:-

$$\alpha = \theta - \frac{1}{u_t}\left(v_{if} + \sum_{n=1}^{\infty}W_n(r)\dot{q}_n(t)\right)$$

and in more convenient notation:-

$$\alpha = \theta - \frac{v_{if}}{u_t}+\alpha_{kin}.$$

Therefore, the rotor induced velocity is given by:-

$$v_{if} = u_t\,(\theta - \alpha + \alpha_{kin}) \qquad\qquad (A2.7)$$

where the kinematic and local angles of attack are extracted by the techniques described in Sections A2.3 and A2.4 respectively and the root pitch displacement is "measured" directly.

A comparison between reconstructed and actual induced flow is show in Figure A2.20. In this case, no error was injected onto the "measured" signals and the blade

displacements were reconstructed at 0.005 second time slices for use in the numeric differentiation during the evaluation of α_{kin}. With reference to Figure A2.20, it can be seen that the induced flow has been accurately reconstructed along the blade span with the small disparity present being attributable to errors associated with the numeric differentiation of the blade displacements.

Figure A2.21 depicts the correlation obtained between actual and reconstructed induced flow when noise of 5% standard deviation is injected onto the "measured" C_{p02} signal. From this figure it can be seen that the effect of the noise is most significant along the outboard region of the blade and hence the previously described trend in α has carried forward to the evaluation of induced flow. Unfortunately, the associated errors have become more significant due to the factor of u_t in the induced flow calculation (Equation A2.7). This problem is compounded by the fact that u_t increases linearly with spanwise co-ordinate, hence, the larger errors in α are biased by the greatest amount. With reference to Figure A2.21, it can be seen that the factoring of α by u_t has produced errors of up to 30% in the reconstructed induced flow near the blade tip. It is felt that errors of this magnitude may perhaps be unacceptably large, however, application of some prior knowledge of the physical characteristics of the problem can improve the levels of correlation significantly. For example, the model structure assumed in Section A2.1 produces a linear variation of induced flow with spanwise position and this knowledge can be exploited to improve agreement between the reconstructed and actual data shown in Figure A2.21. In this case, the optimum gradient and intercept of a straight line fit to the reconstructed data have been obtained by minimisation of a least squares cost function. The resultant line is plotted in Figure A2.21 and as can be seen the errors have been reduced considerably with the maximum disparity now being in the order of 2%. Hence, it can be concluded that the IIM can be used in the measurement of induced flow but the level of accuracy obtained is dependant on the application of some insight into the physical characteristics of the system. In this case, the spanwise variation of induced flow was known to be defined by a linear function whereas in the practical situation there will be no such prior knowledge of the underlying distribution and statistical means will need to be employed to determine the optimal representation.

Figure A2.22 depicts the correlation obtained between reconstructed and actual induced flow when 5% noise has been superimposed on the "measured" strain distribution. As can be seen the correct trend of linear spanwise variation is present in the reconstructed data, however, the gradient is inaccurate and this produces an error of 19% at the blade tip. This tendency is generated as a direct consequence of the manner in which the noise influences the blade shape synthesised by SPA processing. As described in Section A2.2, noise on the measured strain distribution causes SPA to synthesise an incorrect gradient

along the outboard section of the blade and therefore a linearly increasing error is produced toward the tip. Subsequent numeric differentiation will produce structural velocity components with the same characteristic and hence the resulting kinematic angle of attack will contain a linearly increasing error along the outboard section of the blade. This incorrect gradient in the kinematic angle of attack propagates through to the reconstructed induced flow by means of Equation A2.7 and hence the linearly increasing error witnessed in Figure A2.22 is produced.

A2.5.1. Filtering

A specimen time history depicting the blade tip velocity reconstructed using SPA processing and numeric differentiation is given in Figure A2.23. As can be seen, the introduction of noise onto the "measured" strain distribution has resulted in high frequency oscillations on the reconstructed blade velocity; these are responsible for the errors in induced flow depicted in Figure A2.22. To reduce the magnitude of these high frequency oscillations and their associated errors, a first order lag has been used to filter the output from the SPA processing before the numeric differentiation is performed. Various time constants in the range 5ms to 25ms have been considered in an attempt to obtain the optimal value for this parameter and the results obtained are shown in Figure A2.23. From this figure it is evident that time constants of 5ms and 10ms do not significantly reduce the amplitude of the high frequency oscillations and would therefore offer little improvement over the unfiltered case. It can also be seen that the 25ms time constant does reduce the high frequency oscillations but the associated lag is too great and would adversely effect the phasing of the reconstructed kinematic angle of attack. It was therefore concluded that the 15ms time constant represented the optimum compromise and this was subsequently used to reconstruct the kinematic angle of attack and induced flow.

A comparison between the actual and reconstructed induced flow when using a filter with a 15ms time constant is give in Figure A2.24. From this figure it can be seen that the correlation is much improved over the unfiltered case with the maximum disparity being reduced from 19% to 4%. It should be noted that the type of filtering used in the preceding discussion is specific to the emulation and may not be suitable for the real case. In the real SPA processing and the derivation of the blade velocities, there will be a similar need for some filtering in order to counteract the effect of sensor noise. At present, information regarding the assumed characteristics of the sensor noise and filter incorporated in the derivation process is unavailable so a detailed emulation of the real situation has not been possible. Hence, numeric differentiation of the synthesised blade displacements represents an adequate methodology for extracting the blade structural velocity component but some form of filtering may be required to reduce errors to an acceptable level.

A2.6. <u>Conclusions Drawn From Appendix 2</u>

The research discussed in this appendix has produced a full emulation of the proposed validation methodology and its sensitivity to noise has been established. The progress made during the course of this work can be summarised as follows:-

1. Aerodynamic forcing, dependent on a time varying and spanwise angle of attack distribution, has been applied to the existing elastic blade model.

2. The SPA emulation has been enhanced by the inclusion of the following:
    a) the facility to specify a user defined distribution of "strain gauges"
    b) the facility to inject noise on the "measured" strain distribution.

3. Numeric differentiation of the synthesised blade shapes has been used to yield the spanwise structural velocity components and hence the kinematic angle of attack distribution. This process was found to be sensitive to high frequency noise in the SPA output, however, acceptable results were obtained when a first order filter was used prior to the numeric differentiation. The filtering described in this report was specific to the emulation and may not be suitable for the real case, however, it is understood that some form of filtering will ultimately be included but its characteristics are unknown at present.

4. The Incidence Indicator Method has been emulated and its sensitivity to noise investigated. From this it was found that the IIM becomes more sensitive to noise as Mach Number increases and hence errors are biased toward the blade tip. However, with application of some prior knowledge, it is possible to satisfactorily extract the spanwise induced flow when noise is present on the "measured" pressure distribution.

5. The velocity of the induced flow has been extracted without and in the presence of noise on the "measured" data. It has been ascertained that the induced flow can be extracted using the proposed technique, however, filtering of the SPA data and prior knowledge to the form of the induced flow distribution is required if this reconstruction is to be adequately carried out in the presence of noise. In the absence of prior knowledge, it is suggested that the best order of polynomial could be obtained by statistical means.

A2.9. <u>References Used in Appendix 2</u>

1.   Bisplinghoff, R., L., "Aeroelasticity", Addison-Wessley Publishing Company, Massachusettes, 1955

2.   Riley, J., et al "Estimation of Rotor Blade Incidence and Blade Deformation from the Measurement of Pressures and Strains in Flight", Proceedings of the 14th European Rotorcraft Forum, Milan 1988

3.   Tartellin, P. C., "Rotor Aeromechanics Research with the RAE Research Lynx - the Experimental Facility and Test Program", Proceedings of the 16th European Rotorcraft Forum, Glasgow 1990

4.   Walker, A., R., "RAE Bedford Flight Research Lynx Helicopter Suggestions for SPA Transducer Positions", MS2 Technical Note ARW/08, 1987

Appendix 3

This appendix will describe results obtained when the techniques described in Appendices 1 and 2 were used to estimate the induced flow distribution produced by a Puma rotor in hover using flight test data.

From Figure 1 it is evident that the estimation of rotor induced flow from data measured in flight can be conveniently broken down into the following four stages:-

1. Estimation of the blade displacements using SPA processing
2. Estimation of the blade structural velocities by numeric differentiation of the blade displacements
3. Estimation of the blade aerodynamic angle of attack distribution using the Incidence Indicator Method
4. Estimation of the induced flow distribution

and each of these stages will now be considered in turn

A3.1. Estimation of Rotor Blade Displacements From Strain Distributions Measured Along a Puma Blade in the Hover

As discussed in Appendix 1, the measured strain distributions are processed using SPA in order to synthesise a time history of blade displacements occurring in flight. An example of this is shown in Figure A3.1 where the blade displacements produced in hovering flight have been synthesised from measured strain distributions. In this case, 3 flapping modes were used (one rigid and two elastic) as the calibration modes in the SPA processing. The elastic contribution to the deformed blade shape is evident in this figure where the influence of the second mode is clearly visible. As can be seen, the blade achieves maximum deflection toward the front of the disc and this is consistent with the applied root pitch inputs, θ, shown in Figure A3.2, where maximum pitch occurs at 90 degrees azimuth.

Despite the fact that only 5 spanwise strain gauges were installed on the Puma blade, the software is capable of satisfactorily optimising the blend of calibration modes necessary to fit the measured strain distribution. This promoted high levels of confidence that this software will be capable of accurately predicting the Lynx blade displacements when 14 spanwise gauges are present.

A3.2. Estimation of Puma Blade Structural Velocities and Kinematic Angle of Attack Distributions

Numeric differentiation of the blade displacements is used to produce a time history of the blade structural velocity component $\dot{w}$, an example of which, again for hovering flight, is shown in Figure A3.3. In this case, the influence of noise on the measured strain distribution has been filtered out using a first order lag with a 15mS time constant; the value of the time constant was selected using experience gained from work carried out using the rotating beam emulation. The blade kinematic angle of attack α_{kin} is then extracted using the expression:-

$$\alpha_{kin} = -\frac{\dot{w}}{u_t}$$

where the blade tangential velocity component u_t is measured in flight.

A3.2. Estimation of Puma Blade Aerodynamic Angle of Attack Distributions

As described in Appendix 2, the Incidence Indicator Method is used to process the measured C_{p02} pressure distribution measured in flight to yield the blade aerodynamic angle of attack, α_{aero}, distribution and an example of this is shown in Figure A3.4. As can be seen, the incidence is generally uniform over approximately 85% of the span with a high loading peak in the tip region from approximately 90 to 300 degrees azimuth. This trend is consistent with that reported by Houston and Tarttelin (1991) and is attributed to tip blade vortex interaction; the loading is reduced over the last quadrant of the rotor disc due to the proximity of the tail rotor.

A3.3. Estimation of the Puma Rotor Induced Flow Distribution

Once the blade structural velocity component and aerodynamic angle of attack distribution have been estimated from the measured data, it is then possible to ascertain the rotor induced flow using the expression:-

$$v_{if} = \mu_z - \dot{w} - u_t \left(\alpha_{aero} - \theta \right)$$

where the rotor velocity component in the local z-axis direction, μ_z, and the blade pitch inputs, θ, are measured in flight.

The estimated induced flow distribution, is shown graphically in Figure A3.5 and, as occurred in the angle of attack distribution, the surface is generally uniform with the exception of the tip region where the influence of the tip vortex is evident. The values shown agree well with those reported by Houston and Tarttelin (1991) where the induced

flow was found to vary between 15m/s to -6m/s in the hover. However, it should be noted that some longitudinal harmonic of induced flow is evident in Figure A3.5 and this was not the case for the results presented by Houston and Tartellin (1991). Such a discrepancy may be attributable to the lag introduced by the filtering process carried out during the estimation of the blade structural velocities. This problem is addressed in Appendix 4 when the filtering of the blade structural velocities is carried out by a zero phase shift Butterworth filter .

A3.4. Preliminary Identification of Rotor Induced Flow States

Once the induced flow distribution has been estimated, the optimal v_0, v_{1c}, and v_{1s} components necessary to fit the standard inflow distribution:-

$$v_{if} = v_0 + r\left(v_{1c} \cos\psi + v_{1s} \sin\psi\right)$$

are obtained by least squares minimisation. This process yielded a uniform component of 13.23m/s with lateral and longitudinal harmonics of -2.07m/s and 4.95m/s respectively producing the inflow distribution shown in Figure A3.6. The identified uniform component of inflow corresponds fairly well with the 12m/s predicted by Houston's RASCAL model. However, the longitudinal and lateral harmonics are an order of magnitude higher than those of RASCAL and consequently this requires further attention. As described previously, it is felt that this disparity may be attributable to the phase shift introduced to the estimated blade structural velocity components and this problem is addressed in Appendix 4.

Figure A3.7 shows the error surface produced by $v_{if_{recon}} - v_{if_{ident}}$ and from this it is evident that the identified distribution provides a fairly good representation to the induced flow across the uniformly loaded region of the disc. However, the model structure used in the identification cannot capture the influence of the main rotor blade vortex interaction at the blade tip and hence large errors are witnessed here. It is suggested that a statistical approach, eg Chebyshev Polynomials, could be used to identify an appropriate model structure across the whole disc.

A3.6. Conclusions Drawn from Appendix 3

In this appendix the validation technique shown in Figure 1 was successfully used to estimate rotor states from strain and pressure distributions measured along a Puma blade in the hover. The estimated induced flow distribution does however contain an unexpectedly large harmonic variation and it is suspected that this effect is attributable to the filtering technique used in the numeric differentiation for the blade structural velocities; this problem is addressed in Appendix 4.

A3.7. References Used in Appendix 3

1. Houston, S. S., Tarttelin, P. C., "Validation of Mathematical Simulations of Helicopter Vertical Response Characteristics in Hover", Journal of the American Helicopter Society, January 1991

Appendix 4

This appendix will describe work carried out in completing the emulation of the validation methodology as shown in Figure 2. In order to achieve this objectives, the work described in Appendices 1 and 2 will be developed in the following main areas:-

1. The single elastic blade model is enhanced to form a rotor simulation ELROT. The Peters-HaQuang inflow model is included in this algorithm to generate representative induced flow distributions.

2. The rotor state estimation techniques described in Appendix 2 are expanded to encompass estimation of the rotor thrust and moments from pressure measurements gathered along a single blade. The state estimation strategy, derived in Appendices 1 and 2, is now restructured as a single autonomous MATLAB m-file, ROTEST, which performs the estimation of the induced flow states in addition to the estimation of rotor thrust and moments.

3. Finally, a strategy will be developed by which the dynamic gains and apparent mass matrices of the Peters-HaQuang dynamic inflow model (Peters-HaQuang 1989) can be identified using data measured in flight. In the first instance, the identification strategy is exercised using data generated by the elastic rotor model ELROT. Once the characteristics of the strategy are established using simulated data, the Puma flight test data, discussed in Appendix 3, is revisited and the dynamic gains matrix identified.

Each of these topics will now be discussed in detail.

A4.1. Development of Elastic Rotor Model

The work described in Appendices 1 and 2 yielded a model which could predict the elastic bending response of a single rotating blade under aerodynamic forcing with a user defined induced flow distribution. This algorithm had therefore to be extended in order to generate pressure and strain distributions which could be used to identify the apparent mass and dynamic gains matrices associated with a lifting rotor.

A4.1.1. Modelling of a Rotor With n_b Blades

The first enhancement made to the existing algorithm was to model a rotor comprising n_b blades. The main effort in this task was to extend the system of $nMode$ modal equations for a single blade, given in Appendix 2, to a system of (n_b x $nMode$) equations which yield the modal weighting parameters for each blade in the rotor. This system is given below in Equation A4.1:-

$$\left(\ddot{q}_n + \frac{C_n}{M_n} \dot{q}_n + \omega_n^2 q_n = \frac{Q_n(t)}{M_n} \right)_{BlNo} \tag{A4.1}$$

where:-

the modal mass, M_n, is given by:- $\int_0^R m \, W_n^2 \, dr$

the modal work, Q_n, is given by:- $-\frac{1}{2} \rho \, C \, a_0 \int_0^R W_n \, u_t^2 \left(\theta - \frac{v_{if}}{u_t} \right) dr$

the modal damping, C_n, is given by:- $\frac{1}{2} \rho \, C \, a_0 \int_0^R u_t \, W_n^2 \, dr$

a_0 is the lift curve slope, C is the blade chord, m is the blade mass per unit length, u_t is the tangential velocity, W_n is the nth natural mode shape, θ is the blade pitch, ρ is air density, ω_n is the resonant frequency of the nth natural mode.

and:-

the subscripts n and $BlNo$ indicate the mode and blade numbers respectively.

Once the modal weighting parameters have been obtained using Equations A4.1, then the blade deformation, $w(r,t)_{BlNo}$, and structural velocity, $\dot{w}(r,t)_{BlNo}$, are yielded by the following summations:-

$$w(r,t)_{BlNo} = \sum_{n=1}^{nModes} \left\{ W_n(r) q_n(t) \right\}_{BlNo}$$

$$\dot{w}(r,t)_{BlNo} = \sum_{n=1}^{nModes} \left\{ W_n(r) \dot{q}_n(t) \right\}_{BlNo}$$

A4.1.2. Inclusion of Dynamic Inflow

In order to simulate representative induced flow distributions, the Peters - HaQuang dynamic inflow model has been included in the rotor algorithm. The full version of this model is quoted by Peters and HaQuang (1988), however, the current study is purely concerned with the hovering regime and hence the following simplified structure is appropriate:-

$$M \begin{bmatrix} \dot{v}_0 \\ \dot{v}_{1s} \\ \dot{v}_{1c} \end{bmatrix} + VL \begin{bmatrix} v_0 \\ v_{1s} \\ v_{1c} \end{bmatrix} = \begin{bmatrix} T \\ L_{mom} \\ -M_{mom} \end{bmatrix}_{aero} \tag{A4.2}$$

where, the apparent mass matrix, M, is given by:-

$$M = \begin{bmatrix} \dfrac{128}{75}\rho R^3 & 0 & 0 \\ 0 & -\dfrac{16}{45}\rho R^4 & 0 \\ 0 & 0 & -\dfrac{16}{45}\rho R^4 \end{bmatrix}$$

and, in hover, the dynamic gains matrix L, is given by:-

$$L = \begin{bmatrix} \rho\pi R^2 & 0 & 0 \\ 0 & -\dfrac{\rho\pi R^3}{2} & 0 \\ 0 & 0 & -\dfrac{\rho\pi R^3}{2} \end{bmatrix}$$

also in hover, the mass flow parameter matrix, V, is given by:-

$$V = \begin{bmatrix} v_0 & 0 & 0 \\ 0 & 2v_0 & 0 \\ 0 & 0 & 2v_0 \end{bmatrix}$$

the rotor thrust, T, is given by:-

$$T = \frac{1}{2}\rho C a_0 \sum_{BlNo=1}^{nb} \left\{ \int_0^R u_t^2\left(\theta + \frac{u_p}{u_t}\right)dr \right\}_{BlNo}$$

the rotor aerodynamic rolling moment, L_{mom}, is given by:-

$$L_{mom} = -\frac{1}{2}\rho C a_0 \sum_{BlNO=1}^{nb} \left\{ Sin\psi \int_0^R u_t^2\left(\theta + \frac{u_p}{u_t}\right)dr \right\}_{BlNo}$$

the rotor aerodynamic pitching moment, M_{mom}, is given by:-

$$M_{mom} = -\frac{1}{2}\rho C a_0 \sum_{BlNo=1}^{nb} \left\{ Cos\psi \int_0^R u_t^2\left(\theta + \frac{u_p}{u_t}\right)dr \right\}_{BlNo}$$

and:-

R is the blade radius, v_0 is the uniform induced flow component, v_{1s} and v_{1c} are the harmonics of induced flow.

The rotor model defined in the preceding sections has been implemented in the form of a FORTRAN program, ELROT, and run on a DEC ALPHA. In this

- 43 -

implementation, the evaluation of the blade modal weighting parameters and rotor induced flow states has been simplified by decoupling the integration of Equations A4.1 form that of Equation A4.2. More specifically, an Euler integration scheme is used to update the induced flow states at the start of each time step. The induced flow is then held constant for the duration of the time step whilst the Runge-Kutta scheme integrates the modal equations of each blade in turn.

A4.1.3. Validation of the Elastic Rotor Model ELROT

The main role for ELROT is to produce representative data from which a strategy can be developed to identify the apparent mass and dynamic gain matrices. Consequently, ELROT is not formulated with the main intention of attaining high levels of fidelity, however, it was felt that some limited validation was appropriate to ensure that realistic results were being produced. In order to obtain a quantitative validation, HELISTAB was used to produce a hovering trim state for the Westland Lynx and the resulting control inputs (θ_o =0.246 rad, θ_{1s} = -0.0033 rad, θ_{1c} = 0.00472 rad) used to drive the standalone ELROT. A comparison was then made between the predicted rotor induced flow, thrust and equivalent flap angle producing the following results:-

Parameter	HELISTAB	ELROT
thrust	42186 N	45652 N
v_0	12.80 m/s	12.02 m/s
flap angle	0.050 rad	0.059 rad

Table A4.1 Comparison Between ELROT and HELISTAB

With reference to Table A4.1 it is evident that ELROT has produced very good agreement with HELISTAB for all quoted parameters. It can therefore be concluded that the model is functioning satisfactorily for the purposes of the current research project.

A4.2. Development of a Strategy for the Identification of the Apparent Mass and Dynamic Gains Matrices

When developing this strategy, ELROT was configured with Westland Lynx data and used to generate representative "measurements" of pressure and strain distributions produced by the "instrumented" blades. When using ELROT, the user can select any of the blades to carry the pressure or strain gauges respectively, in the following examples both sets of instruments have been placed on the same blade. A useful item of future work would be to investigate the ability of the strategy to identify the L and M matrices when the strain and pressure gauges are placed on opposing sides of the azimuth; as is the case with the real vehicle.

Before the identification of the apparent mass and dynamic gains matrices can be carried out, it is first necessary to estimate the rotor induced velocity, thrust and moments from the measured data; this will now be discussed.

A4.2.1. Estimation of Rotor Induced Flow Distribution

A detailed description of the technique used to estimate the rotor induced flow distribution, v_{if}, is provided in Appendix 2. Essentially, the induced flow distribution is estimated by means of the following expression:-

$$v_{if}(r,t) = \dot{w}(r,t) - u_t(r)\{\theta(r,t) - \alpha(r,t)\} \tag{A4.3}$$

where:-

$\dot{w}(r,t)$ is obtained by SPA processing (Riley et al 1988) of the measured strain distribution (which yields the blade deformations) followed by numeric differentiation.

$u_t(r)$ is extracted directly from the data measured by the HADS system on the vehicle.

$\alpha(r,t)$ is obtained by IIM processing (Riley et al 1988) of the measured pressure distribution, C_{p02}, using look-up tables formed by wind tunnel testing.

The state estimation technique described above was used with some success to extract induced flow distributions from measured Puma data in Appendix 3. However, this earlier work was implemented as a suite of FORTRAN programs which was cumbersome to use. Also, as described in Appendix 3, the approach used to filter the effects of noise from the blade structural velocity introduced a lag which adversely affected the estimated induced flow. Hence, a new implementation was written in the form of a single MATLAB m-file, ROTEST, and a zero phase shift filter used in the numeric differentiation for the structural velocity. This approach has yielded much improved results over the original implementation as will be shown in Section A4.3.3 where state estimation of the salient rotor states is performed using data measured from the Puma in hover.

A4.2.2. Estimation of Rotor Induced Flow Components

Once the estimation of v_{if} has been performed, it is then necessary to extract the components v_0, v_{1s} and v_{1c} from the resulting distribution which, for the Peters-HaQuang model, takes the standard form:-

$$v_{if} = v_0 + \frac{r}{R}\left(v_{1s}Sin\psi + v_{1c}Cos\psi\right).$$

Ideally, one would estimate values for v_0, v_{1s} and v_{1c} at each azimuthal location, however, with reference to the preceding equation, it is apparent that this is not possible. In fact only v_0 and the gradient, $(v_{1s}Sin\psi + v_{1c}Cos\psi)$, can be uniquely estimated at any given azimuthal location, hence, some compromise is necessary. The solution adopted was to perform the estimation at 0, 90, 180, and 270 degrees azimuth where:-

at 0 and 180 degrees v_0 and v_{1c} are estimated
at 90 and 270 degrees v_0 and v_{1s} are estimated.

Subsequent interpolation yields an estimate to the parameters at each azimuthal location.

A4.2.3. Estimation of Rotor Thrust and Moments

The thrust and aerodynamic moments produced by the instrumented blade are obtained by integration of the normal pressure distribution, C_N:-

$$\left. \begin{aligned} T(\psi) &= \frac{1}{2}\rho C\Omega^2 \int_{eR}^{R} r^2 C_N Cos\beta Cos\theta \ dr \\ L_{mom}(\psi) &= -\frac{1}{2}\rho C\Omega^2 Sin\psi \int_{eR}^{R} r^3 C_N Cos\beta Cos\theta \ dr \\ M_{mom}(\psi) &= -\frac{1}{2}\rho C\Omega^2 Cos\psi \int_{eR}^{R} r^3 C_N Cos\beta Cos\theta \ dr \end{aligned} \right\} \qquad \text{(A4.4)}$$

where:-

C_N is obtained from the measured C_{p02} distribution by means of a look up table
β is the local equivalent flapping angle
θ is the blade root pitch input.

For a trimmed rotor with identical blades, each blade will generate the same contribution to the rotor forces and moments as it passes through any arbitrary azimuthal position, ψ. Hence, pressure data gathered from the instrumented blade, when used in conjunction with Equations A4.4, will yield a complete description of the thrust/moments generated by the trimmed blades as they advance round the rotor azimuth. This description, expressed in terms of a 1-dimensional look up table, could therefore be used to estimate the overall thrust/moments produced by the trimmed rotor. The states estimated from the trimmed rotor could then be used in the identification of the dynamic gains matrix, L. The current research is however, also concerned with the identification of the apparent mass

matrix, M, and it is therefore necessary to estimate the rotor thrust and moments during transient responses.

By definition, it is apparent that the transient forces/moments produced by the blades at a given azimuthal location will not be constant with time. Hence, the 1-dimensional look up table described above would be inappropriate for state estimation in this regime. Now the thrust/moments evaluated for the instrumented blade are expressed in the form of 2-dimensional look up tables with ordinates of ψ (expressed in the range 0 to 2π) and time. (When forming these tables, the raw data gathered from the instrumented pressure blade are interpolated onto a uniform grid of azimuth and time using cubic interpolation). At each time frame, these look up tables are used to ascertain the thrust/moments produced by each individual blade at the prescribed time and azimuthal co-ordinates. The overall rotor thrust/moment is then obtained by summing the contribution from each blade.

The rotor state estimation techniques described in this section have been implemented as part of ROTEST and resulting software exercised using simulated data. The observations made during the course of this work will now be discussed.

A4.2.4. Validation of Rotor State Estimation Methodology

Validation of ROTEST has been achieved by estimating rotor states from a range of 'measured' pressure and strain distributions simulated by ELROT. The results of this exercise are best highlighted by means of the following three examples.

A4.2.4a. Trimmed rotor in hover ($\theta_0 = 0.215$ rad, $\theta_{1s} = \theta_{1c} = 0.009$ rad)

Figure A4.1 shows a comparison between the time histories of simulated and estimated induced flow states, from this figure , it can be seen that correlation between the two sets of signals is excellent. The time histories for estimated and simulated v_0 are coincident, however, a small disparity is present between the traces for the harmonic states. In particular, the estimated states do not display the n_b per rev oscillations present on the simulated data, in fact, a lower frequency oscillation is evident on the estimated time histories. It is felt that this feature is attributable to the fact that v_{1s} and v_{1c} are only directly estimated every 180 degrees of rotor azimuth with interpolation being used to complete the time histories (as described in Section A4.2.2). This technique will tend to filter out the higher frequency oscillations and produce records of the type shown in Figure A4.1. It should be noted however that the maximum error between the two sets is approximately 0.01% of the mean value and can be considered as negligible.

The look up tables of blade forces and moments obtained from the pressure instrumented blade are shown graphically in Figures A4.2, A4.3 and A4.4. From these figures, the periodic oscillations in the blade thrust and moments round the rotor azimuth are clearly visible. Also, as this is a trimmed example, the forces/moments produced at each azimuthal location are constant with time.

A comparison between the simulated and estimated rotor thrust and moments is provided in Figure A4.5. N_b per rev oscillations on both the simulated and estimated time histories are clearly visible in this figure. Also, it is evident that the estimation software has accurately established the rotor thrust and moments with errors of considerably less than 1% being present between the simulated and estimated histories. In all cases this disparity is manifest in the underprediction of the estimated time histories and it is felt that this feature is attributable to the fact that the pressure distribution is measured at only 14 spanwise locations. The subsequent trapezoidal integration of this measured distribution leads to the witnessed underestimation of the rotor thrust/moments. (It should be noted that the outermost pressure gauge is located at 96% blade radius, hence, the pressure distribution along the most heavily loaded 4% of the span is unmeasured and this could lead to a significant underprediction of the blade forces and moments. To reduce this problem, the measured data has been extrapolated to zero at the blade tip before the integration is performed).

A4.2.4b Rotor in hover with 10% step input applied to collective
(125mS lag between stick displacement and blade pitch input)

Figure A4.6 shows a comparison between the time histories for simulated and estimated induced flow states. With reference to this figure it can be seen that correlation is excellent with both sets of signals being coincident for all 3 states.

The look up tables of blade forces and moments produced when a step input is applied to the collective are shown in Figures A4.7, A4.8 and A4.9 and, in each of these figures, the effect of the control perturbation is clearly visible.

A comparison between the simulated and estimated rotor forces and moments is provided in Figure A4.10. From this figure, it is evident that a reasonably good estimate has been established to the steady state thrust/moments before and after the control perturbation is applied. However, the estimated transients poorly replicate the simulated response with the thrust being smeared relative to the measured signal and the moments containing large oscillations (approximately 40% of the mean value) which are not present in the measured signals. Primarily, the transients are poorly estimated because the look up tables for blade thrust/moments are formed using data measured from a single blade.

Hence, the table entries made at each azimuthal location are updated at the rate of once per rev and this leads to a relatively coarse time grid (for the Lynx there is approximately 0.176 seconds between time points). Rapid variations in blade thrust/moments (such as occur with the step input) are not accurately captured by interpolation from these look up tables, hence, the rotor transient behaviour is poorly estimated.

One solution to this problem would be to structure the look-up tables with a finer time grid, ie, the thrust and moments produced at each azimuthal station would have to be updated more frequently. Such an approach would require the instrumentation of more blades or a faster rotor speed - both of which are impractical. It is therefore felt that this estimation technique is best restricted to responses which contain only slow transients; an example of this is described in the following section where a ramp input is considered.

A4.2.4c. Rotor in hover with 10% ramp input applied to collective over 2 seconds (125mS lag between stick displacement and blade pitch input)

Figure A4.11 shows a comparison between the time histories for simulated and estimated induced flow states. With reference to this figure it can be seen that correlation is again excellent with both signals being coincident for all 3 states.

The look up tables of blade thrust and moments produced when a ramp input is applied to collective are shown in Figures A4.12, A4.13 and A4.14 and, in each of these figures, the effect of the control displacement is clearly visible.

A comparison between estimated and simulated rotor thrust/moments is provided in Figure A4.15. From this figure it can be seen that correlation between the estimated and simulated data is now much improved over that obtained for the step input. The estimated rotor thrust is now virtually coincident with the simulated response. However, the estimated rotor moments still demonstrate a visible oscillation as the initial control movement is applied but the resulting error has been greatly reduced (now approximately 2.5% of the mean value). It is therefore felt that these estimated states would be acceptable for use in subsequent parameter estimation.

A4.2.5. Identification of Dynamic Gains and Apparent Mass Matrices

The model structure for the Peters-HaQuang dynamic inflow model given in Equation A4.2 can be expressed more conveniently as:-

$$\dot{\lambda} = M^{-1}\{\mathbf{f} - VL\lambda\} \qquad \text{(A4.5)}$$

where:-

$\mathbf{f}$ is the vector of thrust and aerodynamic moments, λ is the vector of induced flow states.

When identifying the L and M matrices in the above equation it was elected to adopt a two phase approach. In the first instance, the L matrix is identified using data estimated from a steady trim where $\dot{\lambda} \approx 0$, consequently:-

$$L\lambda = V^{-1}\mathbf{f}. \tag{A4.6}$$

The L matrix is identified by obtaining an analytic least squares solution to Equation A4.6.

In the second phase, each row of the M matrix is identified in turn using states estimated from time histories measured when appropriate control perturbations are applied to the rotor (i.e. collective perturbations for row 1, lateral cyclic perturbations for row 2, longitudinal cyclic perturbations for row 3). In each case, the L matrix identified in Phase 1 is substituted into Equation A4.5 and a time domain OSR (Padfield et al 1987) approach adopted to identify the row of the M matrix.

In order to test the proposed strategy, the rotor states estimated from simulated data (described in the preceding sections) were used to identify the L and M matrices and the results obtained from this exercise will now be discussed.

A4.2.5a. Identification of L matrix using data estimated from a trimmed rotor in hover

The rotor inflow and thrust/moments estimated in Section A4.2.4a were employed in Phase 1 of the identification strategy and the following L matrix was obtained:-

$$L_{ident} = \begin{bmatrix} 314.00 & -3.12 & 2.63 \\ 28.35 & 19.37 & -19.28 \\ -22.98 & -8.41 & 2.27 \end{bmatrix}$$

where the L matrix input to the simulation ELROT was:-

$$L_{sim} = \begin{bmatrix} 315.5 & 0.0 & 0.0 \\ 0.0 & -504.7 & 0.0 \\ 0.0 & 0.0 & -504.7 \end{bmatrix}.$$

As can be seen the top row of the matrix, that is the terms which relate the rotor thrust to the induced flow states, has been accurately identified. However, the rows which correspond to the rotor rolling and pitching moments are poorly identified. It is felt that this problem is attributable to the fact that the harmonics of induced flow are strongly linearly dependent, hence, the optimisation scheme is ill-conditioned which results in the poor

solution. In order to investigate this, a diagonal structure was assumed for the L matrix and the optimisation repeated producing the following result:-

$$L_{ident} = \begin{bmatrix} 314.29 & 0.0 & 0.0 \\ 0.0 & -503.83 & 0.0 \\ 0.0 & 0.0 & -505.68 \end{bmatrix}.$$

It is evident that, the L matrix has now been accurately identified with negligible errors (less than 1%) being present in all of the states.

A4.2.5b. Identification of the M matrix using data estimated from a rotor in
        hover using ramp inputs to the control states

Having successfully identified the diagonal dynamic gains matrix, it is now possible to focus on the apparent mass matrix M using Phase 2 of the identification strategy. As ROTEST is capable of estimating the rotor thrust/moments with greatest accuracy when ramp inputs are applied, it was decided to use ramp inputs in the identification of M. In this example, 10% ramps were applied over 2 seconds to each of the control states in turn, the apparent mass matrix was then identified row by row as described in Section A4.2.5. The following apparent mass matrix was produced:-

$$M_{ident} = \begin{bmatrix} 598.8 & 641.6 & 271.4 \\ 418.4 & -692.0 & 4608.5 \\ 345.1 & -2060.7 & -642.0 \end{bmatrix}$$

where the corresponding matrix input to the simulation was:-

$$M_{sim} = \begin{bmatrix} 548.32 & 0.00 & 0.00 \\ 0.00 & -731.10 & 0.00 \\ 0.00 & 0.00 & -731.10 \end{bmatrix}.$$

As can seen, the diagonal elements of M have been accurately identified with errors of approximately 10% being associated with each of these states. The off-diagonal elements are, unfortunately, poorly identified and it is felt that this problem is attributable to strong linear dependence between rotor states. However, the OSR software does recognise that the diagonal elements form the most significant contribution to the model structure as the following table of F-ratios suggests:-

F-ratios for row 1	1689313.0	29408.0	66902.0
F-ratios for row 2	0.7	27761.4	2609.3
F-ratios for row 3	51.0	1358.9	47560.3

Table A4.2 - F-ratios produced during the identification of M

If one assumes a diagonal structure for the apparent mass matrix and repeats the identification process then the following matrix is obtained:-

$$M_{ident} = \begin{bmatrix} 543.9 & 0.00 & 0.00 \\ 0.00 & -711.43 & 0.00 \\ 0.00 & 0.00 & -683.9 \end{bmatrix}.$$

It is now evident that the apparent mass matrix has been accurately identified with all parameters being established to within 4% of the theoretical values originally input to the simulation.

Having, successfully tested the estimation and identification software using simulated 'measured' data it was decided to apply this software to flight test data. In fact, the Puma hover data was revisited (Event 18a of Flight 797) using the state estimation software, ROTEST, and Phase 1 of the identification strategy to identify the L matrix.

A4.3.   Identification of the L Matrix from Puma Hovering Data

The first stage in the identification process is to estimate the induced flow distribution, v_{if}, from the measured pressure and strain distributions. As stated previously, estimation of the rotor induced flow, thrust and moments is now performed in the MATLAB environment by ROTEST. The improved filtering techniques incorporated in ROTEST have led to a significant improvement in the estimate of the induced flow distribution and this will now be highlighted by means of the Puma hover data.

The estimation of v_{if} can be conveniently broken down into 3 stages:-

1. Estimation of normal pressure distribution C_n
2. Estimation of angle of attack distribution α
3. Estimation of induced flow distribution, v_{if}, using Equation A4.2

each of these stages will now be considered in turn.

A4.3.1. Estimation of Puma Blade Normal Pressure Distribution, C_n

C_n is estimated from the pressure distribution measured at 2% chord, Cp_{02}, using a look-up table compiled from wind tunnel testing (Riley et al 1988). Figure A4.16 shows the estimated C_n distribution, in this figure the extent of the uniformly loaded section of the blade is clearly visible with the effect of the main rotor vortex being apparent at the blade tip. Figure A4.17 gives the spanwise variation in C_n averaged round the rotor disc and this shows excellent agreement with that provided by Tarttelin (1989). Hence it can be concluded that the software is functioning correctly in the estimation of the C_n distribution.

A4.3.2. Estimation of Puma Blade Angle of Attack Distribution, a

The angle of attack distribution is now established by means of a look up table relating C_n to α. Figure A4.18 depicts the angle of attack distribution estimated in this case, again the effect of the main rotor vortex is apparent at the blade tip. The distribution shown in this figure correlates well with that of Tarttelin (1989) and hence it can be concluded that α has been accurately estimated.

A4.3.3. Estimation of Puma Rotor Induced Flow Distribution, v_{if}

As stated in Section A4.2.1 the induced flow distribution is estimated by means of Equation A4.3. The structural velocity component in this equation is established by numeric differentiation of the blade structural deformations (obtained by SPA processing). In the previous FORTRAN implementation, the filtering used during this differentiation produced a lag in the blade structural velocity component which in turn generated an error in the estimated induced flow distribution (as described in Appendix 3). In the new MATLAB implementation, a fourth order, two pass Butterworth filter is employed during the differentiation and hence no lag is associated with the structural velocity component.

The angle of attack distribution and blade structural velocities are now input to Equation A4.3 yielding the induced flow distribution shown in Figure A4.19. As can be seen, the distribution does not exhibit a large harmonic variation of induced flow in the uniformly loaded region as was the problem in the earlier work described in Appendix 3. This improvement is attributable to the zero phase shift filtering employed during the numeric differentiation of the blade deformations. Also, the magnitude of this induced flow distribution now bears good correlation with that of Tarttelin (1989) in both the uniformly loaded and tip regions of the blade, this is shown in Table A4.3:-

	Uniform Region	Tip Region
Previous Work (Appendix 3)	20 ms^{-1}	-2 ms^{-1}
Current Work	16.5 ms^{-1}	-7.5 ms^{-1}
Tarttelin (1989)	15.1 ms^{-1}	-6.2 ms^{-1}

Table A4.3 - Comparison of Estimated Induced Flow Distributions

It is evident from the preceding discussion that the current work has produced a considerably more accurate estimate of the induced flow distribution than was previously in Appendix 3. In fact, correlation with Tarttelin (1989) is now very good and this promotes confidence that the new implementation is functioning correctly.

Having estimated the induced flow distribution it is now necessary to identify the uniform and harmonic states v_0, v_{1s} and v_{1c}.

A4.3.4. Estimation of Puma Induced Flow States v_0, v_{1s} and v_{1c}

The technique proposed in Section A4.2.2a for identification of the induced flow states did not function well when applied to the induced flow distribution estimated from flight test data. In particular the harmonic components were found to alternate between positive and negative values as the rotor advances round the azimuth. This problem is attributable to the fact that, as shown in Figure A4.20, the spanwise gradient associated with the induced flow distribution is positive round the whole disc. In order to accommodate this positive gradient the harmonic states v_{1c} and v_{1s} must change sign as $Cos\psi$ and $Sin\psi$ respectively move between quadrants, hence, the harmonic components toggle between positive and negative values.

It is felt that this positive spanwise gradient can most probably be accounted for by either:-

1.   an unmodelled effect in the evaluation of the blade pitch, θ. It is estimated that a more favourable induced flow distribution would be estimated if an additional harmonic variation of approximately 0.35 degrees per metre were present in θ. The strongest candidate for providing a variation of this type is the fundamental mode of elastic torsion and this could merit further attention.

2.   a physical effect not included in the model structure defining the induced flow distribution. The positive spanwise gradient seen in Figure A4.20 is unmodelled by the model structure quoted in Section A4.2.2 however it is possible that this effect is physically

- 54 -

present in the induced flow distribution associated with the real rotor (at least in hover). It is suggested that a model structure of the form:-

$$v_{if} = v_0 + \frac{r}{R}\left(v_{sv} + v_{1s}Sin\psi + v_{1c}Cos\psi\right).$$

where

v_{sv} models the constant spanwise gradient in the induced flow.

could be more appropriate in modelling the induced flow distribution. This again merits further attention.

In order to continue with the identification of the L matrix it is necessary to obtain a representative estimate to the inflow states forming the model structure quoted in Section A4.2.2. This was achieved by obtaining harmonic inflow components which provided an optimal least squares fit to the distribution (across the uniformly loaded section of the blade span) round 1 complete turn of the rotor and the following parameters were obtained:-

$$v_0 = 12.6\text{ms}^{-1} \quad , \quad v_{1s} = -2.57\text{ms}^{-1} \quad , \quad v_{1c} = -0.38\text{ms}^{-1}.$$

It is felt that the v_0 and v_{1c} components quoted above are qualitatively valid, however, v_{1s} appears unexpectedly large and this may well adversely affect the identification of the L matrix.

A4.3.5. Estimation of Puma Rotor Thrust and Moments

The rotor thrust and moments were estimated using the strategy described in Section A4.2.3 with the results obtained being shown graphically in Figure A4.21. The forces and moments averaged round 1 revolution of the rotor are given by:-

$$T = 58117\text{N} \quad , \quad L = 2168\text{Nm} \quad , \quad M = 10494\text{Nm}.$$

The figure quoted above for the rotor thrust closely matches that of Tarttelin (1989) where the derived rotor thrust is quoted as 57517N, the aerodynamic pitching and rolling moments appear qualitatively consistent with the applied cyclic inputs of $\theta_{1s} = 1.896$ degrees and $\theta_{1c} = 0.532$ degrees.

A4.3.6. Identification of the L matrix

In this case the estimated rotor states are expressed as single values and not time histories, therefore, the identification of the diagonal L matrix is performed by solving the following algebraic relationships:-

$$L_{11} = V_{11}^{-1} \mathbf{f_1} v_0^{-1}$$
$$L_{22} = V_{22}^{-1} \mathbf{f_2} v_{1s}^{-1}$$
$$L_{33} = V_{33}^{-1} \mathbf{f_3} v_{1c}^{-1}$$

which yield the following L matrix:-

$$L = \begin{bmatrix} 374.5 & 0.0 & 0.0 \\ 0.0 & -33.8 & 0.0 \\ 0.0 & 0.0 & 1094.5 \end{bmatrix}.$$

For the Puma in hover, the theoretical L matrix is given by:-

$$L = \begin{bmatrix} 432.93 & 0.0 & 0.0 \\ 0.0 & -811.53 & 0.0 \\ 0.0 & 0.0 & -811.53 \end{bmatrix}.$$

It can be seen that a reasonably good approximation to the L_{11} element has been achieved with an error of approximately 13.5% being present in this state, however, L_{22} and L_{33} poorly correlate with the theoretical values. This is most probably attributable to the estimation of the harmonic inflow states which, as described above, are suspected to contain errors.

A4.4.   Conclusions Drawn from Appendix 4

The research described in this Appendix has produced a strategy by which the dynamic gains and apparent mass matrices can be identified. During the course of this work the following have been achieved:-

1.   The single elastic blade simulation developed in Appendices 1 and 2 has been expanded into the form of a rotor model which includes Peters-HaQuang dynamic inflow modelling.

2.   Data (based on the Westland Lynx) simulated by the elastic rotor model has been used to develop a strategy for estimating rotor thrust/moments and inflow states from strain and pressure distributions measured in flight. The strategy is capable of accurately estimating the thrust/moments and inflow states produced by a trimmed rotor. However, control perturbations must be applied slowly if the rotor states are to be accurately estimated during a transient response.

3.   A strategy has been developed by which the dynamic gains and apparent mass matrices can be identified from estimated rotor thrust/moments and inflow states. This strategy has been used with some success when applied to rotor states estimated from simulated data.

4.   The state estimation software has been exercised on Puma flight test data with the resulting normal pressure distribution, angle of attack distribution and mean rotor thrust bearing good agreement with those of Tarttelin (1989). Difficulties were encountered in estimating the harmonic inflow states and this has been attributed to either unmodelled effects in the evaluation of the blade pitch or an inappropriate model structure defining the induced flow distribution..

5.   The rotor states estimated from Puma hover data have been used to identify the dynamic gains matrix with promising results.

A4.5.   References Used in Appendix 4

1.   Peters, D. A., HaQuang, N., "Dynamic Inflow for Practical Applications", Journal of the American Helicopter Society, Technical Note, 1988

2.   Riley, J, et al, "Estimation of Rotor Blade Incidence and Blade Deformations from the Measurements of Pressures and Strains in Flight", Proceedings of the 14th European Rotorcraft Forum, Milan, 1988

3.   Padfield, G., D., et al, "UK Research into System Identification for Helicopter Flight Mechanics", Vertica, Volume 11, Number 4, pp. 665-684, 1987

4.   Tarttelin, P. C., "Rotor Loadings in Hover - Correlation of Theory and Experiment", Proceedings of the 15th European Rotorcraft Forum, Amsterdam, 1989

Appendix 5

This appendix will summarise the work carried out in the development of a suite of software, written in MATLAB/SIMULINK, for use in state estimation and identification of 6 degree of freedom simulation models.

A5.1. <u>Six Degree of Freedom State Estimation</u>

A5.1.1. Summary of the State Estimation Package KINEMOD

A full description of KINEMOD is provided by Turner (1992) and hence only a brief summary is included here in order to illustrate the key features of the methodology employed.

Essentially, KINEMOD estimates the vehicle's 6 DOF states by checking the consistency of the measured data in two distinct phases:-

> 1. The attitude pass
> 2. The velocity pass.

The corrections required for the measurements p, q, r, θ, ϕ, ψ are evaluated during the attitude pass with the corrections to the measurements a_x, a_y, a_z, V, β, α being evaluated during the velocity pass.

The correction applied to each state is assumed to take the form of a bias and gain applied to the measured value i.e., for an arbitrary state, x:-

$$x^* = (1 + \lambda_x)x_m - b_x \tag{A5.1}$$

where the superscript, *, and subscript, m, denote corrected and measured values respectively with λ_x and b_x being the applied bias and gain.

During the attitude pass, the Euler angles are integrated according to the following standard set of first order differential equations:-

$$\left.\begin{array}{l} \dfrac{d\phi}{dt} = p^* + q^* \sin\phi \tan\theta + r^* \cos\phi \tan\theta \\[2mm] \dfrac{d\theta}{dt} = q^* \cos\phi - r^* \sin\phi \\[2mm] \dfrac{d\psi}{dt} = q^* \sin\phi \sec\theta + r^* \cos\phi \sec\theta \end{array}\right\} \tag{A5.2}$$

where the inputs p^*, q^*, r^* are evaluated according to equation (A5.1) with the corresponding output equations being given by:-

$$\left.\begin{aligned}
\phi^* &= \left(1+\lambda_\phi\right)\phi + b_\phi \\
\theta^* &= \left(1+\lambda_\theta\right)\theta + b_\theta \\
\psi^* &= \left(1+\lambda_\psi\right)\psi + b_\psi
\end{aligned}\right\} \tag{A5.3}$$

During the velocity pass the following translational equations of motion are integrated:-

$$\left.\begin{aligned}
\frac{du}{dt} &= -wq^* + vr^* + a_x^* - g\sin\theta \\
\frac{dv}{dt} &= -ur^* + wp^* + a_y^* - g\cos\theta\sin\phi \\
\frac{dw}{dt} &= -vp^* + uq^* + a_z^* - g\cos\theta\cos\phi
\end{aligned}\right\} \tag{A5.4}$$

Where the input angular velocities (p^*, q^*, r^*) are the converged values from the preceding attitude pass and the input accelerations $\left(a_x^*, a_y^*, a_z^*\right)$ are evaluated according to Equation (A5.1).

The output equations are now:-

$$\left.\begin{aligned}
V^* &= \left(1+\lambda_v\right)\sqrt{\left(u_b^2 + v_b^2 + w_b^2\right)} + b_v \\
\beta^* &= \left(1+\lambda_\beta\right)\tan^{-1}\left(\frac{v_b}{u_b}\right) + b_\beta \\
\alpha^* &= \left(1+\lambda_\alpha\right)\tan^{-1}\left(\frac{w_b}{u_b}\right) + b_\alpha
\end{aligned}\right\} \tag{A5.5}$$

where u_b, v_b and w_b are the velocity components at the sensor.

At each pass, a cost function is minimised in order to obtain the optimum set of correction parameters and initial conditions for the integrations. The cost function used is developed using statistical means and takes the form:-

$$J = \frac{1}{2}\sum_t \underset{\sim}{v}^T S^{-1} \underset{\sim}{v} + \frac{N}{2}\log|S| + \frac{1}{2}\sum_t \Delta\underset{\sim}{\zeta}^T S_\zeta^{-1} \Delta\underset{\sim}{\zeta} \tag{A5.6}$$

where:

$\underset{\sim}{v}$ is the residual vector giving the difference between measured and integrated output vectors

$\Delta \underset{\sim}{\zeta}$ gives the difference between the current estimates and the initial estimates for the correction parameters and initial conditions

N is the total number of time points in the measured data

S is the output error covariance matrix evaluated at the previous iteration

S_ζ is a diagonal weighting matrix input by the user.

The cost function given in Equation A5.6 is minimised using a Gauss-Newton iteration scheme in order to obtain the optimum blend of correction parameters.

A5.1.2. MATLAB/SIMULINK Implementation of KINEMOD

In this implementation, the attitude and velocity passes have been written as two independent pieces of SIMULINK code (EULSIM and VELSIM shown in Figures A5.1. and A5.2. respectively) and these will now be discussed in detail.

A5.1.2a. Attitude Pass

As stated in Section A5.1.1, the inputs to this pass are the measured rates and attitudes (*prate, qrate, rrate, phim, thetam, psim* respectively). The rates are input at the blocks *pinput, qinput* and *rinput* by means of a 'From Workspace' block which is selected from the standard SIMULINK library. In order to input data using this technique, the specified input matrix must comprise at least two columns - the first containing a vector of time points and the second containing the corresponding vector of measured data. If an output value is required between two measured time points then SIMULINK performs a linear interpolation to obtain the necessary value. The bias and gain are also applied to the measured signals at this stage and in Figure A5.1 the block *pinput* has been unmasked in order to show the technique employed. The bias and gain are input under the variable names *mp* and *bp* by means of the constant blocks *bias* and *gain* shown in the Figure. The three signals for measured roll rate, bias and gain are then multiplexed to form the input vector for the 'MATLAB Fcn' block which generates the input signal according to Equation A5.1.

Pinput, qinput and *rinput* are subsequently multiplexed to form the input vector for the block *eulsfn* which is an S-Function that provides SIMULINK with the information necessary to integrate Equations A5.2. In order to perform this task, the S-Function is written as a MATLAB M-file which returns salient information (such as the number of input states, the number of output states, initial conditions and state derivatives) to the

calling SIMULINK program. The output vector from *eulsfn* is demultiplexed producing the integrated attitudes before Equations A5.3 are executed in the blocks *phiout, thetaout* and *psiout* hence producing the reconstructed attitudes *theta, phi* and *psi*.

The measured states *phim, thetam* and *psim* are input to the SIMULINK model by means of the 'From Workspace' blocks. The disparities between reconstructed and measured states are then evaluated in the *error* block using 'MATLAB Fcn' blocks.

Finally, the error signals are passed to the MATLAB workspace.

A5.1.2b. Velocity Pass

From Figure A5.2, it can be seen that the measured accelerations are input to VELSIM and corrected using exactly the same methodology as was applied to the measured rates in the attitude pass. The converged states from the attitude pass are input by means of 'From Workspace' blocks before being multiplexed with the corrected accelerations to form the input vector for the S-Function *velsfn* . As was discussed in Section A5.1.2a *velsfn* is a MATLAB M-file which returns the information necessary for SIMULINK to integrate Equations A5.4. The output vector from *velsfn* contains the velocity components of the vehicle centre of gravity and this vector is demultiplexed before being passed to the blocks *Velout, Betaout* and *Alphaout*. These blocks contain 'MATLAB Fcns' which evaluate the output equations given by Equations A5.5 to provide the reconstructed vehicle speed, sideslip and angle of attack respectively.

The disparities between measured and reconstructed values are then evaluated in the same manner as was discussed for the attitude pass before the error vectors are written to MATLAB workspace.

A5.1.2c. MATLAB Command File

EULSIM and VELSIM can be run directly from their SIMULINK menu bars and this provides an extremely useful technique for performing 'one off' simulations. However, as previously stated, an iteration scheme is used to minimise the cost function given by Equation A5.6 and this will necessitate repeated evaluations of the attitude and velocity passes. In such cases, execution of SIMULINK models is best performed from the command line as the simulations can then be run from a MATLAB M-file allowing model parameters to be altered as the iteration proceeds. This technique has the additional benefit of allowing direct access to the range of MATLAB Toolboxes, hence, the minimisation process can be carried out using an 'off the shelf' MATLAB function. It was hoped to exploit this benefit by using a MATLAB Optimisation Toolbox routine to perform the minimisation of the cost function given by Equation A5.6. However, the presence of the

output error covariance matrix in Equation A5.6 generated difficulties which, after considerable effort, were found to render the generic optimisation routines of the Optimisation Toolbox unsuitable for this application. The problems encountered in using the Optimisation Toolbox to minimise Equation A5.6 are now summarised by the following discussion.

When minimising Equation A5.6, one makes an initial *a priori* estimate to the output error covariance matrix, S, then, at each iteration, this estimate is updated using the current error vectors:-

$$S_{est}^{k+1} = diag\left[\frac{1}{N}\sum_t\left(\underset{\sim}{z}_m - \underset{\sim}{z}_p^k\right)\left(\underset{\sim}{z}_m - \underset{\sim}{z}_p^k\right)^T\right] \qquad (A5.7)$$

where:-

$\underset{\sim}{z}_m$ is the vector of measured signals

$\underset{\sim}{z}_p^k$ is the vector of predicted outputs based on the parameter estimates of the kth

iteration.

This process is repeated until the cost function is minimised and the S matrix converges to a constant state.

Such a scheme could not be directly accommodated by the Optimisation Toolboxes and, as a result, these had to be altered in order to update the S matrix at each iteration. However, the Toolbox routines all incorporate sophisticated techniques for updating the Hessian matrix and selecting the direction in which to search for a minimum. Also, the user is not generally advised to make alterations to the M-files which form the MATLAB Toolboxes. Consequently, significant problems arose when attempting to update S within the Optimisation Toolboxes. In fact, this alteration lead to very slow convergence of the scheme and, in most cases, the iteration became unstable and diverged. After considerable time and effort had been expended it was therefore concluded to abandon the Optimisation Toolboxes in favour of a dedicated Gauss-Newton scheme.

The scheme adopted has been used with considerable success in KINEMOD and is quoted by Turner (1992). Essentially, the parameter vector is updated by means of the following expression:-

$$\underset{\sim}{\zeta}^{k+1} = \underset{\sim}{\zeta}^k - \left(M^k\right)^{-1}\underset{\sim}{g}^k$$

where the Hessian matrix M and gradient vector $\underset{\sim}{g}$ are approximated by the following

Taylor series:-

$$M = \sum_t \frac{\partial \underset{\sim}{v}^T}{\partial \underset{\sim}{\zeta}} S^{-1} \frac{\partial \underset{\sim}{v}}{\partial \underset{\sim}{\zeta}} + \sum_p S_\zeta^{-1}$$

$$\underset{\sim}{g} = \sum_t \underset{\sim}{v}^T S^{-1} \frac{\partial \underset{\sim}{v}}{\partial \underset{\sim}{\zeta}} + \sum_p \Delta \underset{\sim}{\zeta}^T S_\zeta^{-1}$$

The software implementation of this iteration scheme has been written as a MATLAB M-file called GITER.

When using the above iteration scheme, rapid minimisation of Equation A5.6 and concurrent convergence of the S matrix was achieved. In fact, it is suspected that this scheme provides faster convergence, in terms of CPU time, than would be possible with the Optimisation Toolboxes because there has been no recourse to sophisticated techniques for updating the Hessian matrix or obtaining search directions.

A MATLAB command file KINEMAT which calls the routines EULSIM, VELSIM and the iteration scheme GITER has been written to obtain the optimal set of biases and gains necessary to ensure kinematic consistency of data measured in flight.

A5.1.2d. Validation of KINEMAT

In order to validate KINEMAT the software was exercised using flight test data. Events 6, 7, 8 and 9 of Flight 258 were used in this task and no anomalies were uncovered for either the attitude or velocity pass in any case. The attitude pass of Event 8 is of particular interest because KINEMOD data were available for direct comparison. The results of this comparison are summarised in Table A5.1:-

Parameter	KINEMAT	KINEMOD
phi(0) (rad)	-0.009	-0.009
theta(0) (rad)	0.009	0.011
psi(0) (rad)	1.639	1.649
bp (rad)	-0.027	-0.027
bq (rad)	0.074	0.076
br (rad)	-0.000	-0.002
mp	-0.034	-0.031
mq	0.068	0.087
mr	0.020	0.014
bphi (rad)	-0.000	0.000
btheta (rad)	0.004	0.000
bpsi (rad)	0.019	0.009
mphi	0.010	0.015
mtheta	0.011	0.040
mpsi	-0.036	-0.014

Table A5.1 Comparison Between Results Produced By KINEMAT and
KINEMOD for Attitude Pass (F258 Event 8)

As can be seen comparison between KINEMAT and KINEMOD is very good with disparities generally only being present in the 3rd decimal place.

Figure A5.3 shows a comparison between measured and integrated vehicle attitudes and measured and corrected rates for Event 8 when no bias or gain is applied to the measured signals. (In each plot the measured state is depicted by the solid line and the integrated attitude or corrected rate by the chained line). As can be seen the comparison between integrated an measured attitudes shows significant disparities between the two signals. The integrated history for θ passes through 90 degrees at approximately 19 seconds and this is responsible for the singularity in ϕ and ψ. As no correction has been applied to the measured signal the traces for measured and corrected rates are coincident.

Figure A5.4 shows a similar comparison once the correction parameters identified by KINEMAT have been applied. From the time histories depicting the vehicle attitudes it is evident that excellent correlation exists between measured and integrated signals with the only visible disparity being manifest in a small error in the vehicle track angle ψ. The time histories of vehicle rates show the effects of the correction parameters on these states with the largest witnessed correction being the bias applied to the vehicle pitch rate, q.

Figure A5.5 shows a comparison between measured and integrated vehicle speed, sideslip angle and angle of attack and also measured and corrected accelerations when no bias or gain is applied to the measured signals. Poor agreement is evident between integrated and measured time histories with the integrated vehicle speed and angle of attack

both diverging significantly from their measured counterparts. The measured and corrected accelerations are coincident because no bias or gain has been applied to the measured signals.

Figure A5.6 shows a similar comparison once the correction parameters identified by KINEMAT have been applied. With reference to this figure it is evident that excellent correlation has been obtained between the time histories for measured and integrated speed. However, correlation for the integrated and measured angles is fairly poor with a phase shift being evident in both cases. It is felt that this error could be attributable to a lag in the sensors measuring the vehicle lateral and normal velocity components. This lag cannot be corrected by the application of a bias and gain hence the phase shift is still present after the correction parameters have been applied. It should be noted that the measured and integrated signals now have approximately the same mean value, therefore it is felt that, KINEMAT has identified the best possible set of biases and gains.

A5.2. Six Degree of Freedom Parameter Identification

In order to complete the MATLAB System Identification Suite, 6 degree of freedom parameter identification software was required within the MATLAB environment. Optimal Subset Regression (OSR) is a parameter identification technique which has been used with considerable success at both the University of Glasgow and DRA Bedford, Black et al (1986), Padfield et al (1987), hence, it was decided that OSR represented the most suitable methodology for use in the completion of the MATLAB System Identification Suite. A frequency domain parameter identification package (FOSR), based on an OSR approach, has been written within the MATLAB environment and this will now be discussed.

A5.2.1. The OSR Technique

A full description of the OSR technique is given by Padfield et al (1987) hence only a brief description is felt appropriate here. Essentially, the technique is based on a least squares minimisation of the equation error:-

$$y(t) = \theta_0 + \theta_1 x_1(t) + \theta_2 x_2(t) + \ldots\ldots\ldots + \varepsilon(t)$$

or

$$\underset{\sim}{y} = X \underset{\sim}{\theta} + \underset{\sim}{\varepsilon} . \tag{A5.8}$$

Where :

the vector $\underset{\sim}{y}$ is the time history of the dependent variable

the columns of the matrix X are the time histories of the of the independent variables x_1, x_2 etc.
the vector $\underset{\sim}{\theta}$ contains the parameters being identified

the vector $\underset{\sim}{\varepsilon}$ is the residual vector comprising both measurement and process

noise.

In this case, the dependent variable $\underset{\sim}{y}$ will generally be a vehicle translational or angular

acceleration; the matrix X will be formed using time histories of the vehicle states (estimated by KINEMAT) and the vector $\underset{\sim}{\theta}$ will contain the vehicle state and control

derivatives.

The least squares solution to the vector $\underset{\sim}{\theta}$ can be expressed analytically by the

expression:–

$$\underset{\sim}{\theta} = \left(X^T X\right)^{-1} X^T \underset{\sim}{y}. \tag{A5.9}$$

The OSR technique proceeds by sequentially applying Equation A5.9 and at each stage, the independent variable which has the highest partial correlation with the residual (or partial F-ratio) is added to the model structure. This process is repeated until the F-ratio falls below a minimum threshold (specified by the user) and hence, the optimal model structure is obtained. At each stage the partial F-ratio for an arbitrary parameter, θ_i, is given by:-

$$F_i = \frac{\theta_i^2}{s_i^2}$$

where s_i^2 the standard error of the parameter θ_i, is given by:-

$$s_i^2 = \sigma^2 diag\left(X^T X\right)^{-1}$$

and σ^2 is the variance of the equation error.

The multiple correlation co-efficient, R^2, is also of interest as it provides a direct measure of the quality of the fit as each parameter is added to the identified model structure:-

$$R^2 = \frac{\left(X\underset{\sim}{\theta}\right)^T \left(X\underset{\sim}{\theta}\right)}{\underset{\sim}{y}^T \underset{\sim}{y}}$$

A software implementation, TOSR, of the above technique has been written in the MATLAB environment and the results obtained will now be discussed.

A5.2.2. Results Produced by TOSR

In order to gain experience with the OSR technique and also to promote confidence that the new software was functioning correctly TOSR was primarily exercised using simulated data. These data were generated using a linear 3 state model with one control input available for excitation. In this case, the state derivatives were chosen to be representative of those encountered in the rolling, pitching and yawing moment equations and the control derivatives were chosen to be representative of those associated with an input of lateral cyclic:-

$$
\begin{bmatrix} \dot{p} \\ \dot{q} \\ \dot{r} \end{bmatrix} = \begin{bmatrix} L_p & L_q & L_r \\ M_p & M_q & M_r \\ N_p & N_q & N_q \end{bmatrix} \begin{bmatrix} p \\ q \\ r \end{bmatrix} + \begin{bmatrix} L_{\theta 1C} \\ M_{\theta 1C} \\ N_{\theta 1C} \end{bmatrix}
\tag{A5.10}
$$

where the following derivatives were input to the model:-

$L_p = -8.0$ (1/s) $\quad L_q = 1.5$ (1/s) $\quad L_r = -0.1$ (1/s) $\quad L_{\theta 1c} = 100$ (1/s^2)

$M_p = 0.0$ (1/s) $\quad M_q = -1.0$ (1/s) $\quad M_r = 0.1$ (1/s) $\quad M_{\theta 1c} = 0.0$ (1/s^2)

$N_p = 0.0$ (1/s) $\quad N_q = 1.0$ (1/s) $\quad N_r = 10.0$ (1/s) $\quad N_{\theta 1c} = 10.0$ (1/s^2)

In order to drive the model, a 3211 input of amplitude +/- 0.5 degrees was applied to the lateral cyclic control and the response obtained is shown in Figure A5.7.

A5.2.2a. The Use of TOSR on Simulated Data in the Absence of Noise

TOSR was used to identify the rolling moment derivatives for the time segment from $t = 5s$ to $t = 25s$ and the following results were obtained:-

Step Number	1	2	3	4
$L_{\theta 1c}$	12.465	100.09	100.31	100.00
L_p	-	-8.041	-8.060	-8.000
L_q	-	-	0.560	1.500
L_r	-	-	-	-0.1
R^2	0.12509	0.99983	0.99996	1.00000

Table A5.2 Parameters Identified by TOSR using Simulated Data with no Noise Present

As can be seen, TOSR identifies the control derivative and primary damping as being the most significant parameters in producing the fit with the final model structure (step 4) consisting of derivatives which exactly match those input into Equation A5.10. Also, the multiple correlation co-efficient, R^2, increases as each parameter is added to the identified model until a value of 1 is attained at the 4th step. A comparison between the

time history of $\dot{p}(t)$ produced by Equation A5.10 and that produced by the identified model is given in Figure A5.8 and from this figure it is evident that the time histories are coincident.

Hence, it can be concluded that TOSR has functioned correctly and identified the set of derivatives input into Equation A5.10.

A5.2.2b. The Use of TOSR on Simulated Data in the Presence of Noise

Measurement noise was now simulated by injecting noise with zero mean and a variance of 10% RMS onto the time histories produced by Equation A5.10. The resulting time histories for the 3 model states and control input are shown in Figure A5.9. The identification process was now repeated and the results obtained are tabulated below:-

Step Number	1	2	3	4
$L_{\theta 1c}$	12.445	87.0258	86.3909	84.1540
L_p	-	-6.9427	-6.8553	-6.3373
L_r	-	-	-0.1000	-1.1181
L_q	-	-	-	10.906
R^2	0.12627	0.8755	0.8760	0.8824

Table A5.3 Parameters Identified by TOSR using Simulated Data in the Presence of Noise

With reference to Table A5.3 it can be seen that TOSR now underestimates the control derivative and the primary damping by approximately 16% and 20% respectively. Large errors are also present on the cross coupled derivatives with L_r and L_q being overestimated by factors of 10 and and 8 respectively. However, the multiple correlation co-efficient does increase to a value of 0.88 which suggests that the quality of fit to the 'measured' $\dot{p}(t)$ is of reasonable quality. With reference to Figure A5.10 which shows a comparison between the time histories for 'measured' and identified $\dot{p}(t)$ it can be seen that agreement is indeed fairly good.

In the above examples, $\dot{p}(t)$ was evaluated analytically using Equation A5.10 and therefore negligible processing noise was introduced at this stage. In practice, when flight test data are used, numerical techniques will be required to obtain vehicle translational and angular accelerations from the estimated states (u, v, w, p, q, r). In the time domain, this differentiation would typically be carried out by numeric differencing which is susceptible to the generation of considerable errors. Hence, in practice, the model parameters identified by TOSR would also be prone to large processing errors. The influence of such processing and measurement noise can be reduced to an acceptable level by the use of low pass filtering, eg Kalman Filtering, before the identification process is carried out, Padfield et al

(1987). However, such pre-processing of the estimated states is inconvenient and the selection of a suitable cut-off frequency for the filter can be awkward.

Black et al (1986), highlight that frequency domain techniques represent a more convenient methodology for performing parameter identification. In this approach, the measured time histories are transformed into the frequency domain using the Fast Fourier Transformation (FFT) and thus all the data which lies outwith the frequency range of interest can be disregarded. Thus, it is now possible to remove higher frequency measurement and process noise by inspection and, additionally, models can be developed which are applicable over a selected frequency range. Furthermore, the estimated states can be differentiated without the need for numeric differencing and hence this process is less error prone in the frequency domain than in the time domain. In light of these advantages it was decided to reformulate the identification software using frequency domain techniques and this will now be discussed.

A5.2.3. OSR in the Frequency Domain

In the frequency domain Equation A5.9 becomes:-

$$y(\omega) \;=\; X(\omega)\,\theta \;+\; \varepsilon(\omega)$$

where the least squares solution is now obtained by minimising the following cost function, quoted by Black et al (1986):-

$$J=\sum_{\omega_1}^{\omega_2}\left[\left\{\mathrm{Re}[\varepsilon(\omega)]\right\}^{T}\left\{\mathrm{Re}[\varepsilon(\omega)]\right\}+\left\{\mathrm{Im}[\varepsilon(\omega)]\right\}^{T}\left\{\mathrm{Im}[\varepsilon(\omega)]\right\}\right].$$

The partial F-ratios, standard errors, s_i, and multiple correlation co-efficients, R^2, are evaluated using the same expressions as were quoted previously in Section A5.2.1.

As stated in the preceding section, the translational and angular accelerations occurring in flight will be evaluated numerically from the time histories of the estimated states. In the frequency domain, the acceleration of an arbitrary state $x(\omega)$ is given by Black et al (1987) as:-

$$\dot{x}(\omega)=j\omega x(\omega)+G(\omega)$$

where the term $G(\omega)$ is included to correct for the effects of non-periodic windowing and is given by:-

$$G(\omega)=\frac{\sqrt{N}}{T}\left[y\!\left(T-\frac{\Delta t}{2}\right)-y\!\left(-\frac{\Delta t}{2}\right)\right]\exp(j\omega\frac{\Delta t}{2})$$

and where N is the number of samples in the time domain record, Δt is the sampling interval and T is the record length in seconds.

A MATLAB M-file, FOSR, which includes the definitions given in this section has been written in order to perform OSR parameter identification in the frequency domain. Results produced by FOSR will now be discussed.

A5.2.4. Results Produced by FOSR

A5.2.4a. Use of FOSR on Simulated Data in the Absence of Noise

FOSR was initially tested using simulated data generated by the linear model given in Equation A5.10. As described in Section 2.1, an attempt was first made to identify the rolling moment and control derivatives with zero 'measurement' noise injected on the time histories of the 'measured' states. The segment from 5 to 25 seconds was again used in the identification with a 1024 point FFT being used to transform the data into the frequency domain. Before the identification process is carried out, FOSR displays the relevant real, imaginary and power spectra onto the screen so that the user can select an appropriate frequency range for consideration in the identification. In this case, most of the signal content was contained between 0 and 1Hz and hence this was selected as the frequency range over which the identification was carried out. The results produced by FOSR are tabulated below:-

Step Number	1	2	3	4
L_r	-10.370	-1.5328	0.0529	-0.1000
$L_{\theta 1c}$	-	11.5547	100.9942	100.0000
L_p	-	-	-8.1338	-8.0000
L_q	-	-	-	1.5000
R^2	0.1568	0.3477	0.9998	1.0000

Table A5.4. Parameters Identified by FOSR using Simulated Data with no Noise Present

With reference to Table A5.4 it is evident that FOSR has functioned successfully with all parameters identified in the 4 state model having zero error to the 4th decimal place. Also, R^2 attains a value of 1.0000 indicating that excellent correlation has been achieved between the spectra of the 'measured' and identified $\dot{p}(\omega)$, in fact, from Figure A5.11, it is evident that these spectra are coincident across the frequency range considered. Figure A5.11 also shows a comparison between identified and 'measured' $\dot{p}(t)$ and again the signals are coincident. Hence, it can be concluded that FOSR has accurately identified the stability and control derivatives originally input to Equation A5.10.

From Table A5.4 it should be noted that FOSR has identified L_r as being the most significant derivative when the single state model is identified at step 1. This is inconsistent with the results produced in the time domain by TOSR where, perhaps more appropriately, the control derivative was selected at step1. Such an inconsistency is suggestive of some anomaly in the evaluation of the partial F-ratios in FOSR and it is recognised that this warrants further attention.

A5.2.4b. The Use of FOSR on Simulated Data in the Presence of Noise

FOSR's ability to identify derivatives in the presence of noise was investigated by performing an identification using the time histories shown in Figure A5.9. (As described in Section A5.2.2b these signals were produced by corrupting the output from Equation A5.10 with noise of zero mean and variance of 10% RMS). As in the previous example, a 1024 FFT was used to transform the data into the frequency domain and a frequency range of 0 to 1Hz was used in the identification. The parameters now identified by FOSR are tabulated below:-

Step Number	1	2	3	4
L_r	-1.0389	-1.5262	0.1040	-0.0430
$L_{\theta 1c}$	-	11.6053	103.0294	102.0269
L_p	-	-	-8.2847	-8.1527
L_q	-	-	-	1.4316
R^2	0.1560	0.3461	0.9774	0.9776

Table A5.5. Parameters Identified by FOSR using Simulated Data in the Presence of Noise

With reference to the above table it can be seen that, despite the presence of noise, FOSR has accurately identified the derivatives $L_{\theta 1c}$, L_p and L_q with errors of less than 5% being present in all 3 parameters. An error of approximately 50% does occur in L_r but it should be noted that R^2 increases to 0.9776 at step 4 indicating that excellent correlation exists between the spectra of 'measured' and identified signals. Figure A5.12 shows graphically the level of correlation in the frequency and time domains and, from this figure, it is evident that FOSR has accurately regenerated $\dot{p}(t)$.

Having successfully tested FOSR on simulated data it was now decided to use this software to identify Westland Lynx stability and control derivatives from flight test data.

A5.3. Summary of Experiences Gained using FOSR on Flight Test Data

Numerous identifications have been performed using data from Events 6, 8 and 9 of Flight 258 with the vehicle states being estimated using the kinematic consistency program KINEMAT described in Section A5.1 of this appendix. Results produced by this work are

exemplified by the FOSR output file provided in Appendix A. In this case, the derivatives L_v, L_p, L_r, $L_{\theta 1c}$ were identified from the forced response to a 3211 input of lateral cyclic. Data with a frequency content in the range 0.03125 Hz to 1 Hz was selected for use in the identification and the F-ratio threshold was set at 1.

With reference to Appendix 5a it can be seen that FOSR has selected a 2 state model, comprising $L_{\theta 1c}$ L_v, as the favoured candidate structure with values of

$$L_{\theta 1c} = 3.9855(\text{rad/s}^2) = -34 \ (1/\text{s}^2)$$
$$L_v = 0.1471 \ (1/\text{s})$$

which do not compare favourably with the HELISTAB values of -152 $(1/\text{s}^2)$ and -0.27 $(1/\text{s})$ respectively. However, the R^2 value of 0.75 reflects that relatively good correlation exists between the identified and measured spectra of $\dot{p}(\omega)$ and this is supported graphically by Figure A5.13. This figure also shows a comparison between the time histories of identified and measured $\dot{p}(t)$ (the trace for measured $\dot{p}(t)$ is noisy because this was evaluated by numeric differencing of the measured $p(t)$) and it can be seen that the identified model achieves good correlation with the measured signal.

With reference to Appendix 5a it is evident that the regression is allowed to continue after the F-ratio threshold has been reached so all four parameters may be included in the model structure. As can be seen the parameters now have the following values:-

$$L_{\theta 1c} = 7.2841(\text{rad/s}^2) = -62 \ (1/\text{s}^2)$$
$$L_v = -0.0559 \ (1/\text{s})$$
$$L_r = 3.9563 \ (1/\text{s})$$
$$L_p = -3.1416 \ (1/\text{s})$$

which differ considerably from the HELISTAB values of:-

$$L_{\theta 1c} = -152 \ (1/\text{s}^2)$$
$$L_v = -0.2705 \ (1/\text{s})$$
$$L_r = -0.0278 \ (1/\text{s})$$
$$L_p = -10.975 \ (1/\text{s})$$

However, it is worth noting that the R^2 value has increased to 0.9392 indicating excellent correlation between measured and identified spectra for $\dot{p}(\omega)$ and this is supported by the plots of these spectra shown in Figure A5.14.

From Appendix 5a it can be seen that the identified parameters vary considerably as each new parameter is added to the model structure. Also, the F-ratios can be seen to vary in a similar manner, eg, L_v is chosen as the most significant parameter for inclusion in

the 2-state model yet its F-ratio has fallen below the threshold at step 4. This feature is typical of the results produced by FOSR and could merit further investigation.

Other experiences with FOSR have shown that the identified parameter values can be very sensitive to the length of (time domain) record used in the identification. For example, the identification given in Appendix 5a was carried out using data from t=5 to t=8.5s; if this segment is extended to t=4 to t=9.5 s the following parameters are identified:-

$$L_{\theta 1c} = 5.6881(\text{rad/s}^2) = -48.5 \ (1/\text{s}^2)$$
$$L_p = -1.8370 \ (1/\text{s})$$
$$L_r = 2.5163 \ (1/\text{s})$$
$$L_v = -0.0197 \ (1/\text{s})$$

All these parameters had an F-ratio above 1 so this was now the favoured model structure which obviously differs considerably from the 2 state model previously identified. Also, the ordering of the parameters is different with the selection of L_v and L_p being transposed. Furthermore, the correlation co-efficient has fallen to 0.68 indicating that FOSR is having difficulty identifying a four state model capable of recreating the measured $\dot{p}(\omega)$, thus, more parameters are required for selection in the model structure.

One final observation; FOSR is liable to select parameters in a physically inappropriate order when forming model structures. For example, when using 7 parameters $(L_u, L_v, L_w, L_p, L_q, L_r, L_{\theta 1c})$ to model the roll response to an input of lateral cyclic then the parameters are selected in the following order:-

$$L_{\theta 1c} \quad L_q \quad L_v \quad L_w \quad L_u \quad L_r \quad L_p$$

with a 2 state model consisting of $L_{\theta 1c}$ and L_q being the favoured structure. This selection appears to be idiosyncratic and perhaps merits further investigation.

Hence it can be seen that FOSR is capable of identifying model structures which produce good correlation with measured spectra and time histories. However, some anomalies exist in the values identified for the model parameters and the order in which they are selected for inclusion in the model structure. Also, the identified values appear to be very sensitive to the length of record and frequency range selected for the identification. These perhaps merit further investigation.

A5.4. <u>Conclusions Drawn from Appendix 5</u>

A suite of 6 DOF state estimation and model identification software has been written within the MATLAB environment, this software has been extensively tested on both simulated and

real flight test data. The conclusions drawn form this exercise can be summarised as follows:-

    1.   A new state estimation software package, KINEMAT, has been written for use in the MATLAB/SIMULINK environment. KINEMAT, exploits the attributes of the this environment to provide benefits in terms of an improved user interface and greater visibility of the programming structure than was experienced with KINEMOD. Considerable effort was expended in an attempt to use the MATLAB Optimisation Toolbox to minimise the cost function given by Equation A5.6. However, this work was unsuccessful because the S matrix could not be updated correctly within the iteration loop. Therefore, it was decided to use a Gauss-Newton scheme similar to that utilised in KINEMOD to perform the minimisation. A MATLAB implementation of this scheme has been written in the form of the M-file, GITER, which now forms part of the KINEMAT package. This software has been used to successfully identify an optimal set of correction parameters necessary to correct flight test data and produce kinematic consistency in the measured signals.

    2.   Parameter identification software, FOSR, which utilises frequency domain OSR techniques has been written in the MATLAB environment. In order to gain experience using OSR and also to verify the new software, FOSR was first employed to identify parameters from simulated data and this task was successfully completed. FOSR, is currently being used to identify Westland Lynx stability and control derivatives using states estimated from flight test data by KINEMAT. When performing this identification, FOSR is capable of producing model structures which yield good correlation with the measured vehicle response. However, the identified parameter values differ significantly from those calculated by HELISTAB, also, some anomalies exist in the sequence by which FOSR selects parameters for inclusion in the identified model structures.

A5.5. <u>References Used in Appendix 5</u>

1.   Turner, G. P., "Consistency Analysis of Helicopter Flight Test Data", DRA Technical Memorandum FS 1031, 1992

2.   Black, C. G., et al "Experience with Frequency Domain Methods in Helicopter System Identification", Proceedings of the Twelfth European Rotorcraft Forum, Paper No 76, Garmisch, Germany, 1986

3.   Padfield, G. D., et al "UK Research into System Identification for Helicopter Flight Mechanics", Vertica, Volume 11, Number 4, pp. 665-684, 1987

Appendix 5a

Input .mat file was > ft8

Paramters chosen for model were:-

```
                              v
                              p
                              r
                              lat cyc
```

Parameter chosen for xdot was > p

Start record of time record was > 4.96875
End of time record was > 8.53125

The control time history was not lagged

A 1024 point Fourier transform converted data to frequency domain
Lower limit of frequency range was > 0.03125
Upper limit of frequency range was >   1
Frequency sampling interval was > 0.03125

F-ratio threshold was set at > 1

fratio1:-

   9.0563   0.0000   4.2429   18.1630

Correlation Co-efficient > 0.3647

Current parameters included are >

   3.2081 lat cyc

fratio2:-

  58.1212   39.5424   16.9506
  41.6758   17.9425   3.2894

Correlation Co-efficient > 0.7469

Current parameters included are >

   3.2081   3.9855 lat cyc
   0.0000   0.1471 v

fratio3:-

   2.0392   19.9841
   0.8023   2.8082
   0.0017   0.7028

Correlation Co-efficient > 0.8294
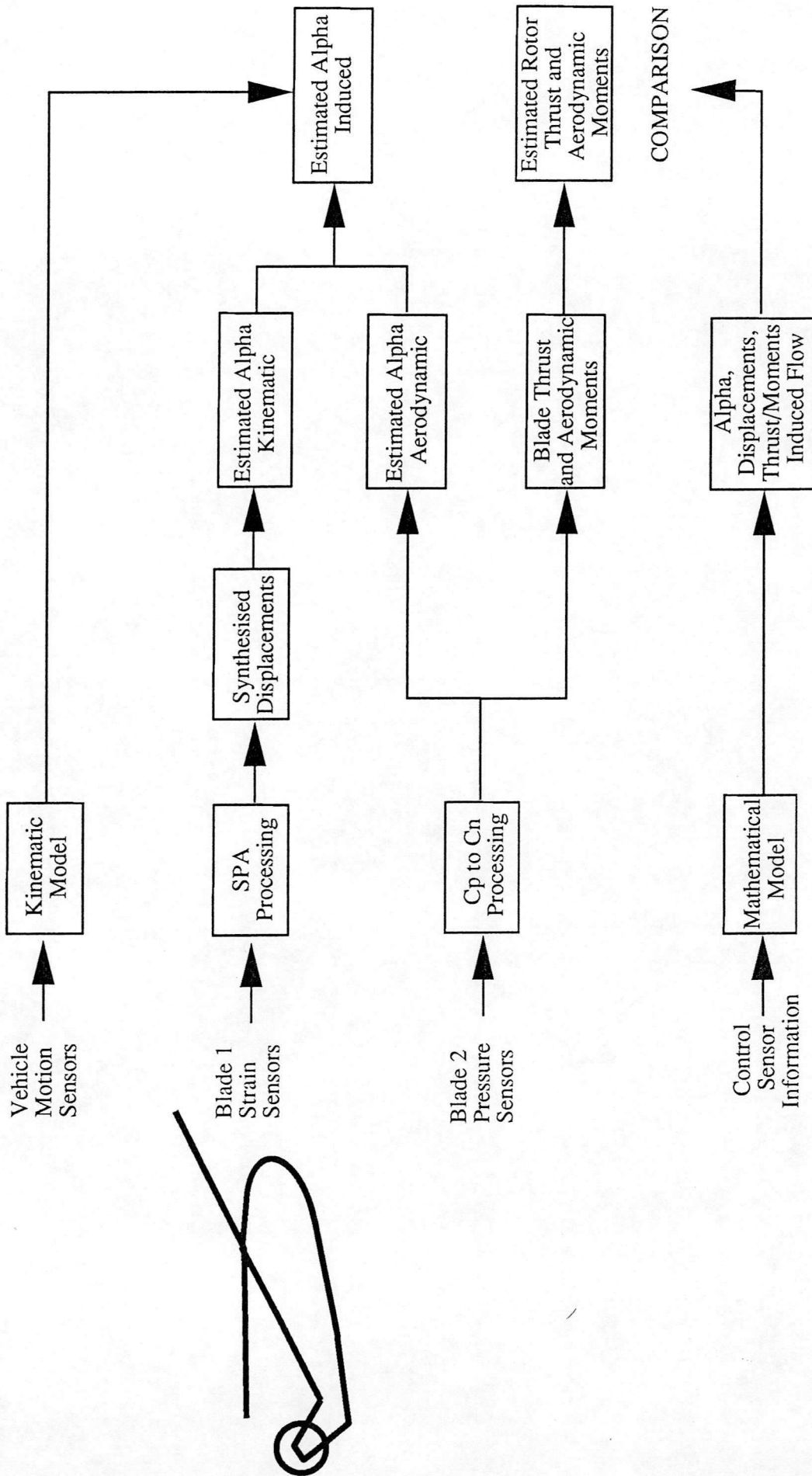
Figures

Figure 1 – The Validation Methodology
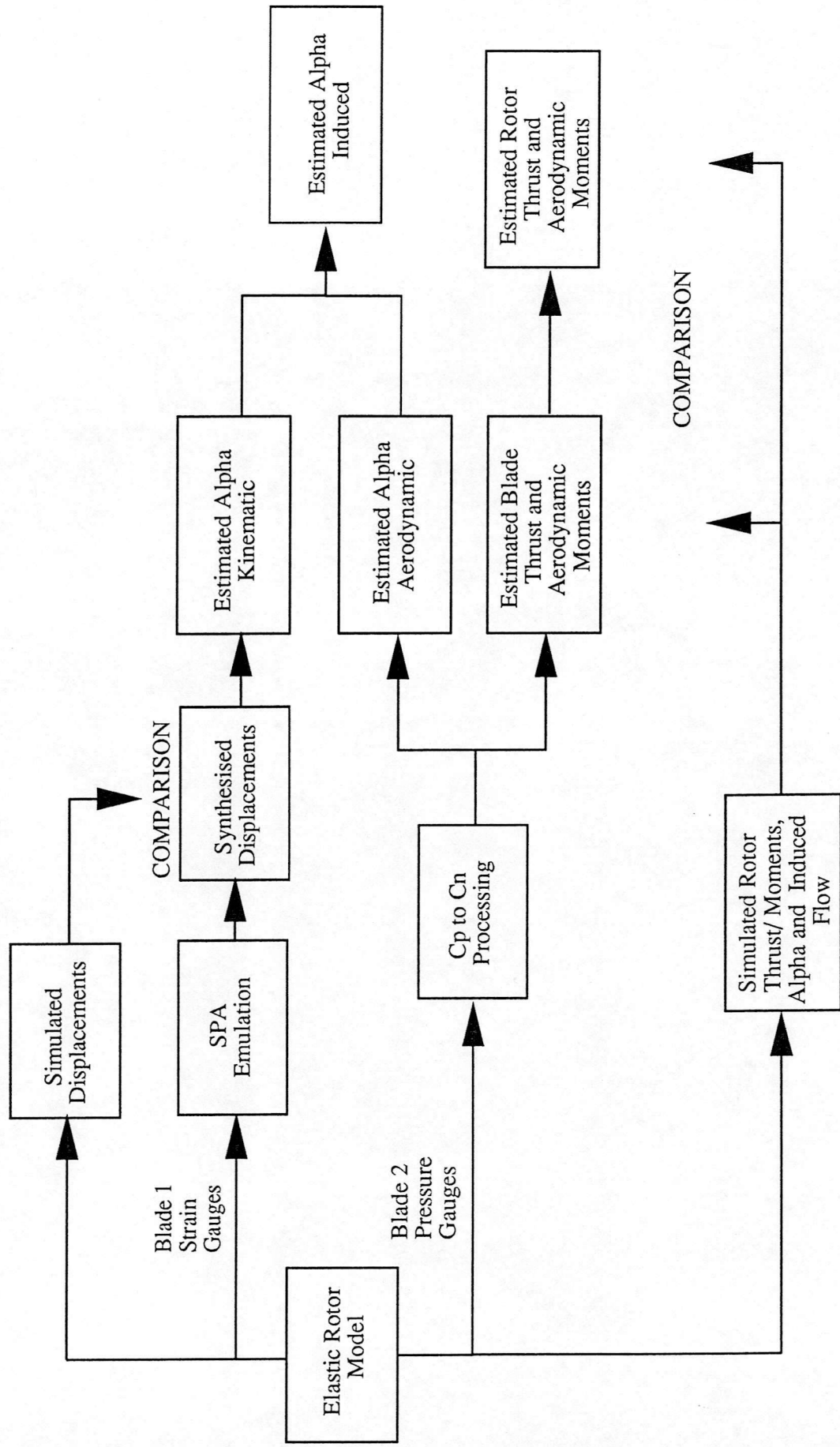
Figure 2 – Emulation of The Validation Methodology

Comparison of First 6 Rotating Modes Obtained when Using Duncan

Functions and Non-Rotating Mode Shapes as Trial Functions
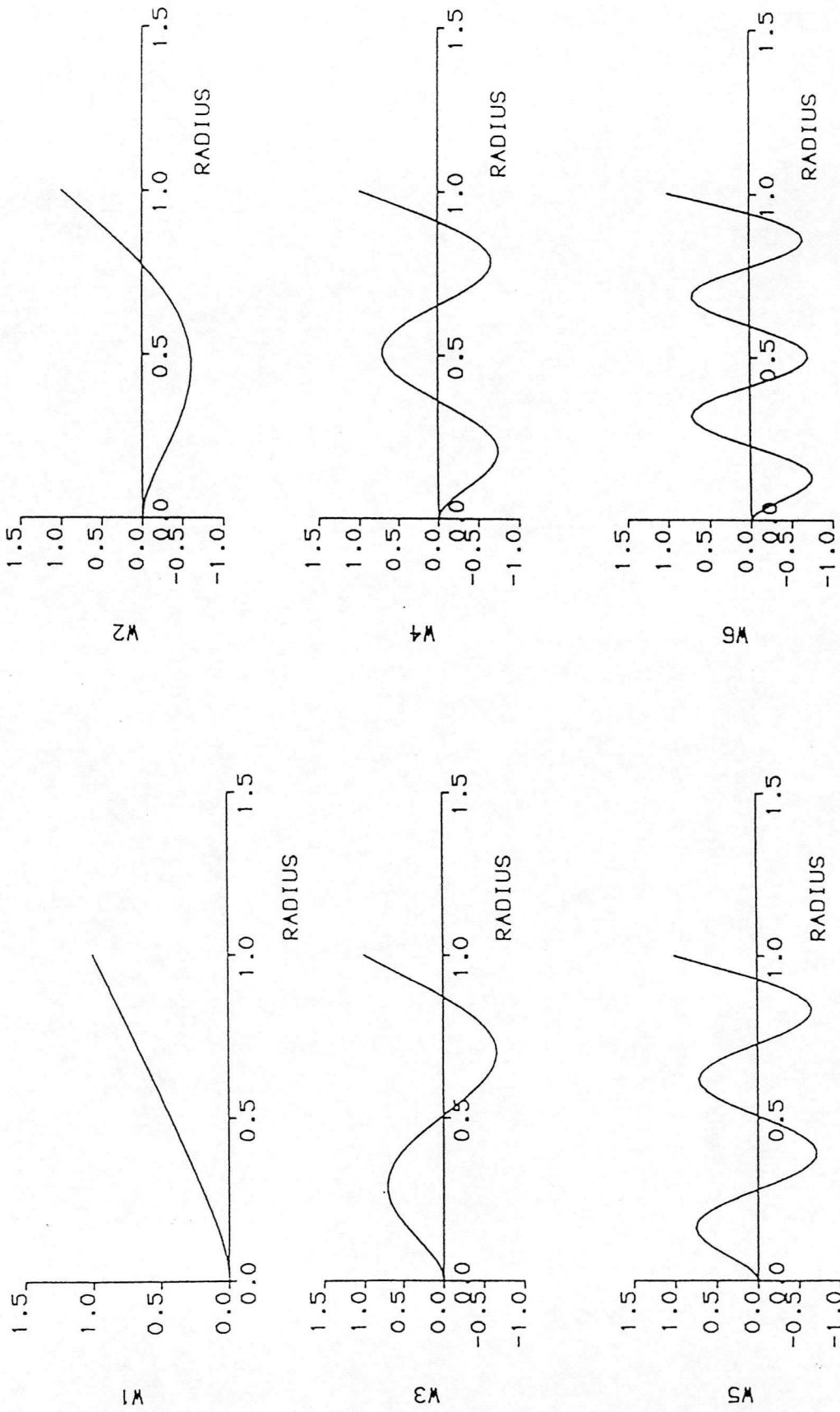
Figure A1.1

NON-ROTATING

DUNCAN

Displacements of Rotating Cantilever Forced at 35.63 Radians Per Second
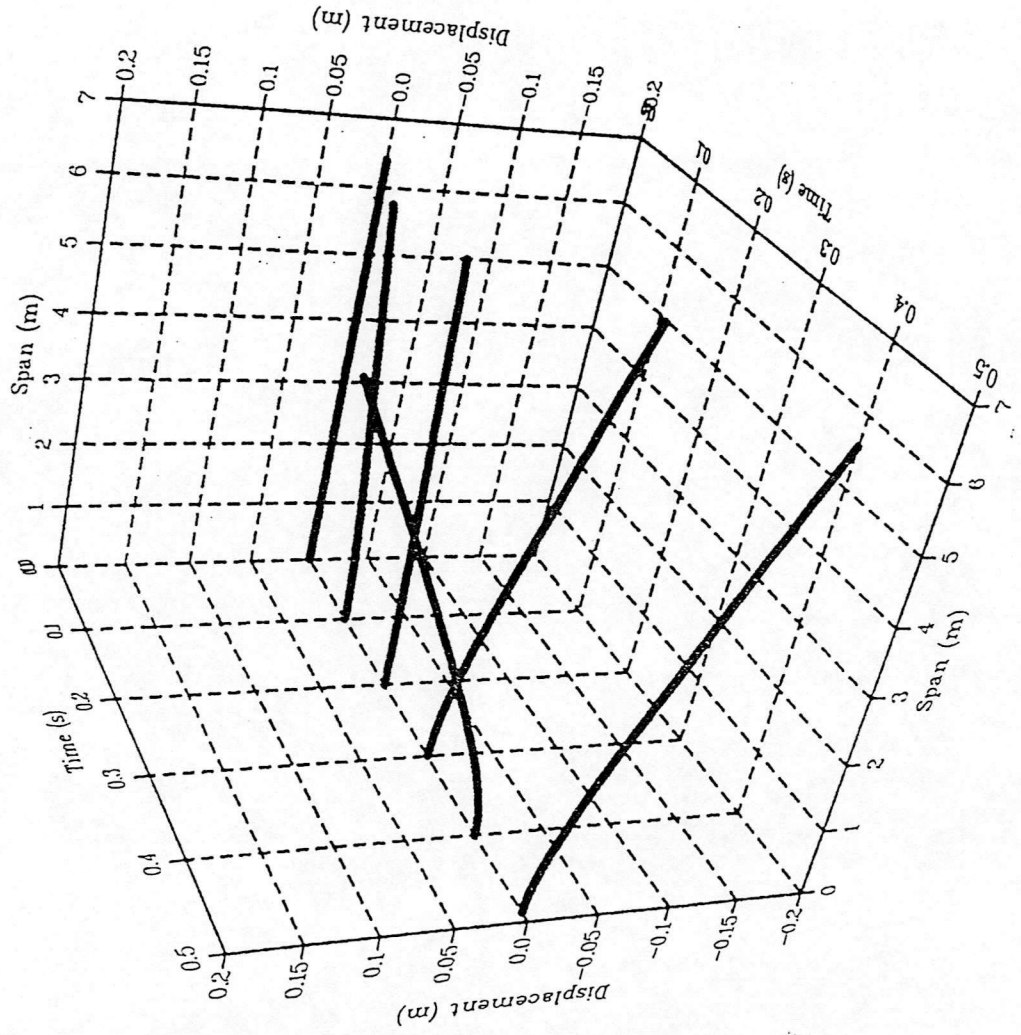
Figure A1.2

Displacements of Rotating Cantilever Forced at 345 Radians Per Second
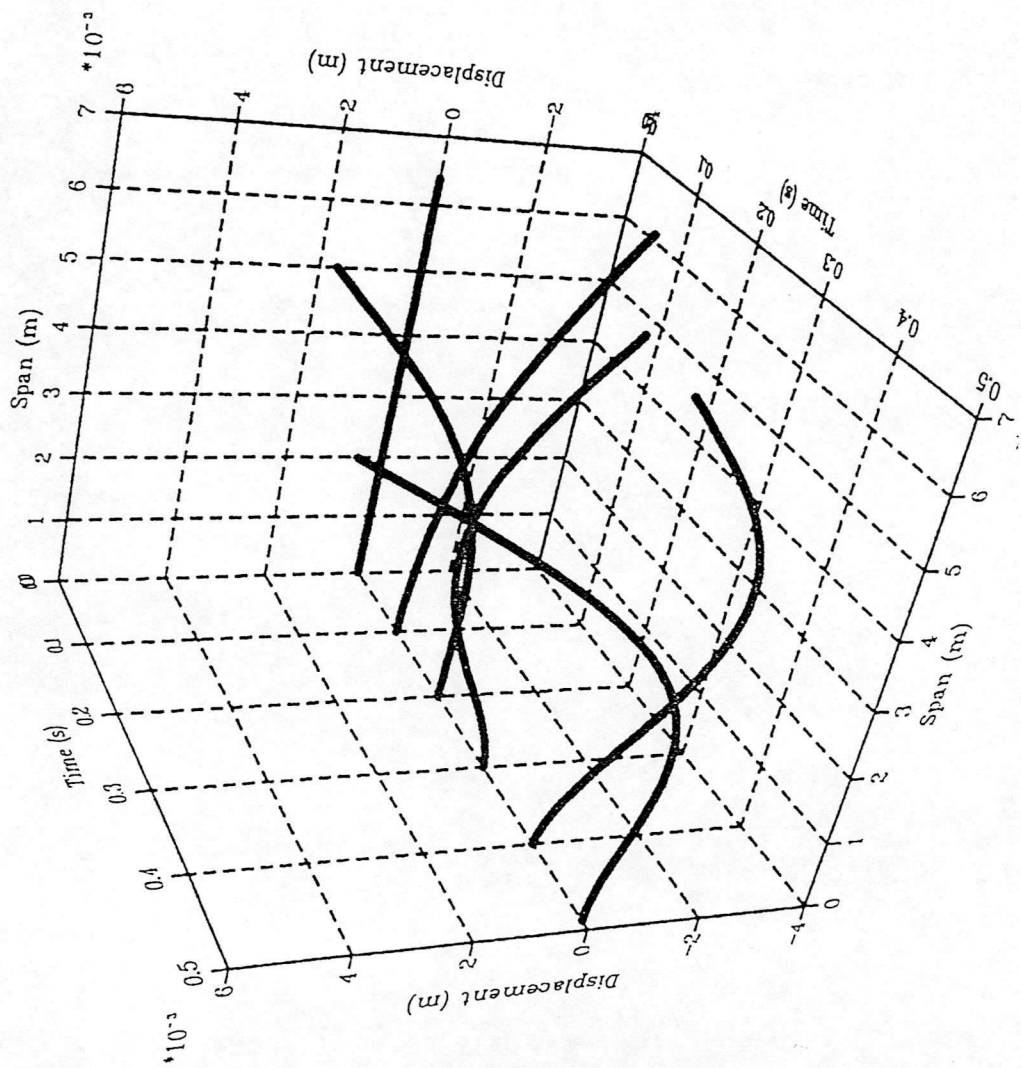
Figure A1.3

Displacements of Rotating Cantilever Forced at 1533 Radians Per Second
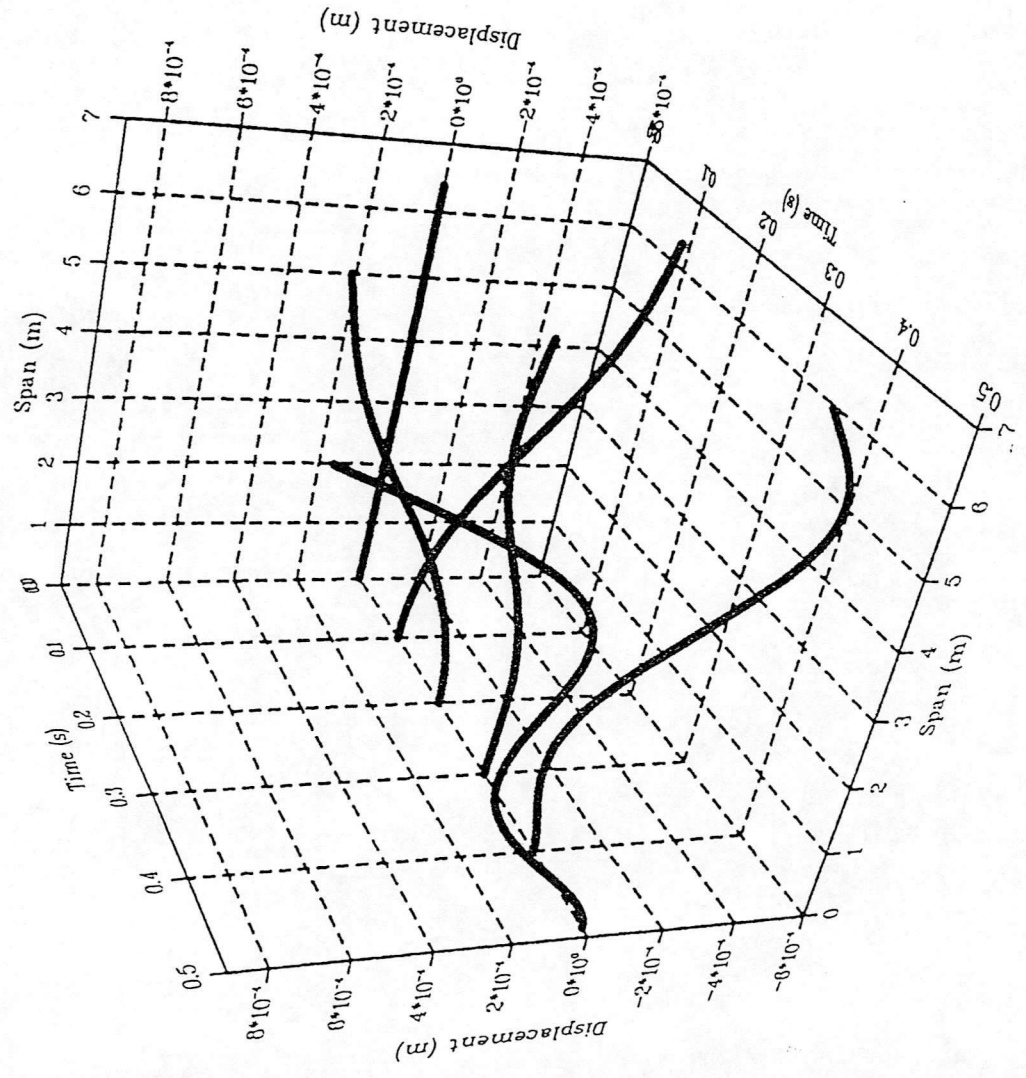
Figure A1.4

Contribution of Mode 1 When forced at 35.63 Radians per Second
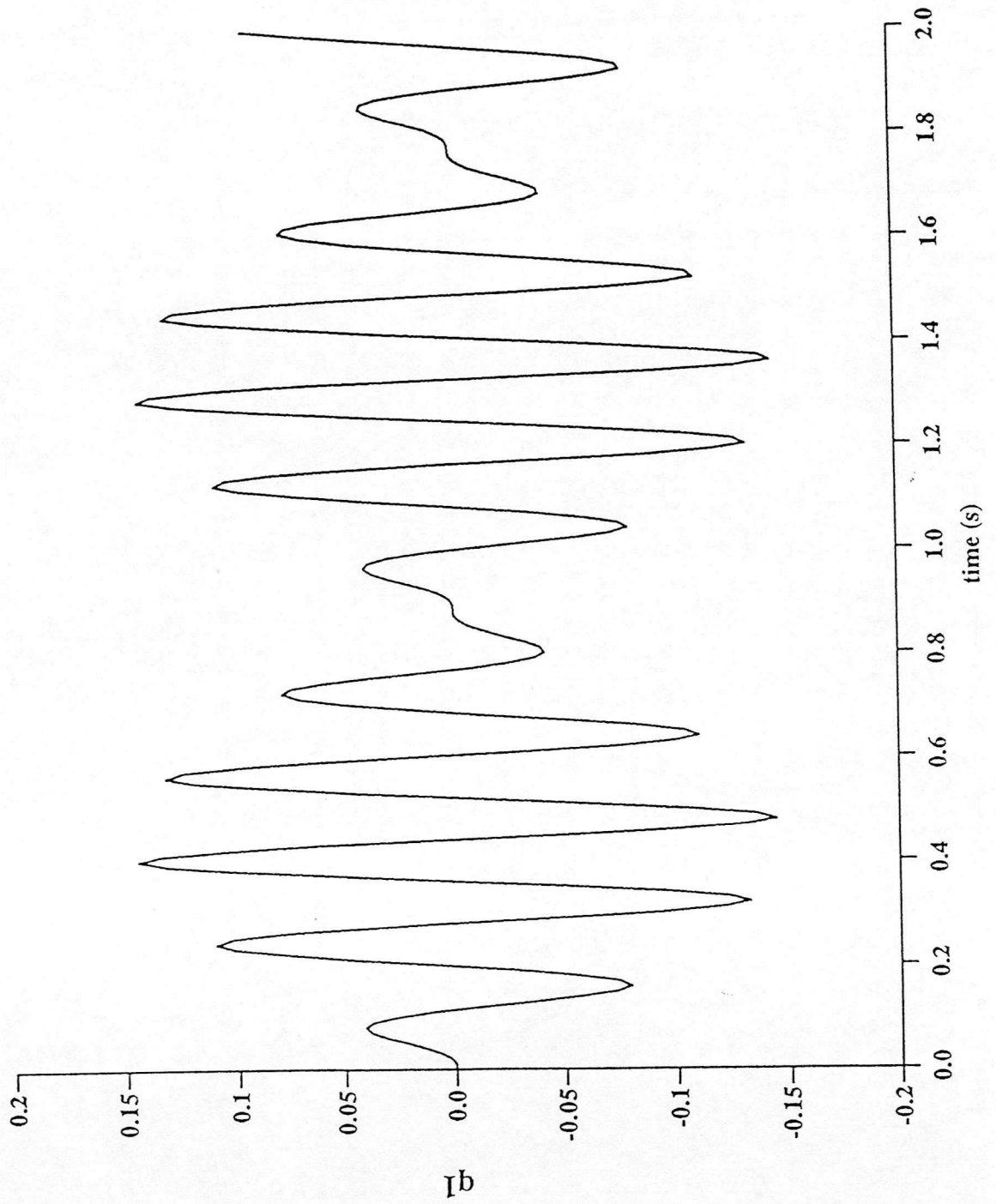
Figure A1.5

Comparison Between 'Measured' Strains and Reconstructed Strains

beam forced at 35.63 radians per second - t=0.5 secs
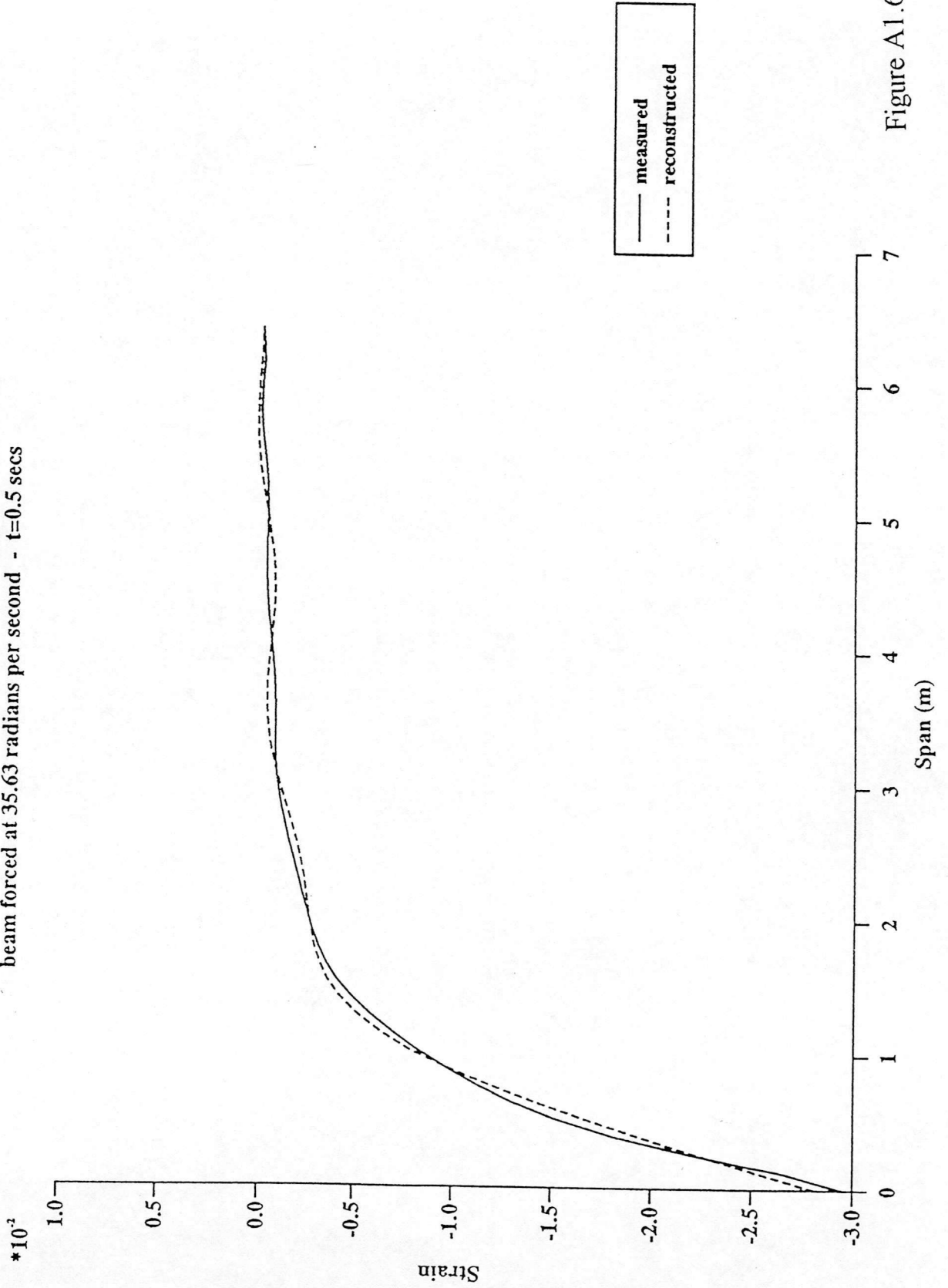
Figure A1.6

Comparison Between 'Measured' Displacements and Reconstructed Displacements

beam forced at 35.63 radians per second - t=0.5 secs
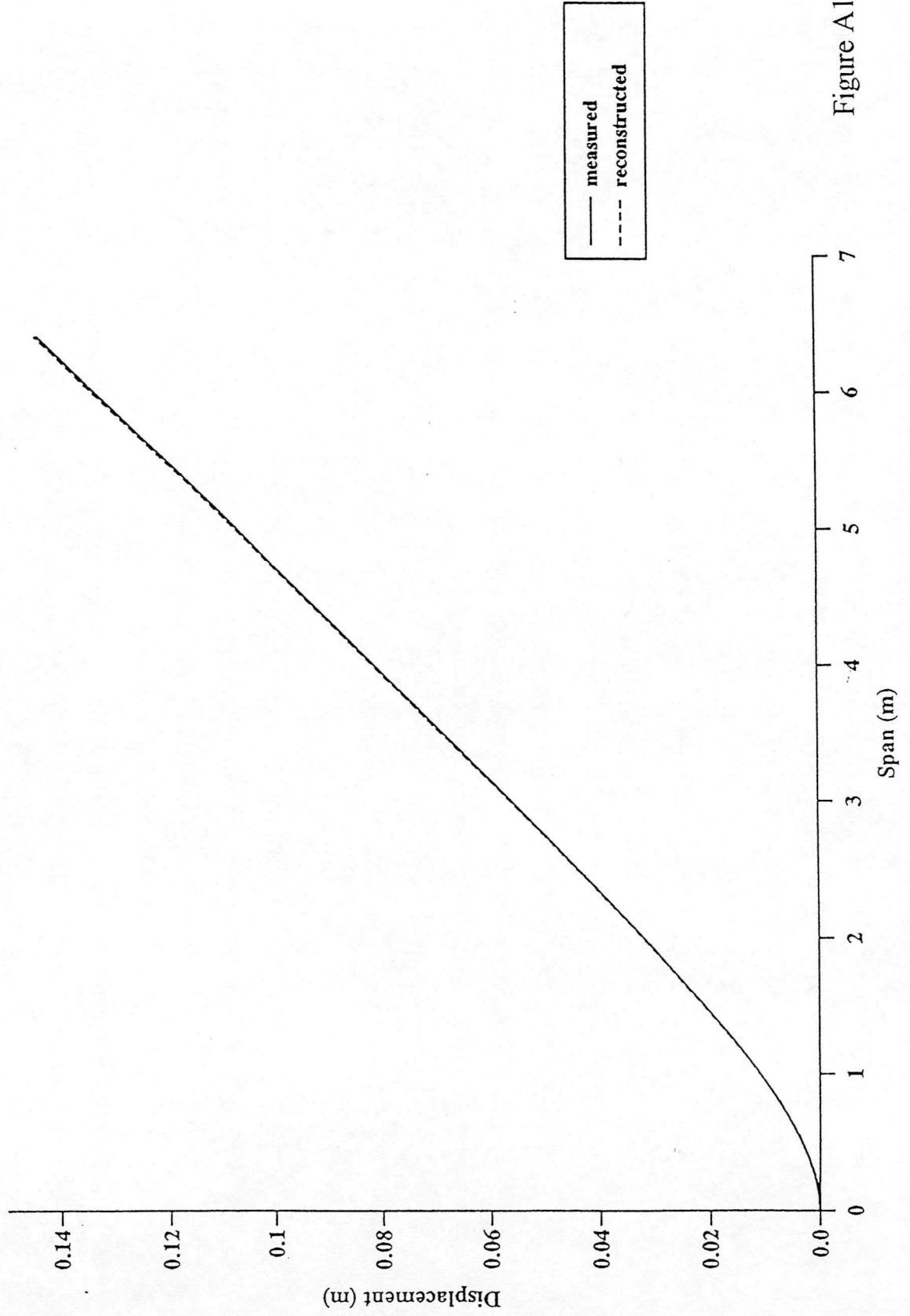
Figure A1.7

Comparison Between 'Measured' Strains and Reconstructed Strains

beam forced at 345 radians per second - t=0.5 secs
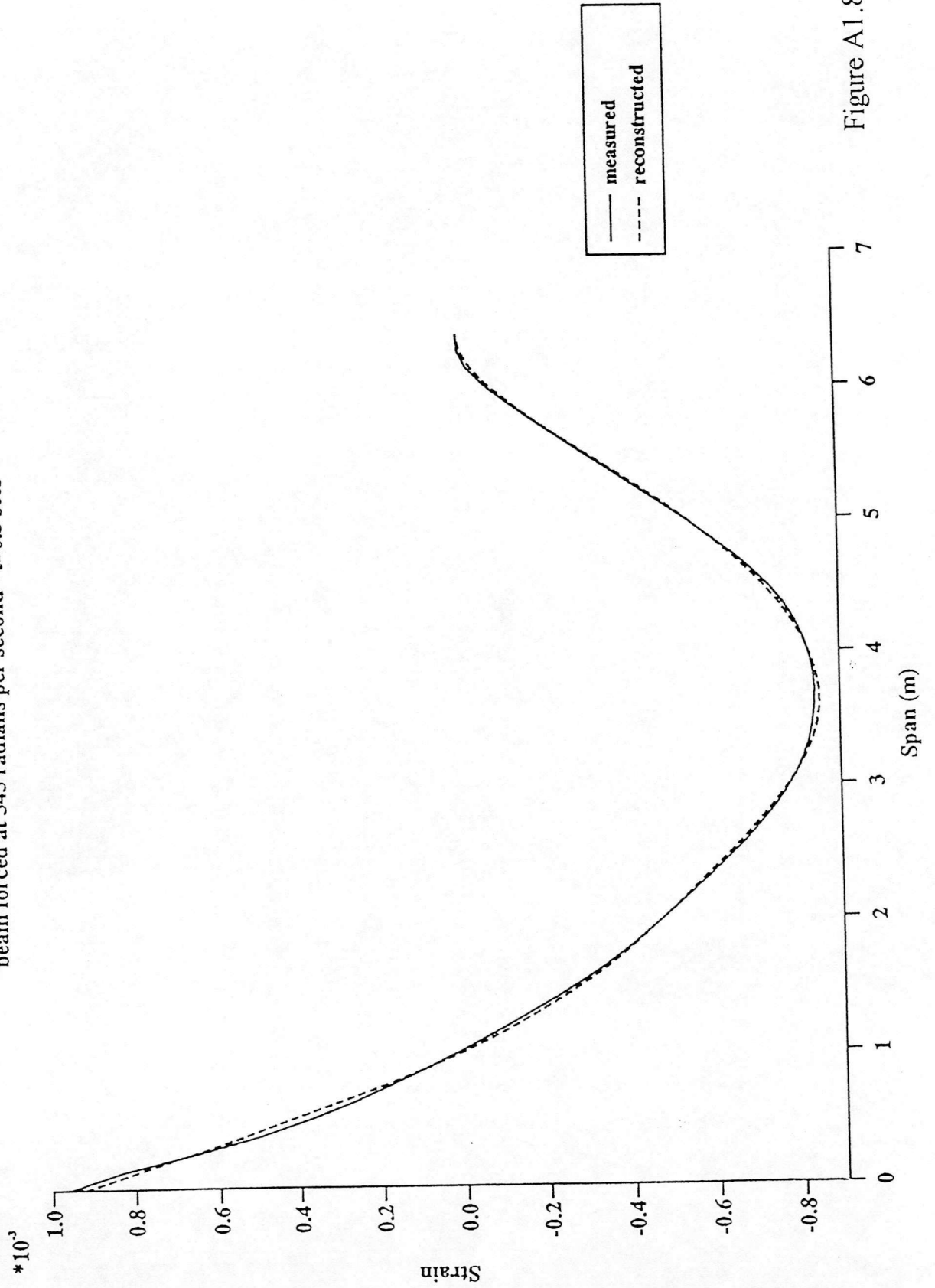
Figure A1.8

Comparison Between 'Measured' Displacements and Reconstructed Displacements

beam forced at 345 radians per second - t=0.5 secs

$*10^{-3}$
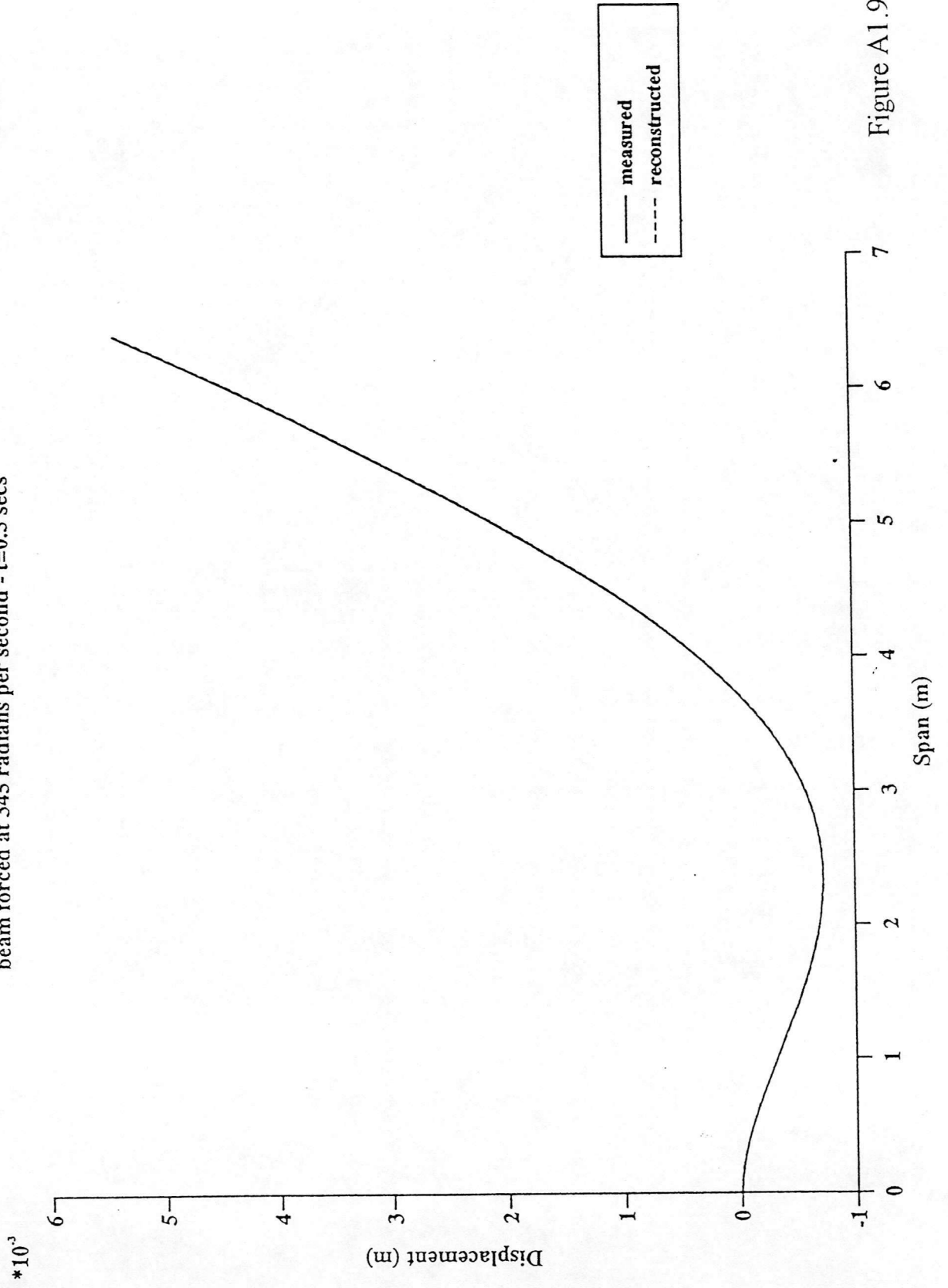
Figure A1.9

Comparison Between 'Measured' Strains and Reconstructed Strains

beam forced at 1533 radians per second - t=0.5 secs
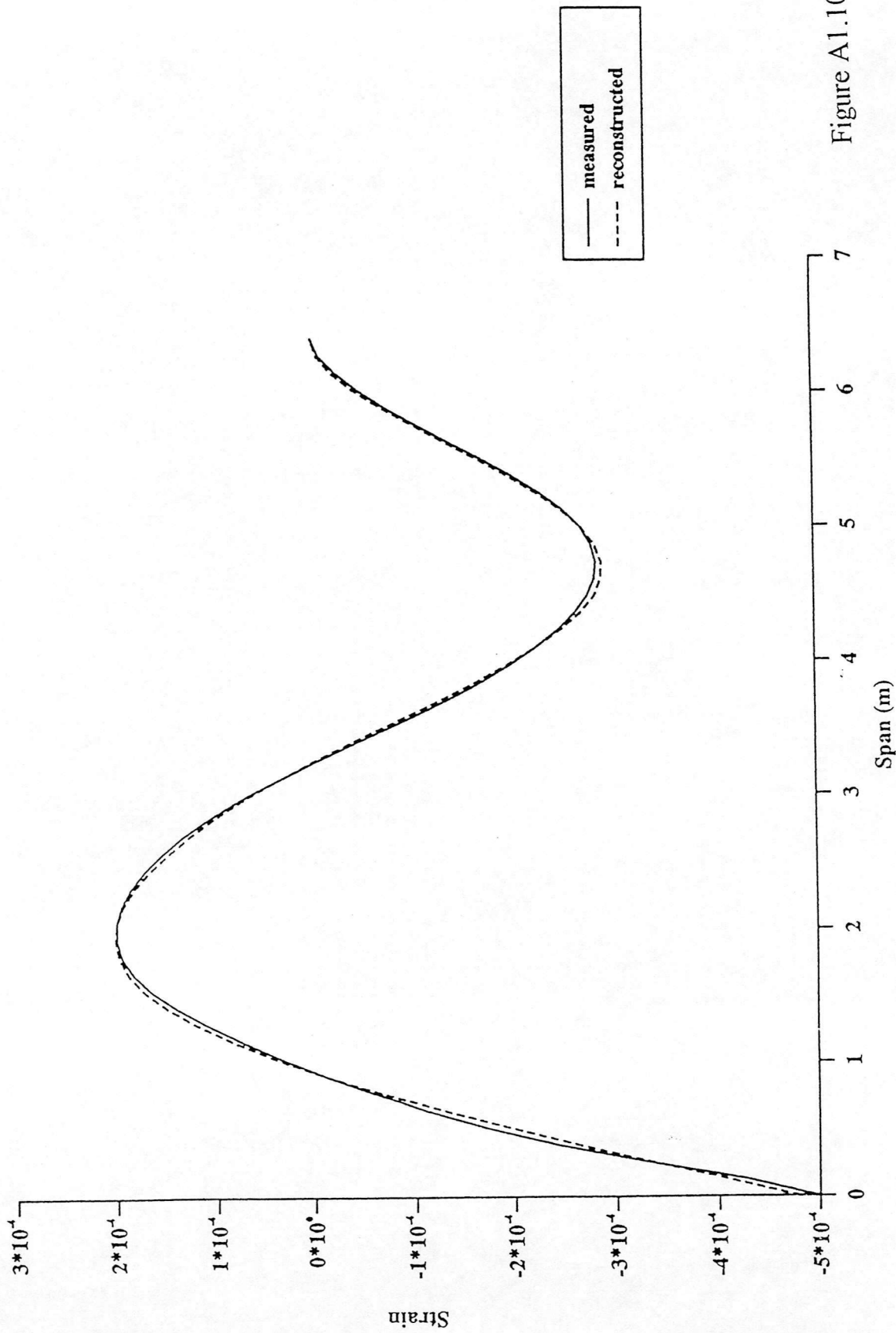
Figure A1.10

Comparison Between 'Measured' Displacements and Reconstructed Displacements

beam forced at 1533 radians per second - t=0.5 secs
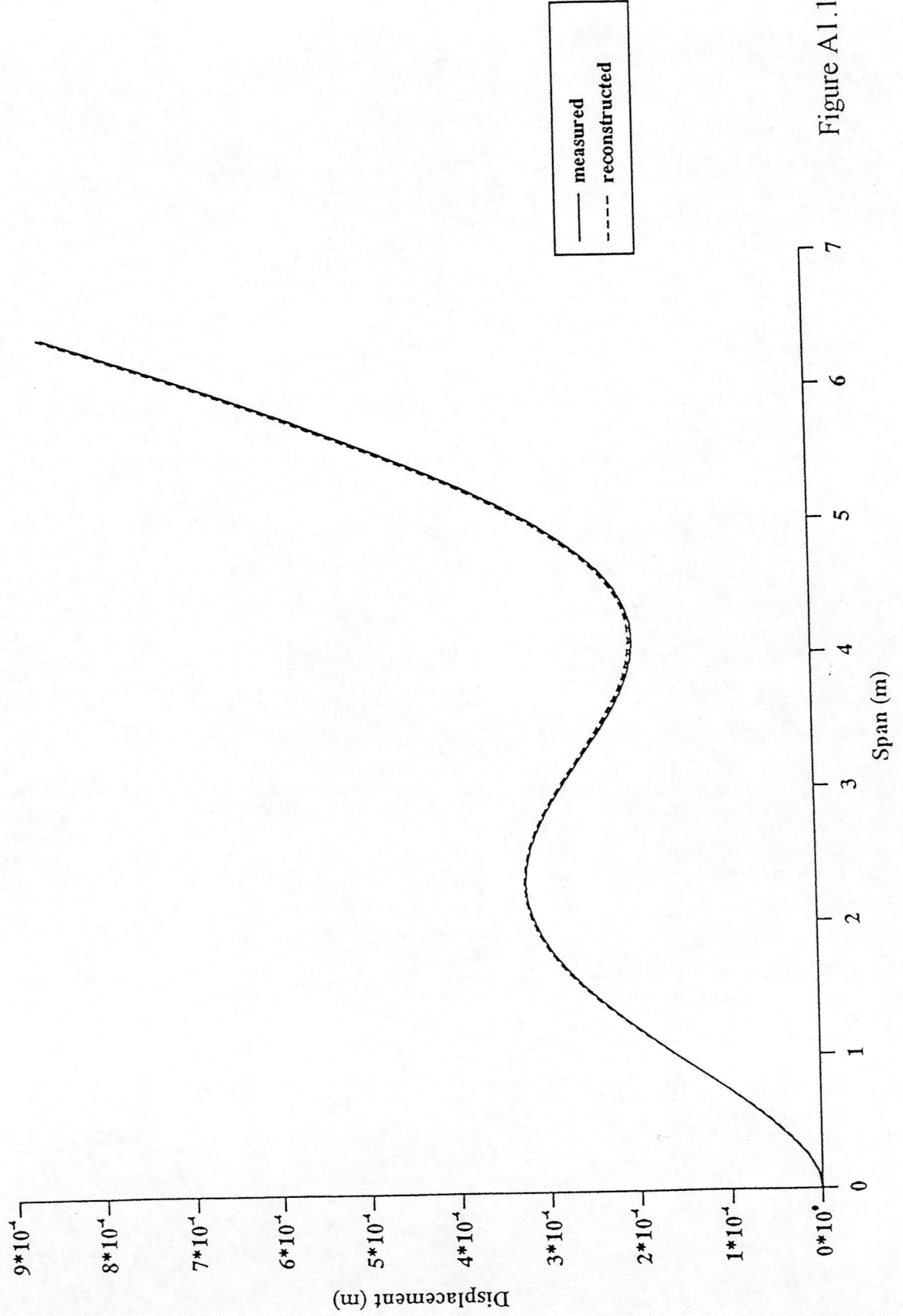
Figure A1.11

Blade Displacements Produced when Rotating at 35.63 Radians Per Second

4 degrees of collective - aerodynamic damping included
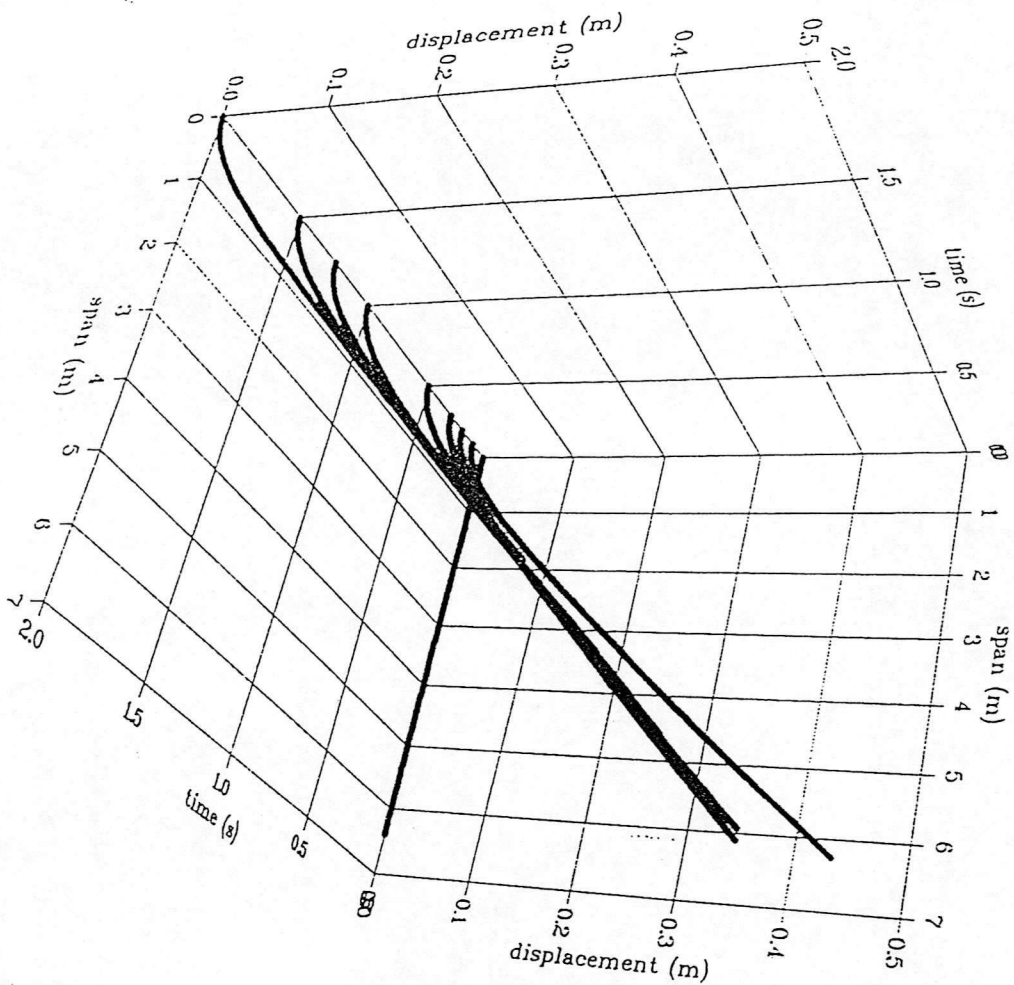
Figure A2.1

Weighting of first mode for blade rotating at 35.63 radians per second
4 degrees of collective applied - aerodynamic damping included
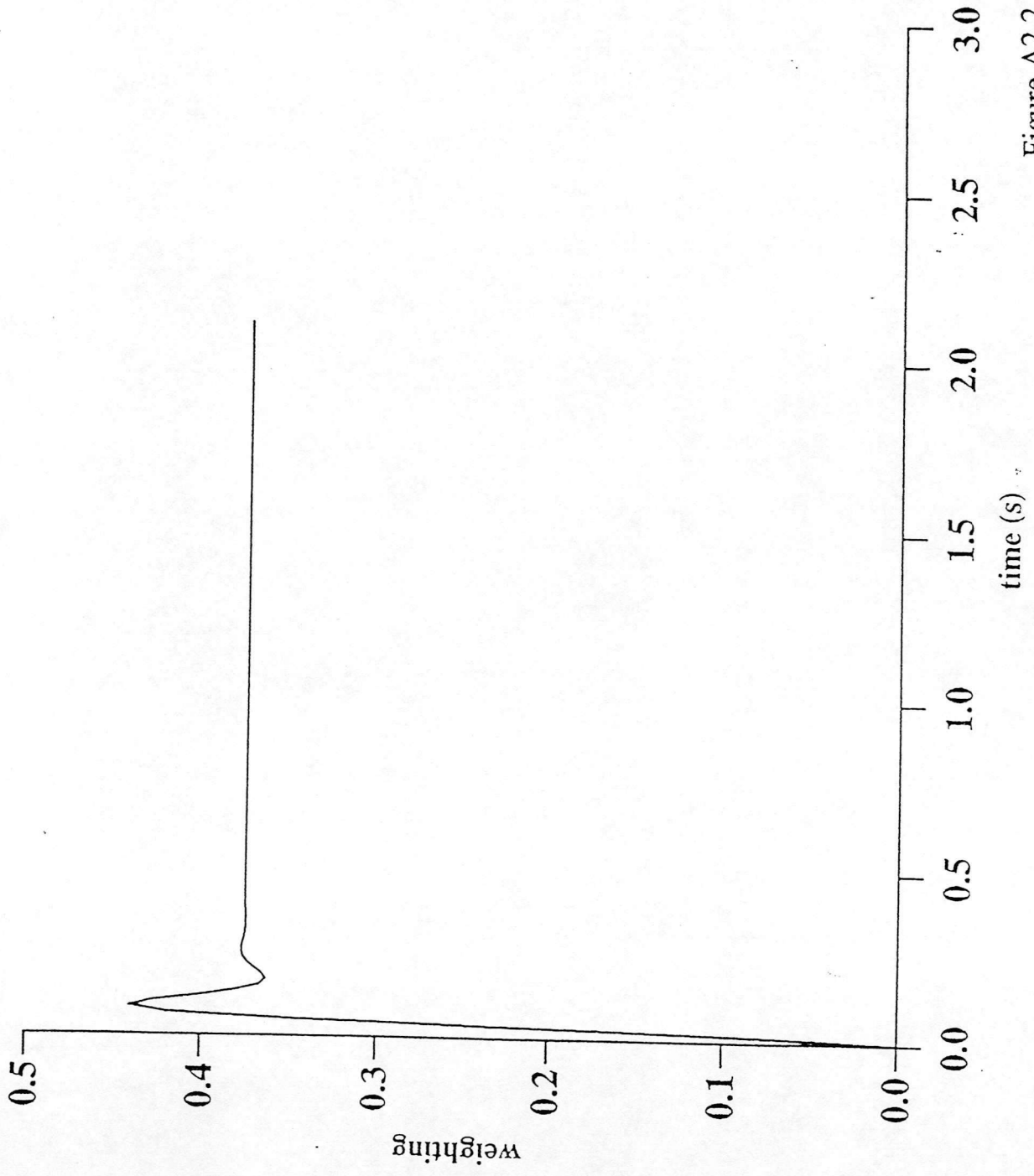
Figure A2.2

Weighting of Second mode for blade rotating at 35.63 radians per second

4 degrees of collective applied - aerodynamic damping included

*10⁻³
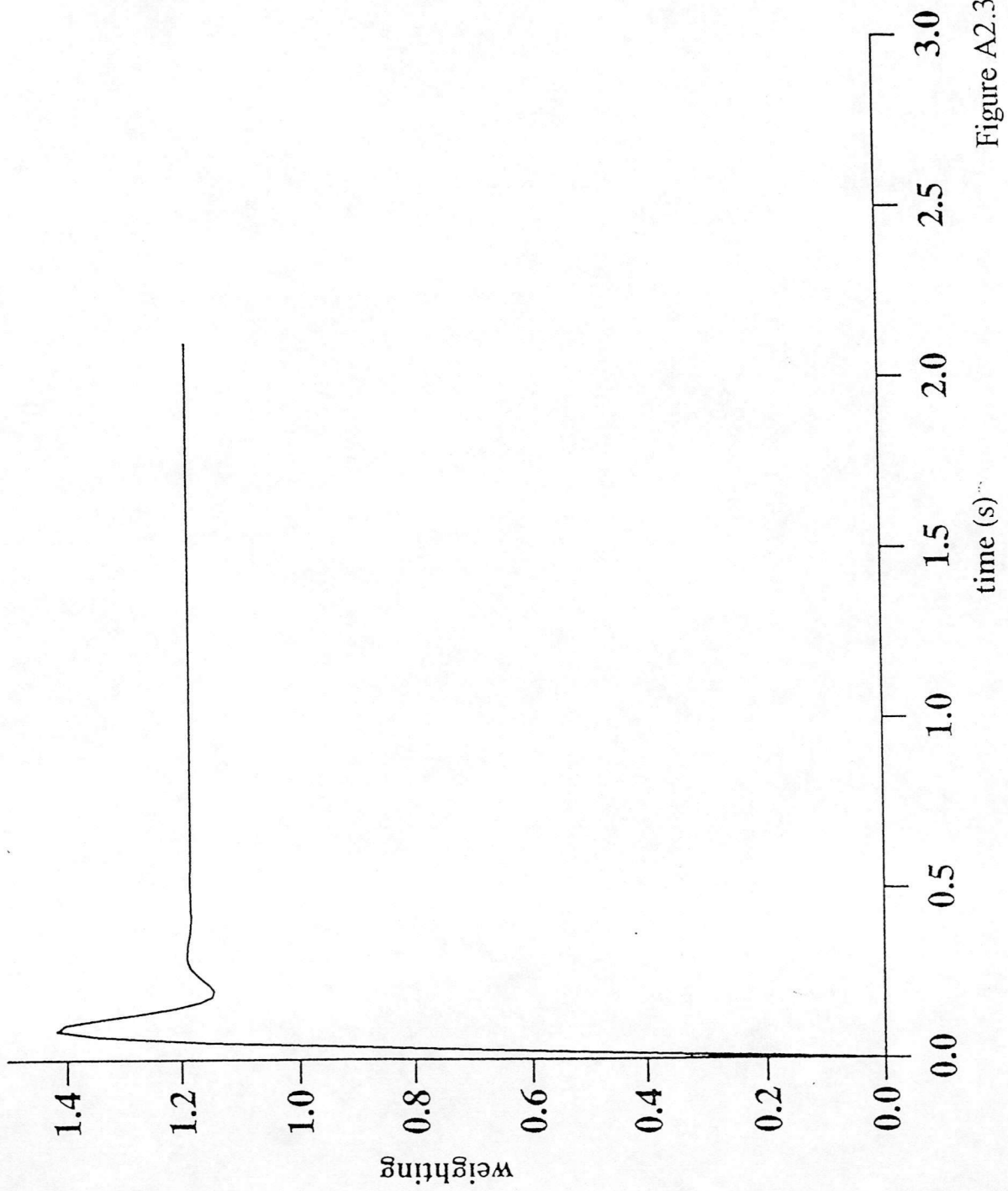
Figure A2.3

Weighting of third mode for blade rotating at 35.63 radians per second
4 degrees of collective applied - aerodynamic damping included

Figure A2.4

time (s)

weighting

0.0*10⁰ 5.0*10⁻⁸ 1.0*10⁻⁷ 1.5*10⁻⁷ 2.0*10⁻⁷ 2.5*10⁻⁷ 3.0*10⁻⁷ 3.5*10⁻⁷ 4.0*10⁻⁷

0.0 0.5 1.0 1.5 2.0 2.5 3.0
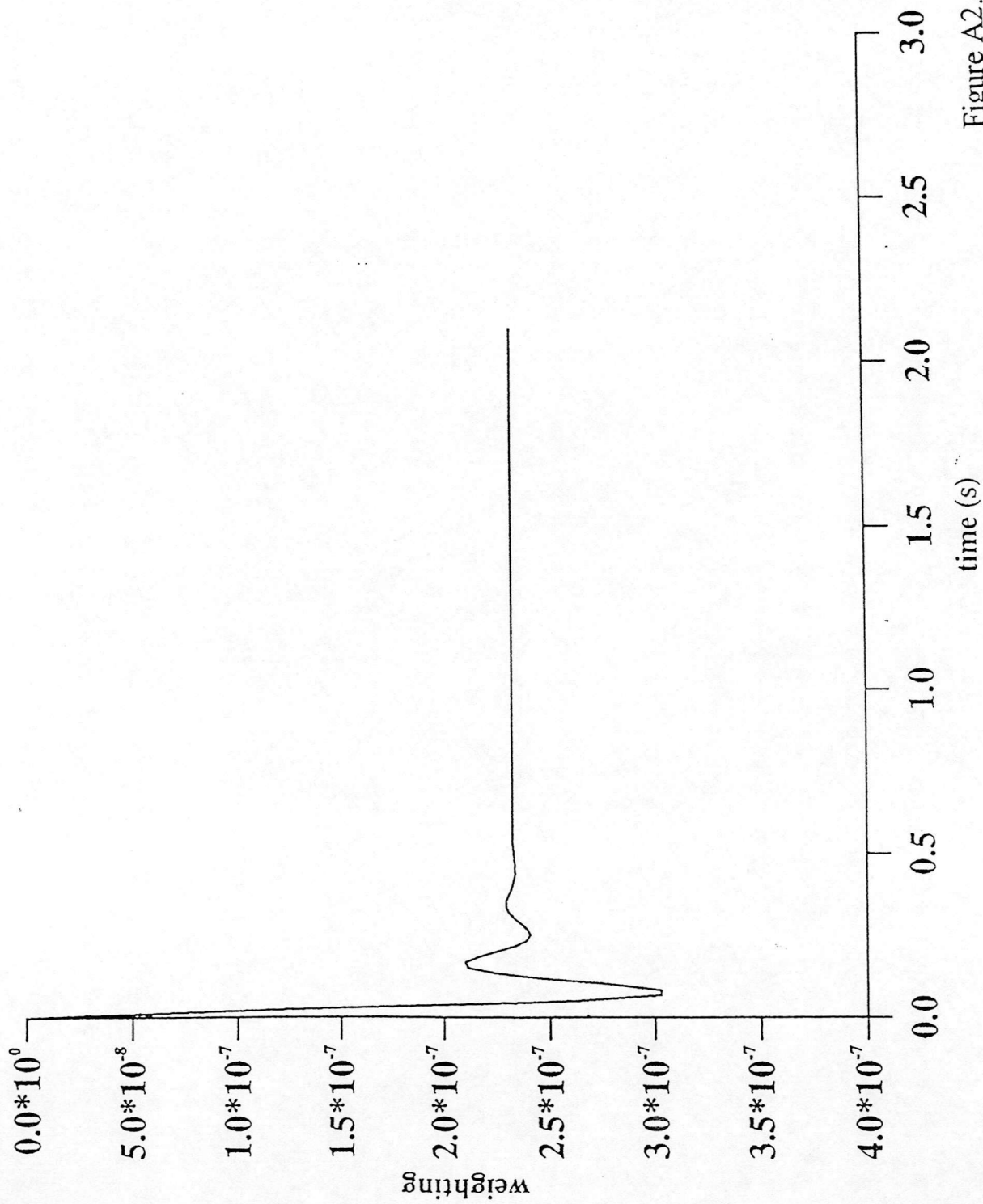
Blade Displacements Produced when Rotating at 35.63 Radians Per Second

0.4 degrees of longitudinal cyclic - aerodynamic damping included
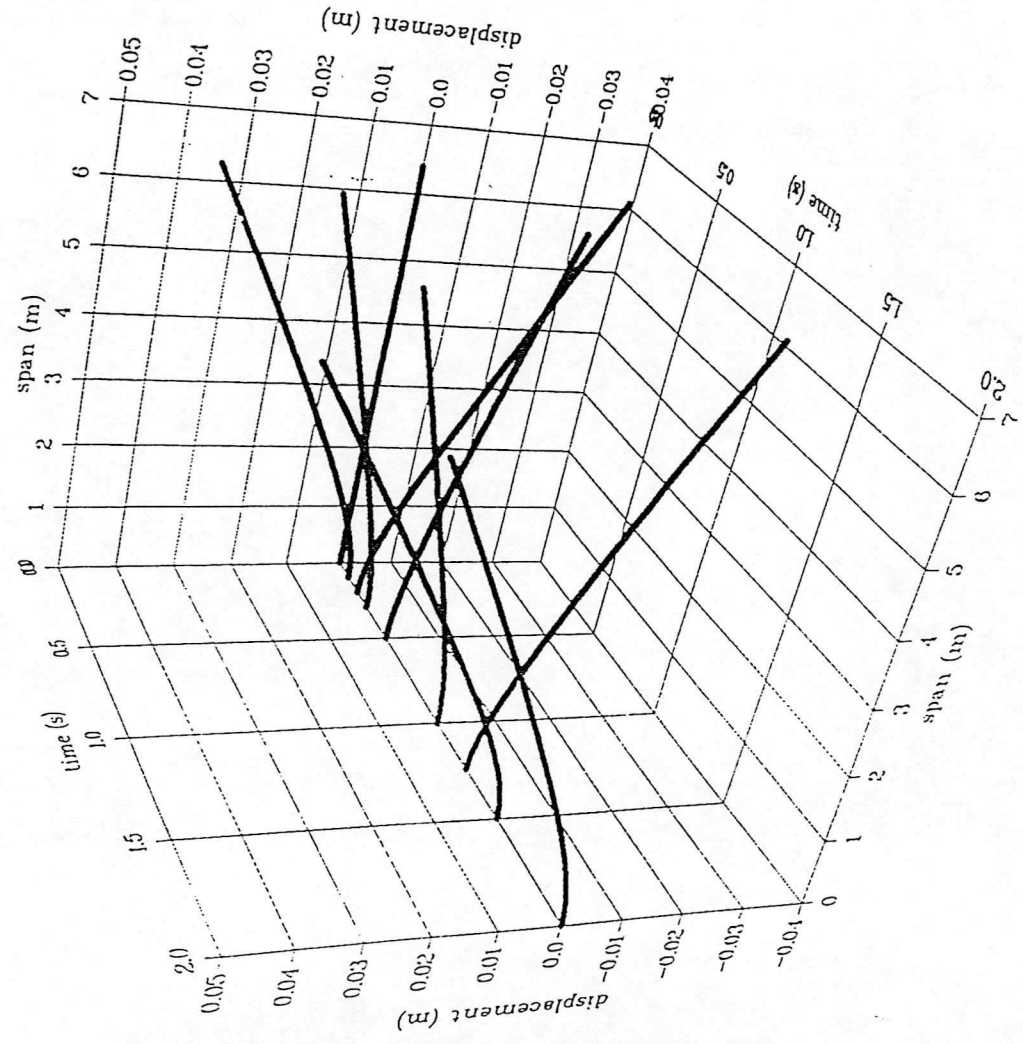
Figure A2.5

Weighting of First Mode for Blade rotating at 35.63 Radians Per Second

0.4 degrees of longitudinal cyclic - aerodynamic damping included
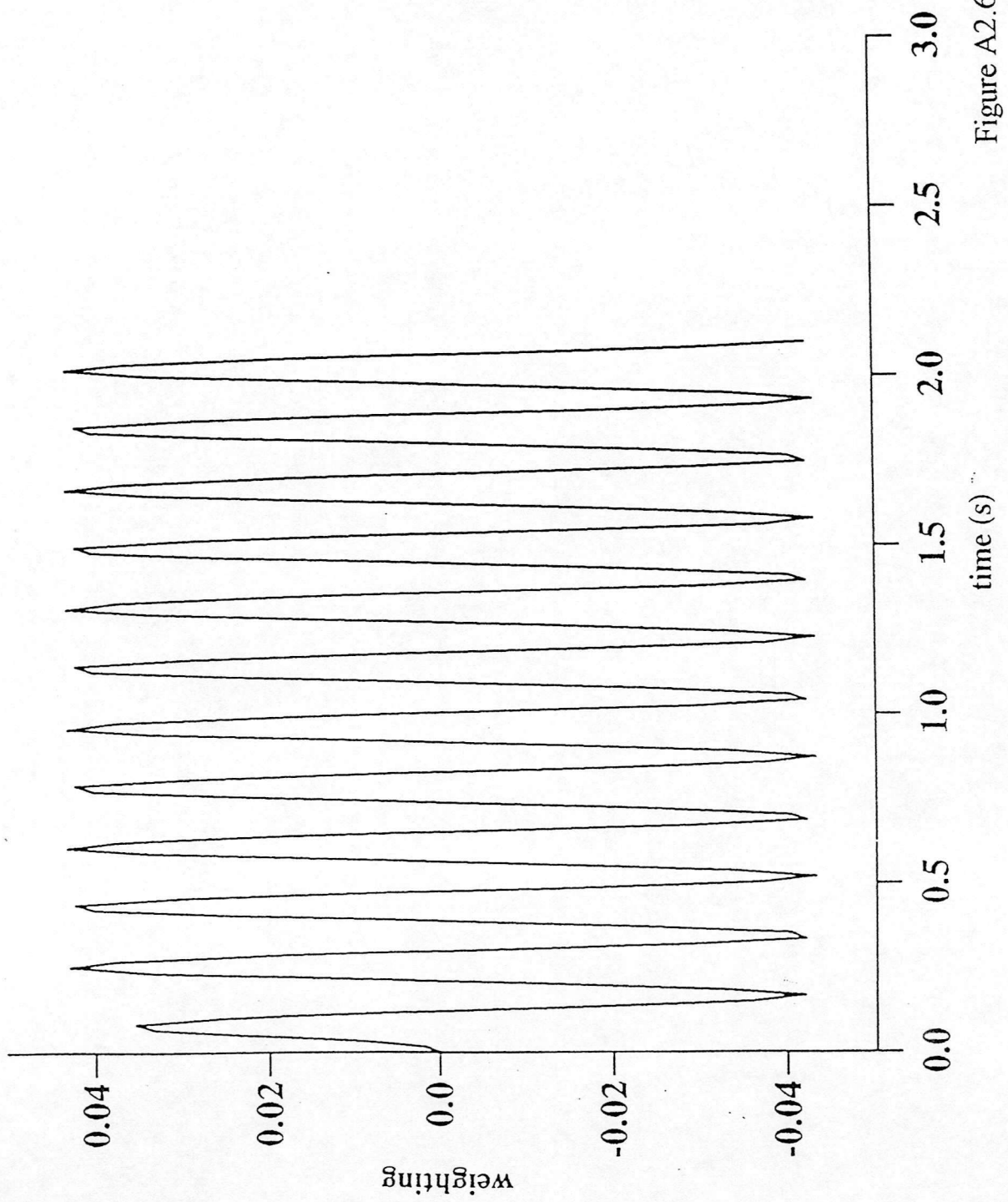
Figure A2.6

Blade Displacements Produced when Rotating at 35.63 Radians Per Second

4 degrees of collective - v0=5m/s
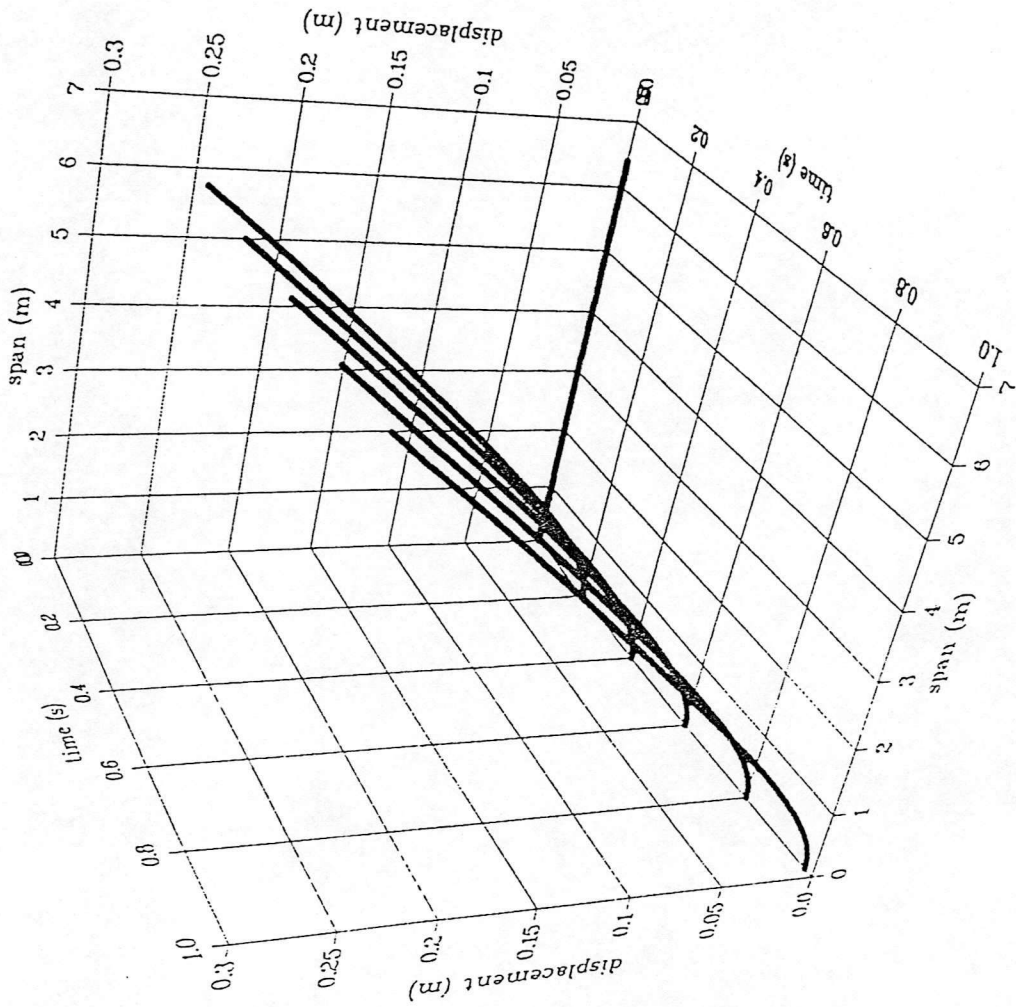
Figure A2.7

Weighting of first mode for blade rotating at 35.63 radians per second
4 degrees of collective - v0=5m/s
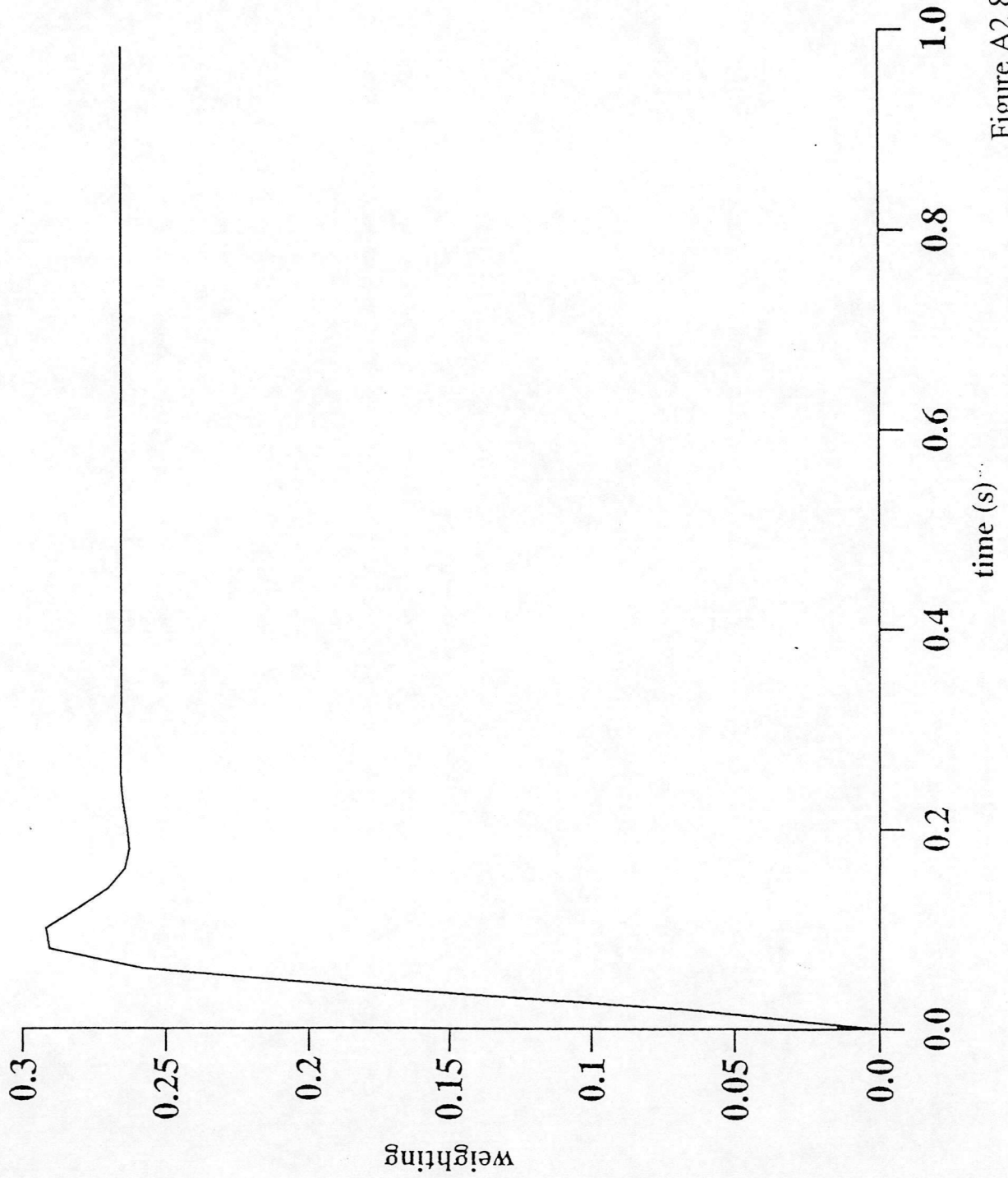
Figure A2.8

Comparison Between Reconstructed, Measured and Actual Strain Distributions

no noise superimposed on measured strain distribution
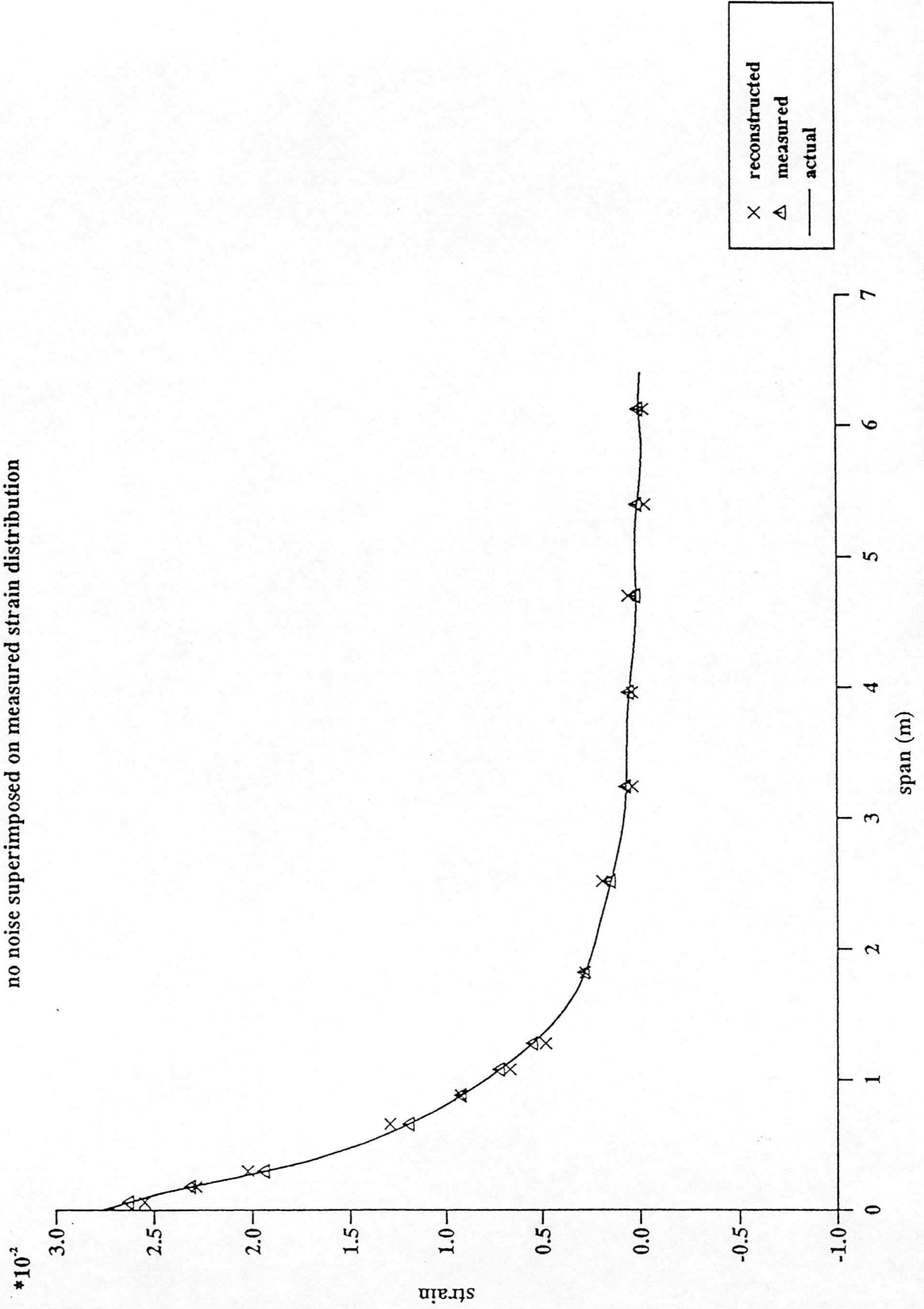
Figure A2.9

Comparison Between Reconstructed Measured and Actual Displacement

no noise superimposed on measured strain pattern
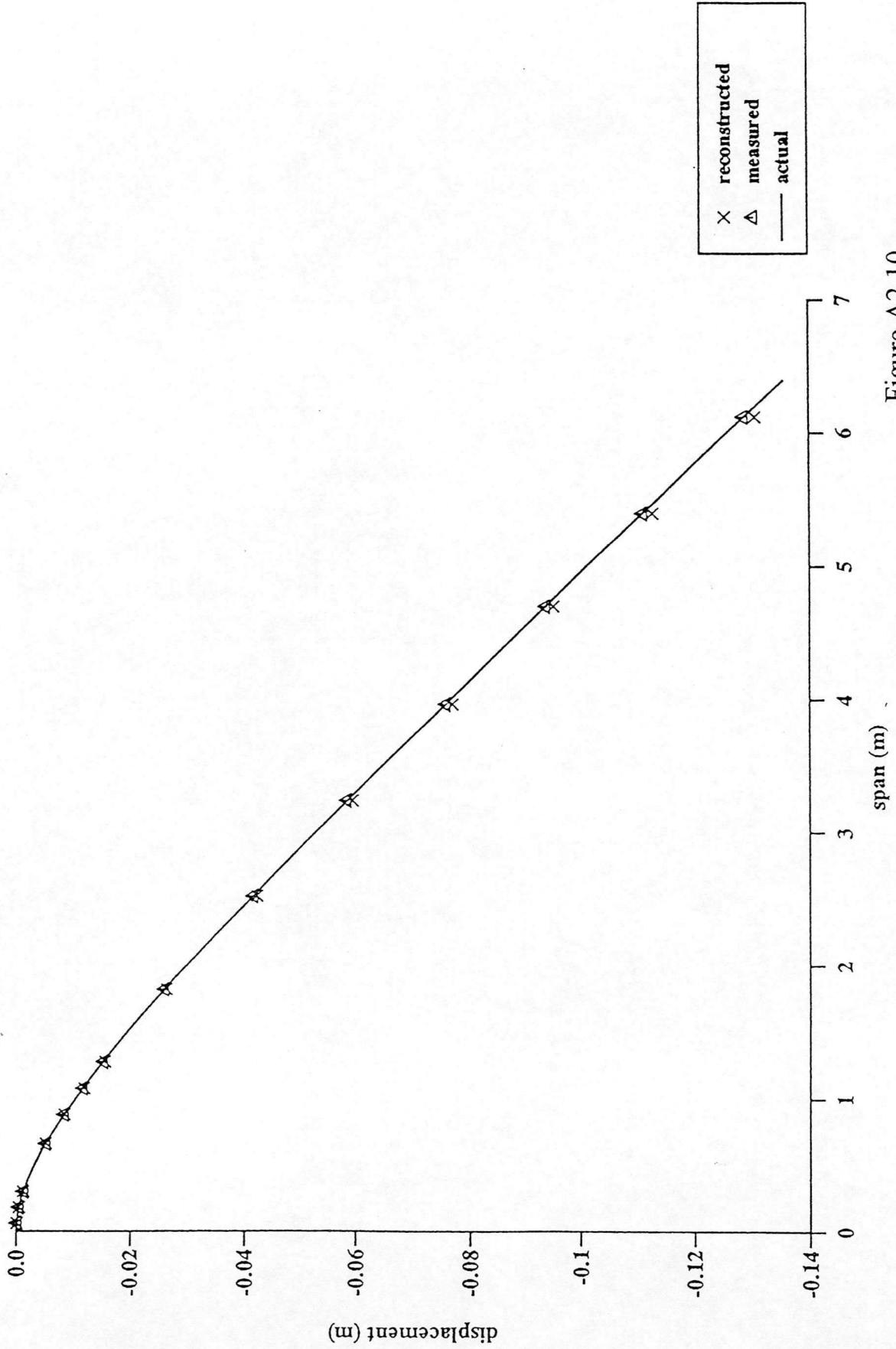
Figure A2.10

Comparison Between Reconstructed, Measured and Actual Strain Distributions

noise - zero mean with standard deviation of 5% of measured value
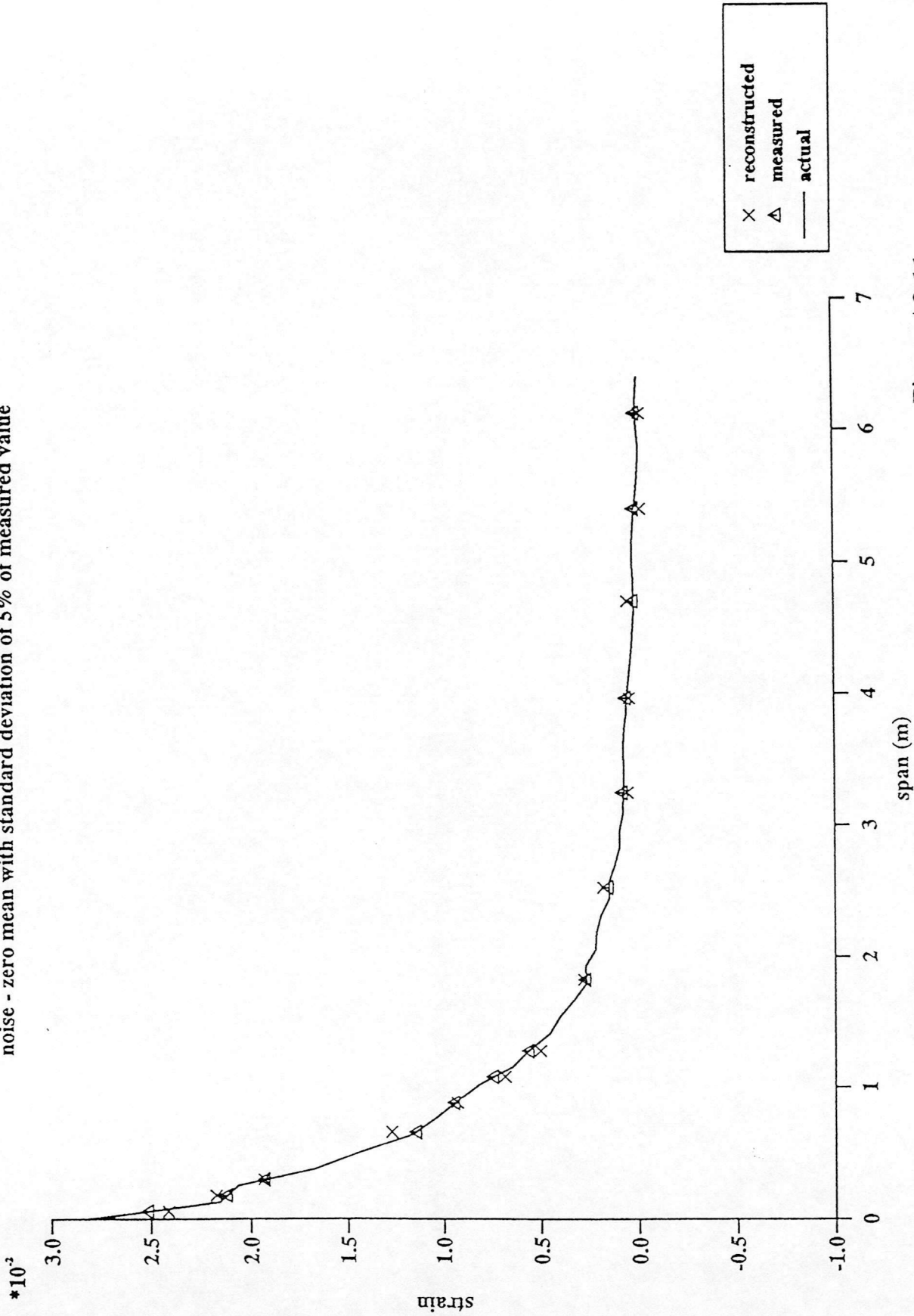
Figure A2.11

Comparison Between Reconstructed Measured and Actual Displacement

noise - zero mean with standard deviation of 5% of measured value
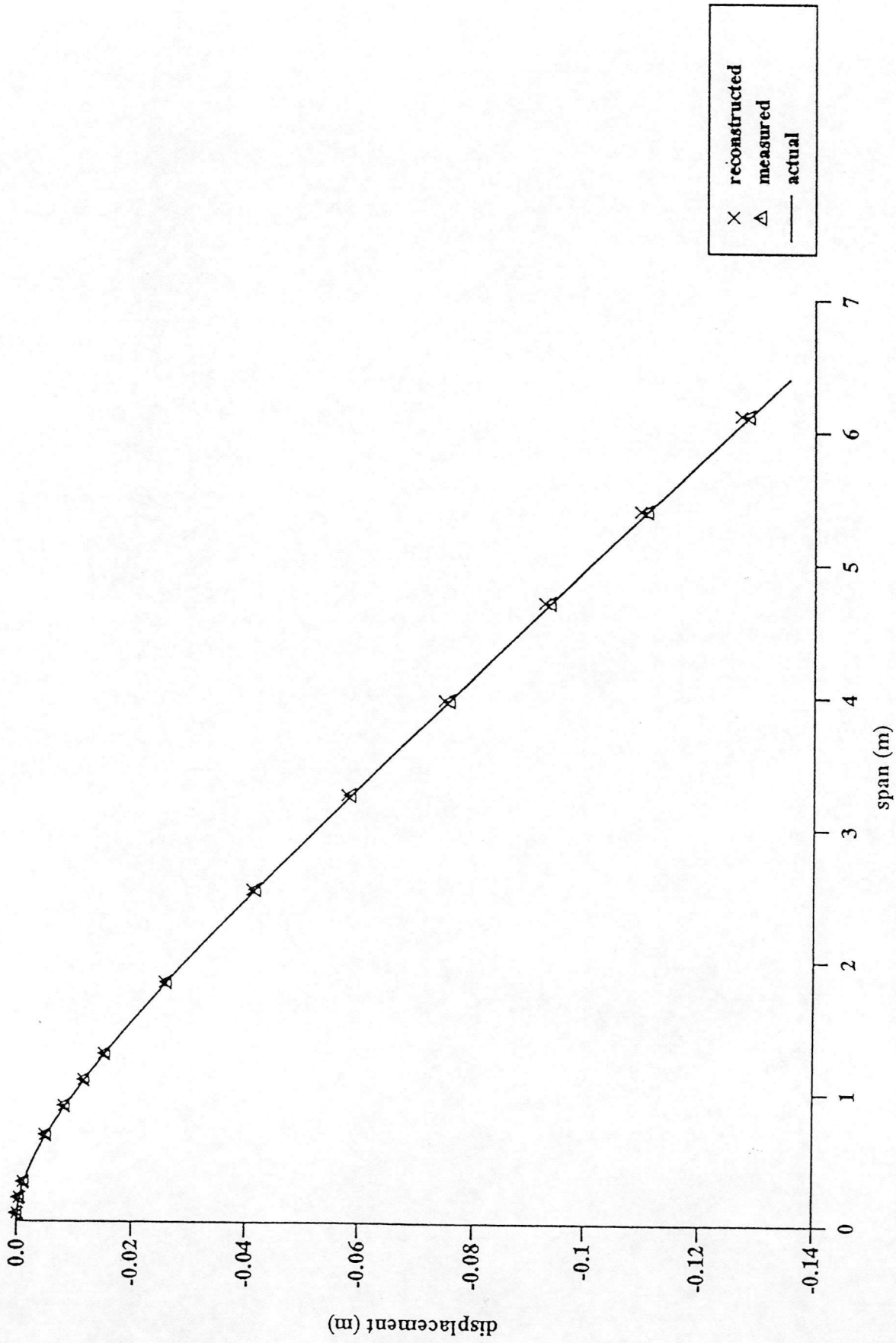
Figure A2.12

Comparison Between Actual and Reconstructed Strain Distributions

noise - zero mean with a standard deviation of 5% of mean strain

4th strain guage failed
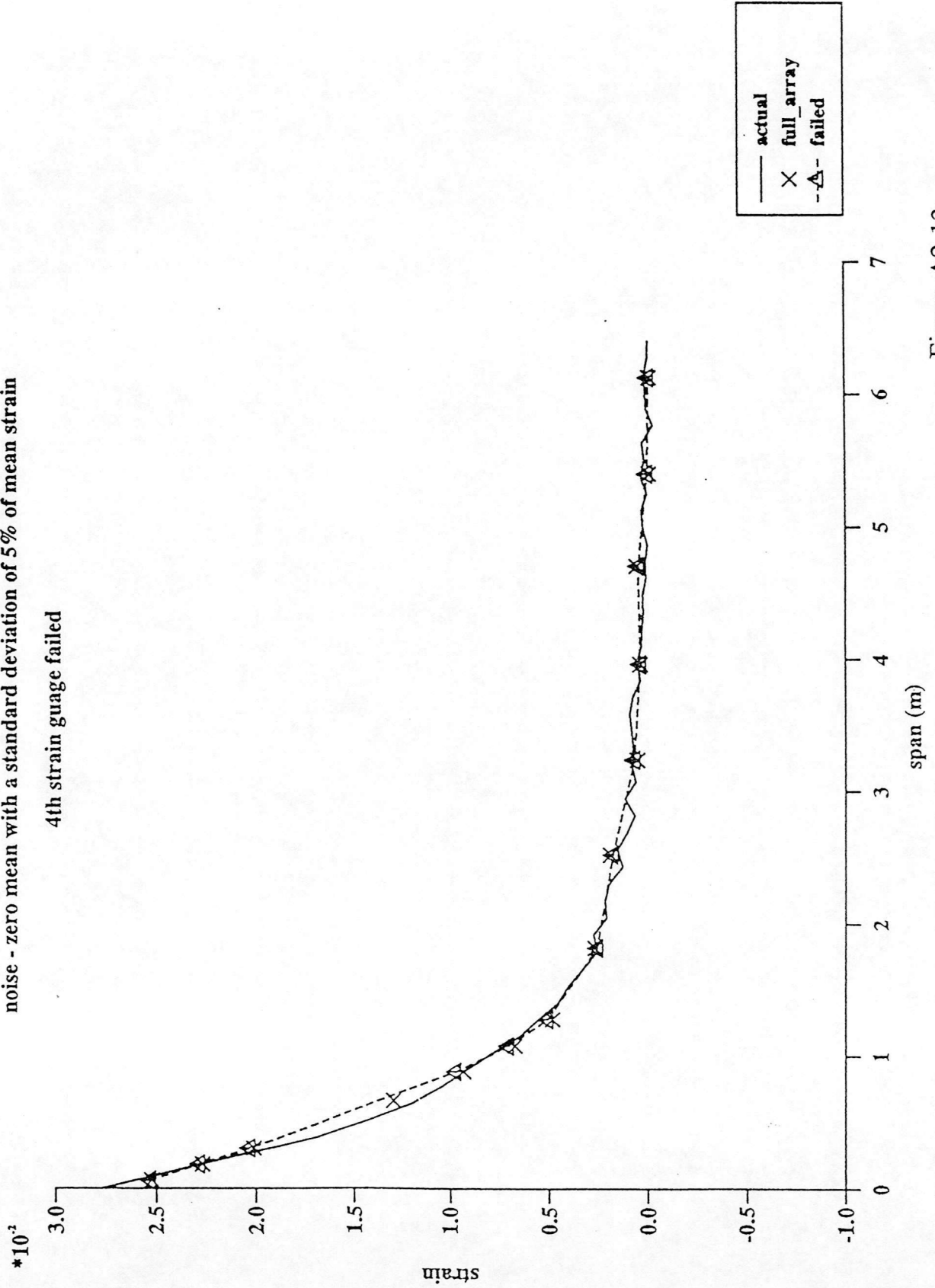
Figure A2.13

Comparison Between Actual and Reconstructed Displacements

noise - zero mean with a standard deviation of 5% of mean strain

4th strain guage failed
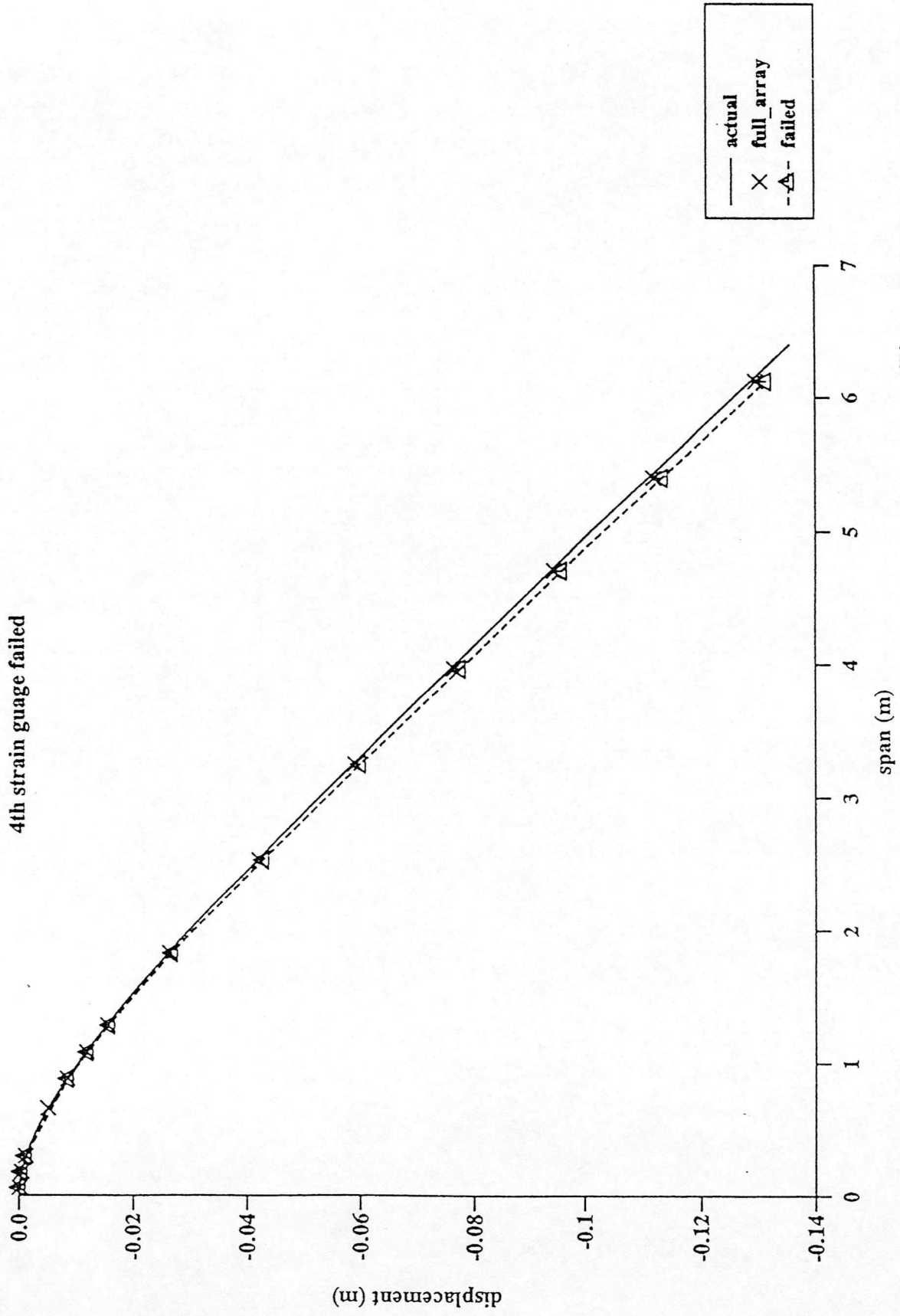
Figure A2.14

Comparison Between Actual and Reconstructed Strain Distributions

noise - zero mean with a standard deviation of 5% of mean strain

14th strain guage failed
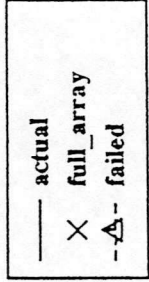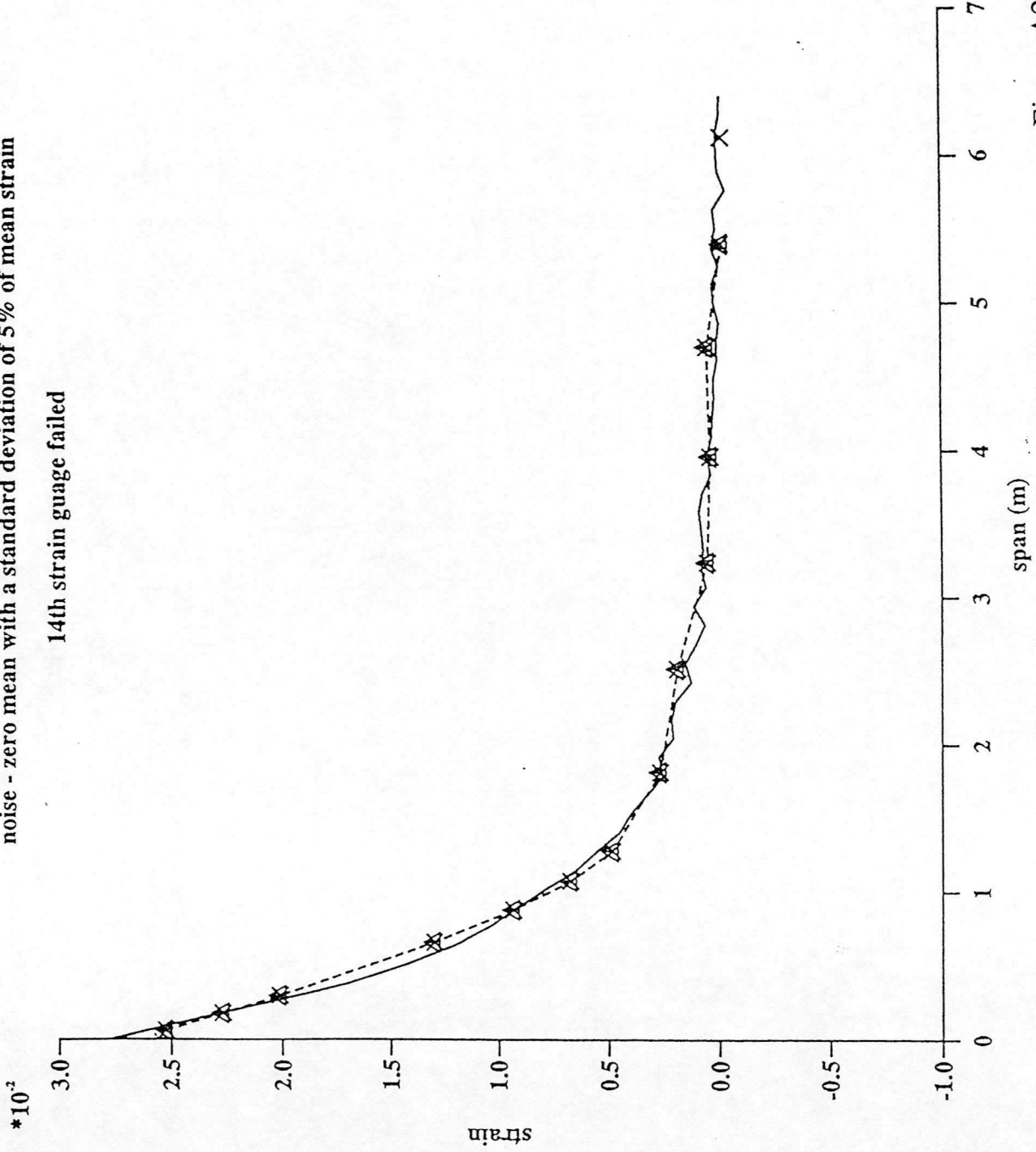
Figure A2.15

Comparison Between Actual and Reconstructed Displacements

noise - zero mean with a standard deviation of 5% of mean strain

14th strain guage failed
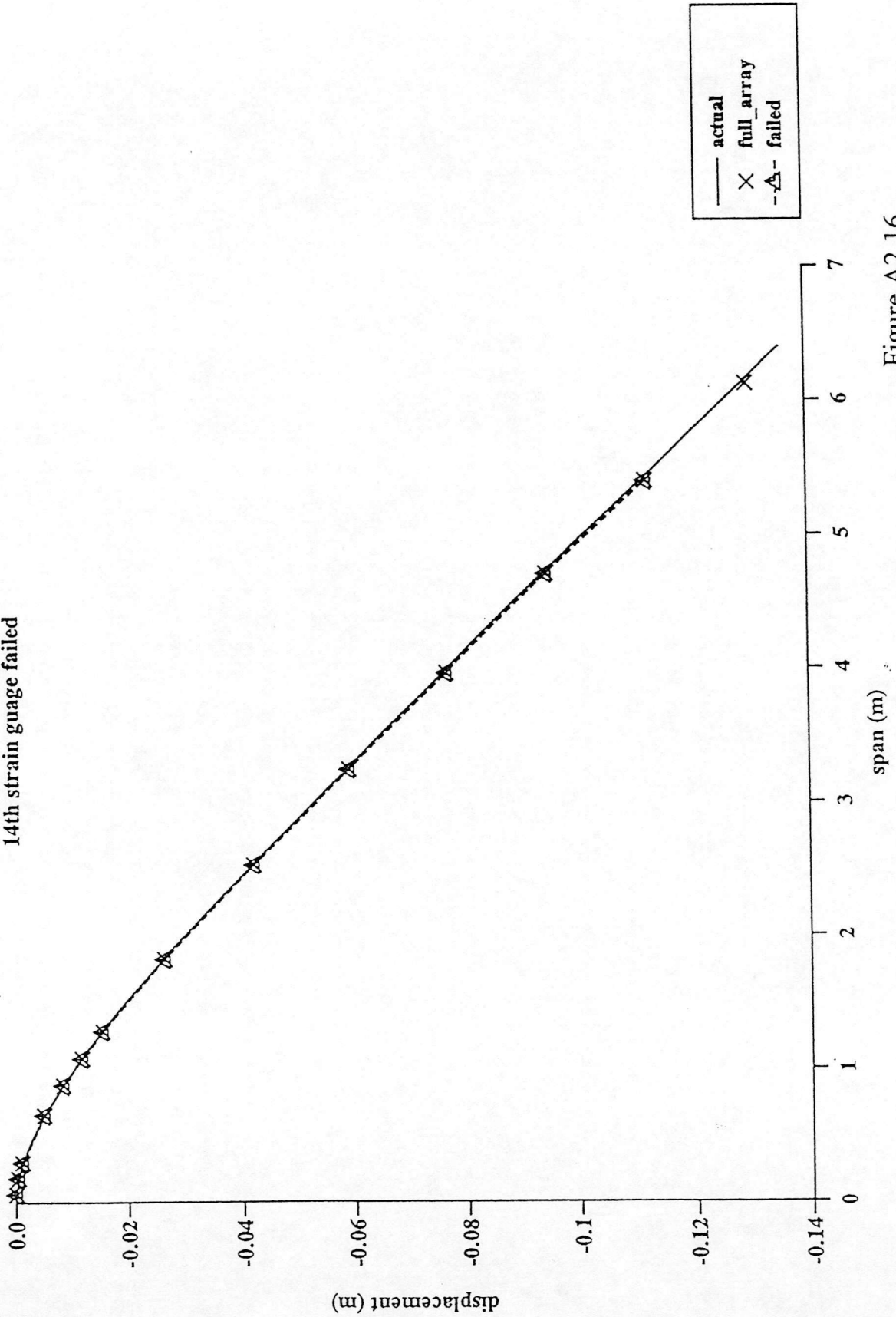
Figure A2.16
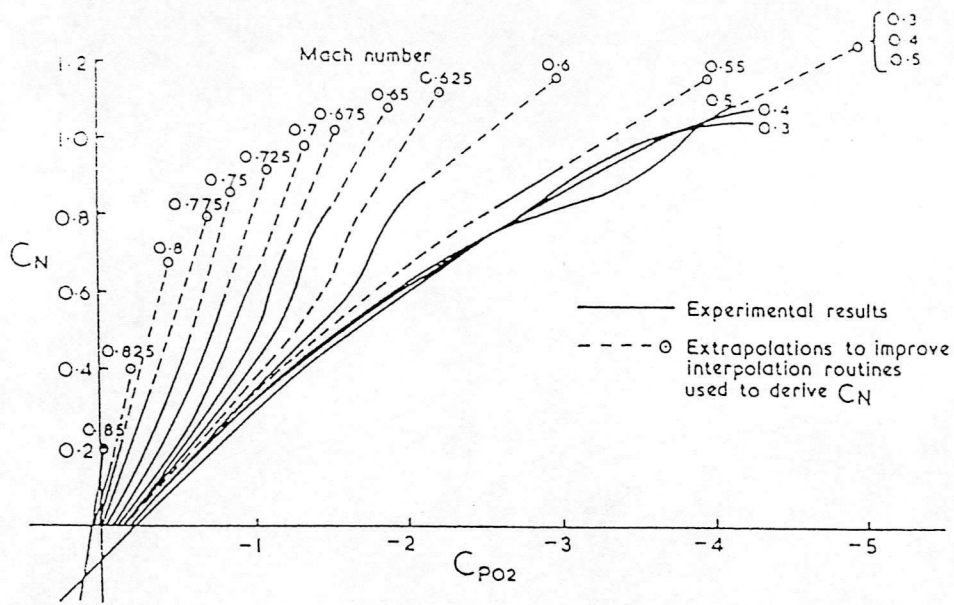
Figure A2.17 - Correlation Between Lift and Upper Surface Pressure at 2% Chord
(from Riley et al 1988)
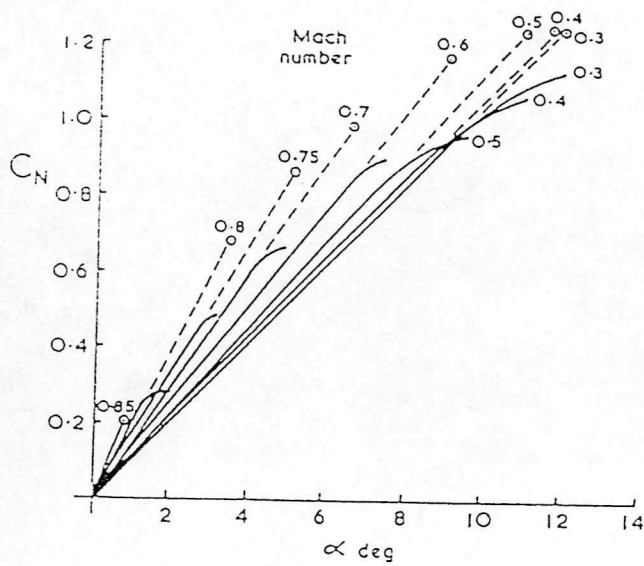
Figure A2.18 - Correlation Between Lift and Incidence
(from Riley et al 1988)

Comparison Between Actual and Measured Angle of Attack

4 degrees of collective   v0=5m/s

t=0.4   std=5%

alpha (degrees)

span (m)
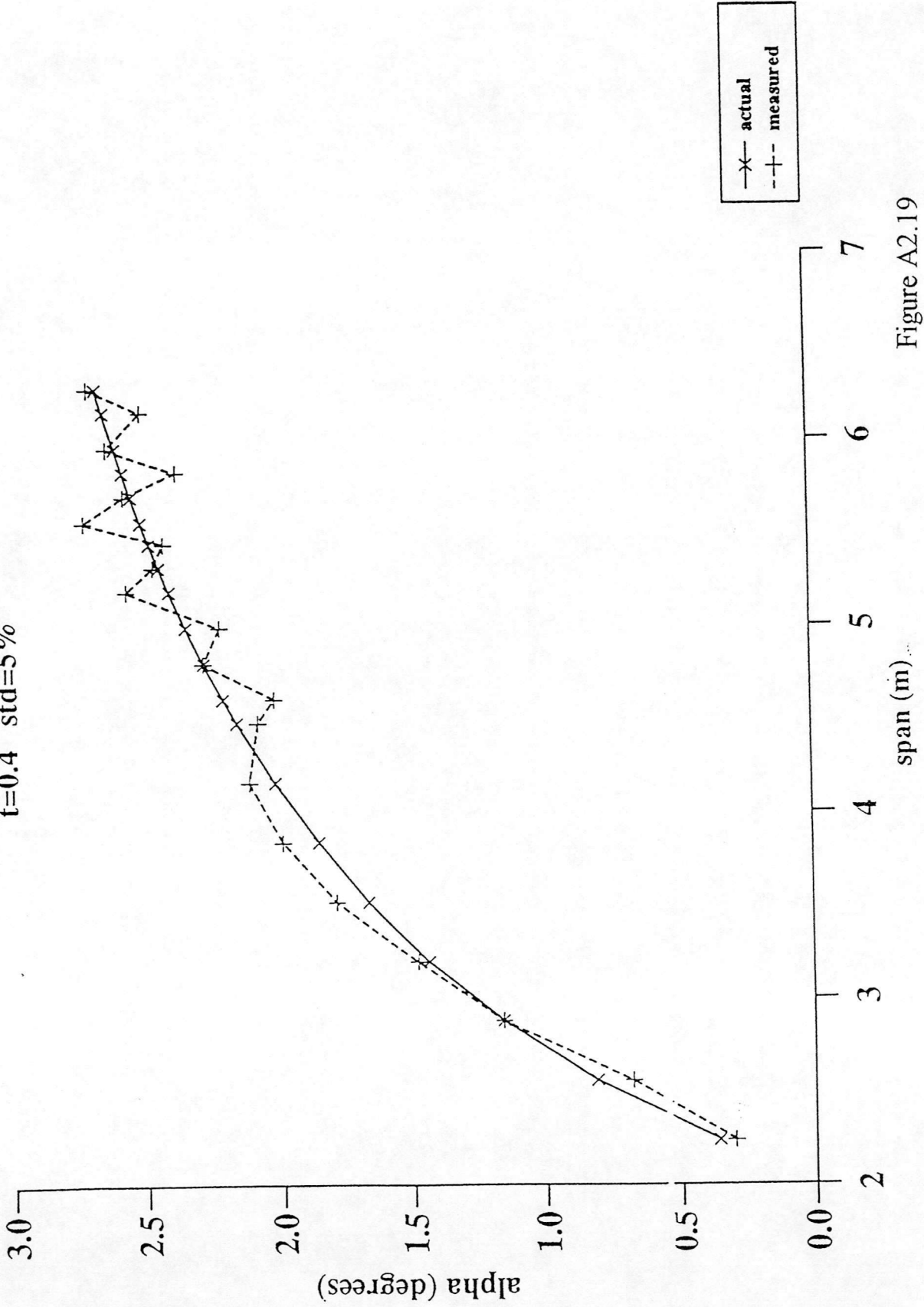
actual
measured

Figure A2.19

Comparison Between Actual and Reconstructed Induced Flow Velocity

4 Degrees of Collective, 0.4 Degrees of Lateral and Longitudinal Cyclic

v0=5m/s   v1c=1m/s   v1s=1m/s   t=0.475s   tstep=0.005s
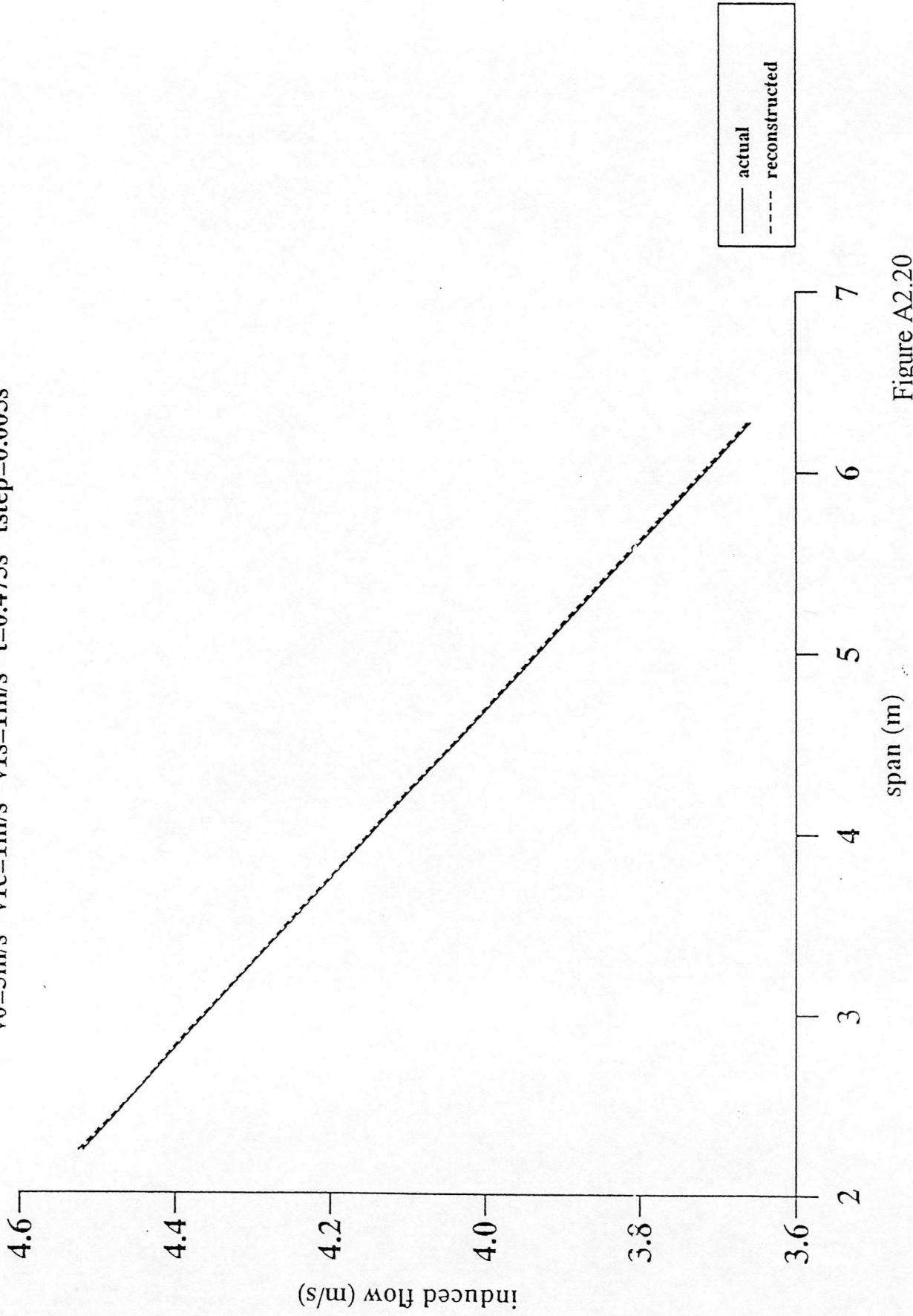
Figure A2.20

Comparison Between Actual and Reconstructed Induced Flow Velocity

4 Degrees of Collective, 0.4 Degrees of Lateral and Longitudinal Cyclic

$v0=5m/s$ $v1c=1m/s$ $v1s=1m/s$ $t=0.475s$ $tstep=0.005s$

5% std noise on "measured" Cp02 Distribution
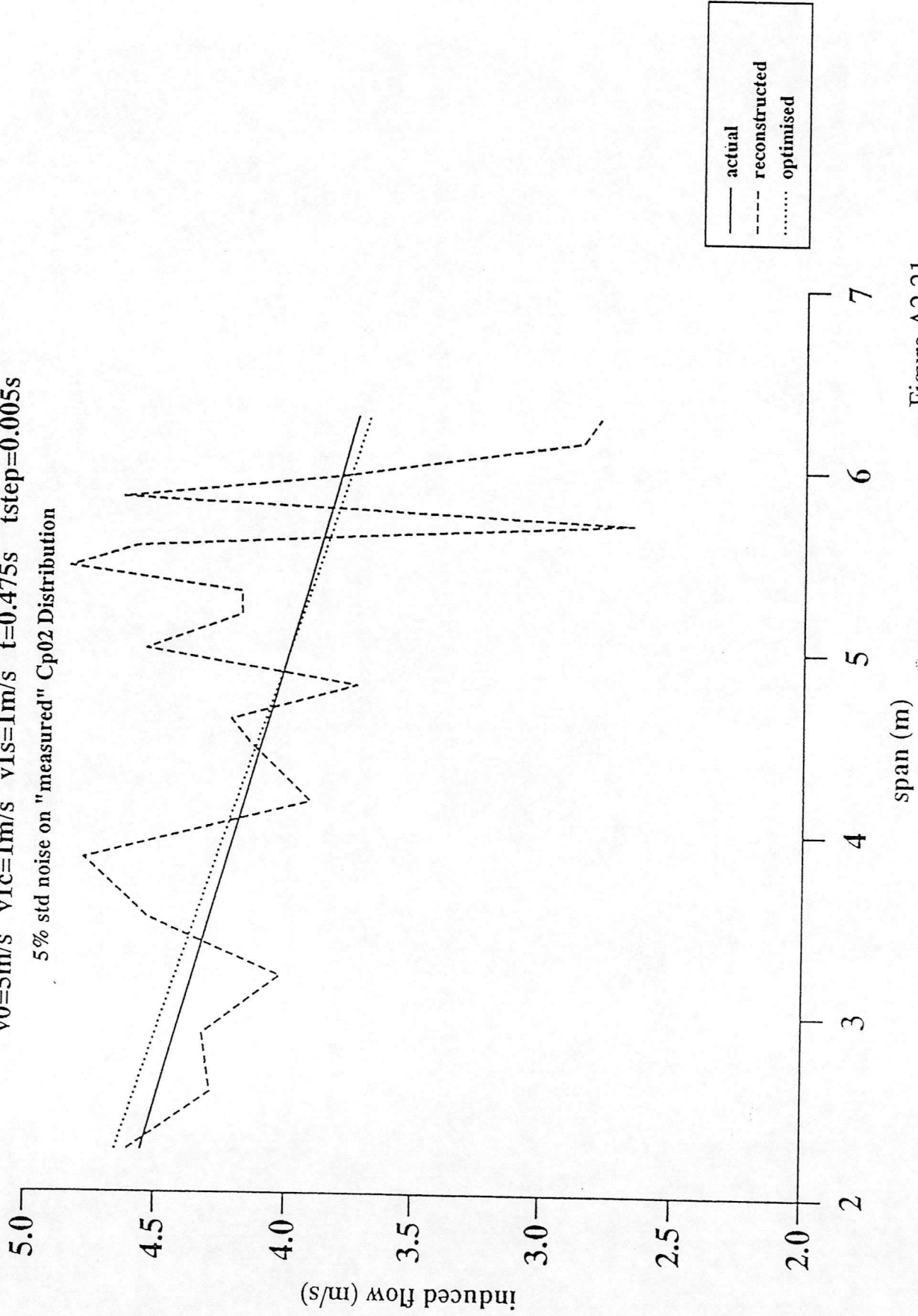
Figure A2.21

Comparison Between Actual and Reconstructed Induced Flow Velocity

4 Degrees of Collective, 0.4 Degrees of Lateral and Longitudinal Cyclic

v0=5m/s   v1c=1m/s   v1s=1m/s   t=0.475s   tstep=0.005s

5% std noise on "measured" strain pattern
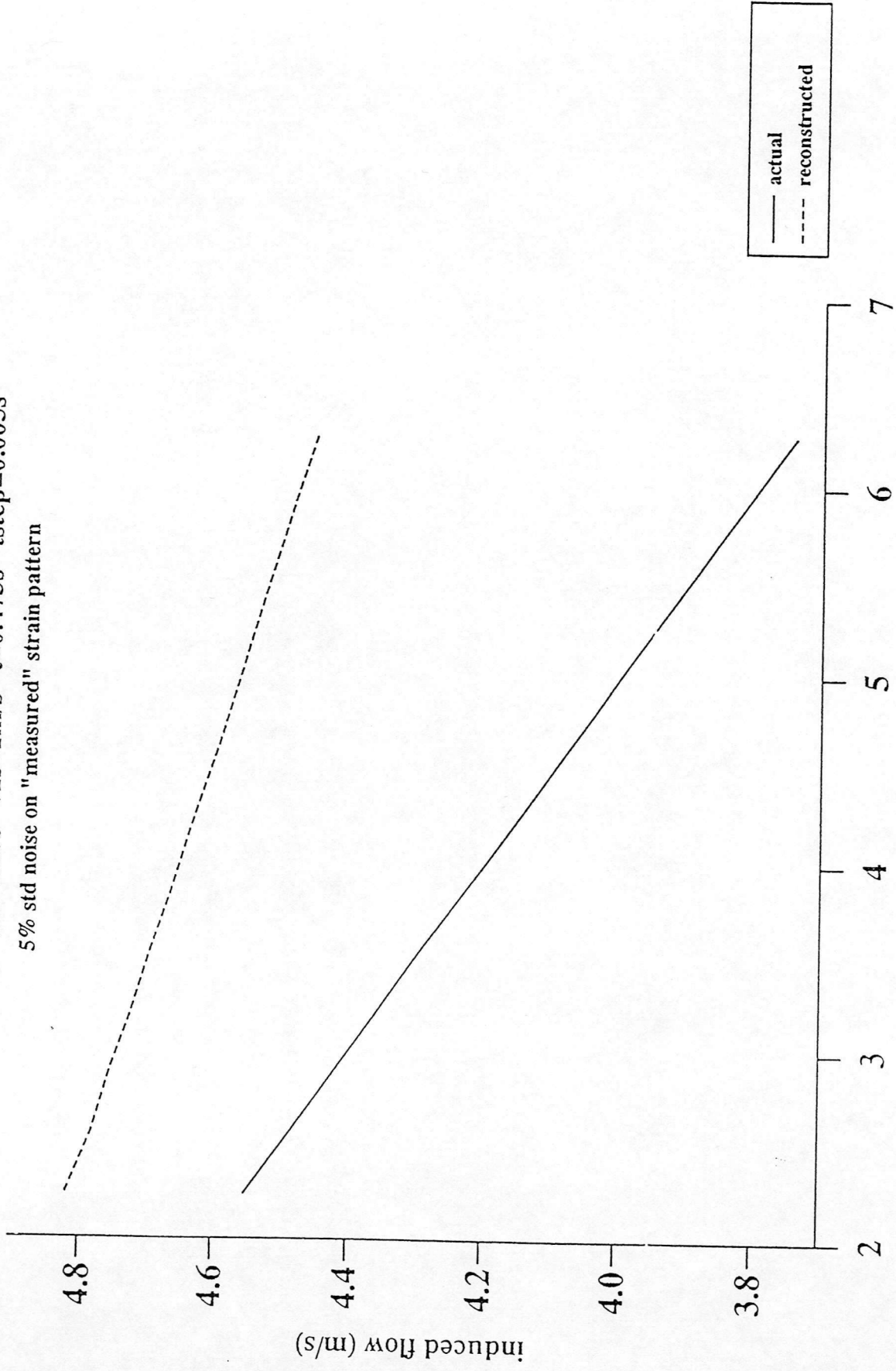
Figure A2.22

Blade Tip Structural Velocity From Spa in The Presence of Noise

First Order Lags with Varying time Constants as Filters
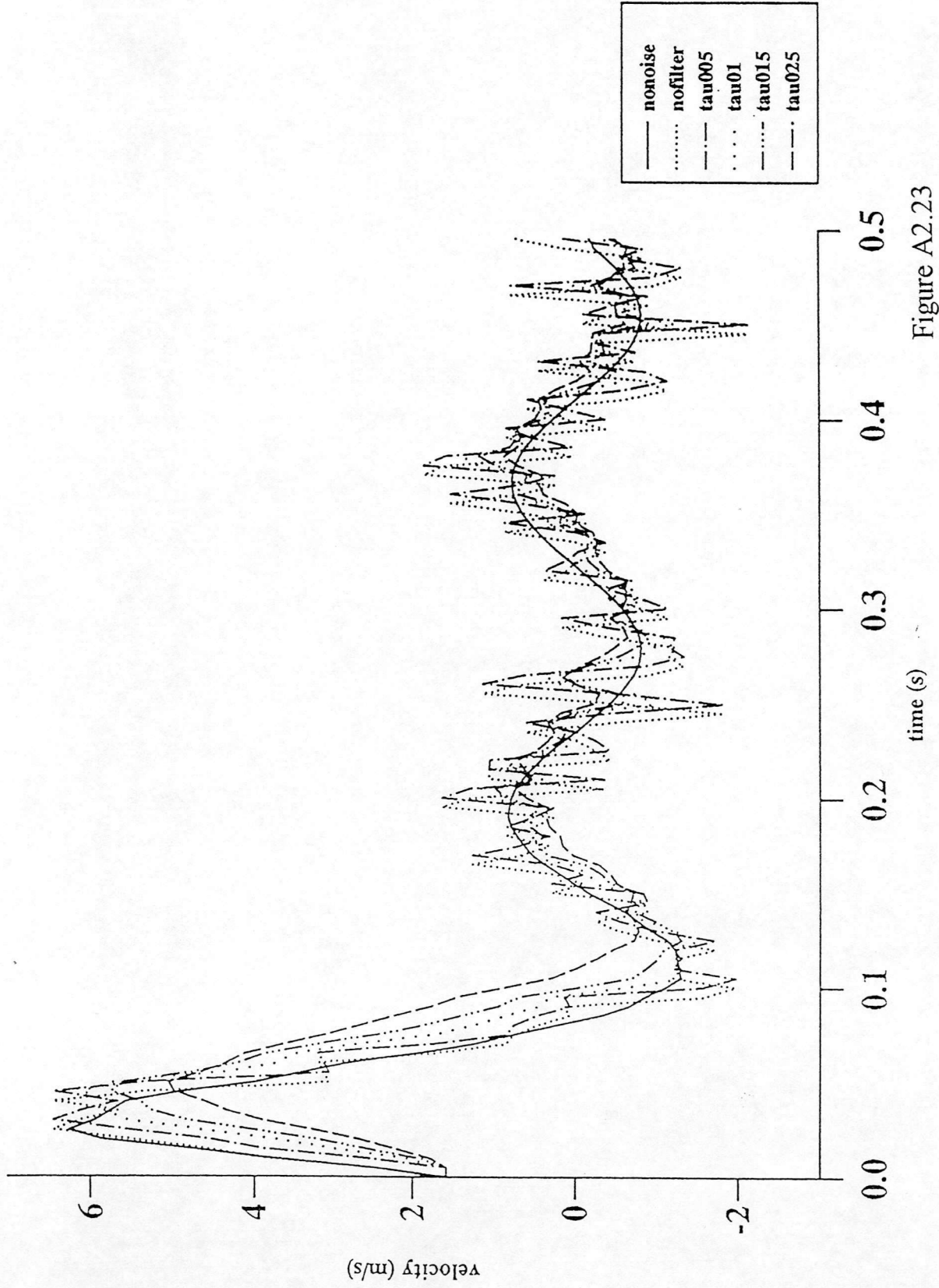
Figure A2.23

Comparison Between Actual and Reconstructed Induced Flow Velocity

4 Degrees of Collective, 0.4 Degrees of Lateral and Longitudinal Cyclic

v0=5m/s   v1c=1m/s   v1s=1m/s   t=0.475s   tstep=0.005s

5% std noise on "measured" strain pattern - filtering with tau=0.015secs
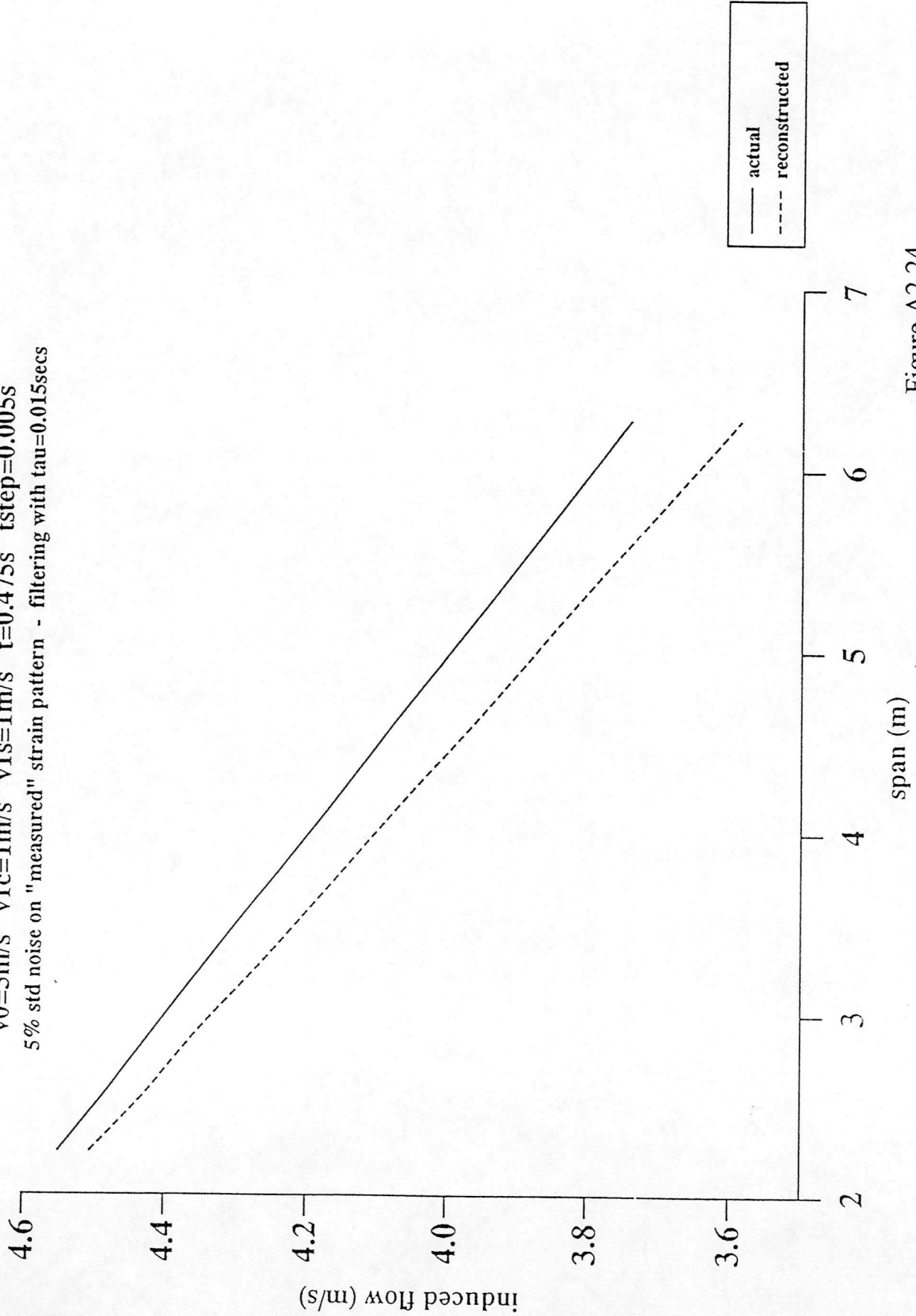
Figure A2.24

Puma Blade Displacements
Synthesised From Data Measured in the Hover
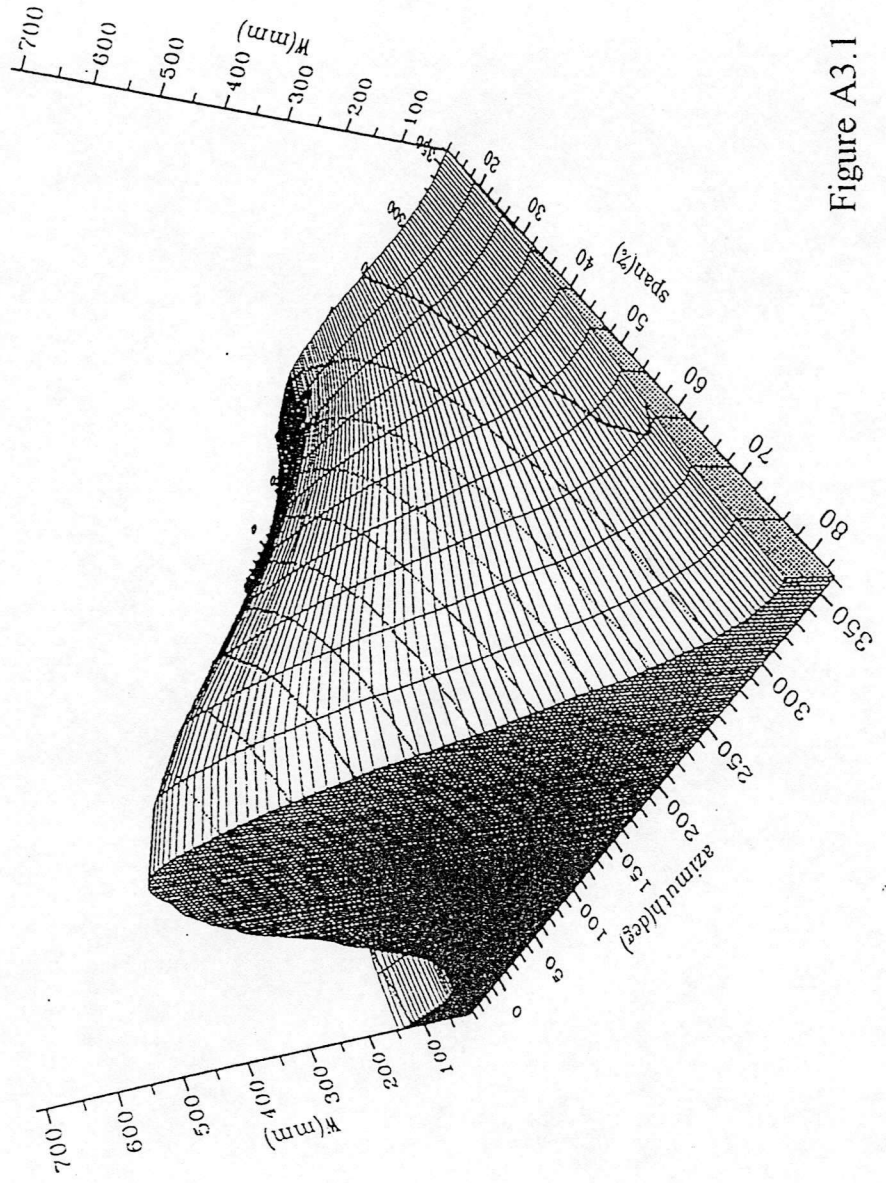
Figure A3.1

Puma Blade Pitch

Synthesised From Data Measured in the Hover
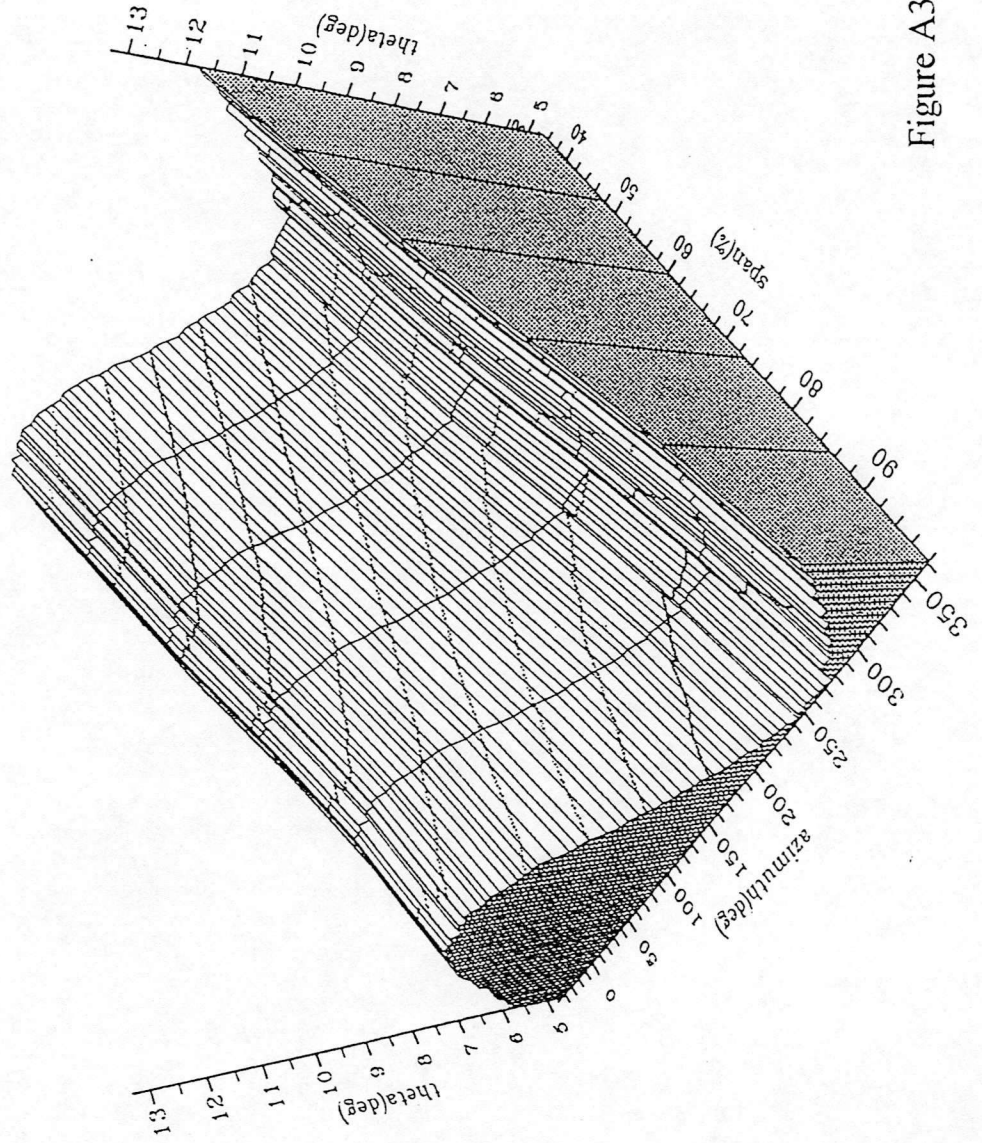
Figure A3.2

Puma Blade Structural Velocity
Synthesised From Data Measured in the Hover
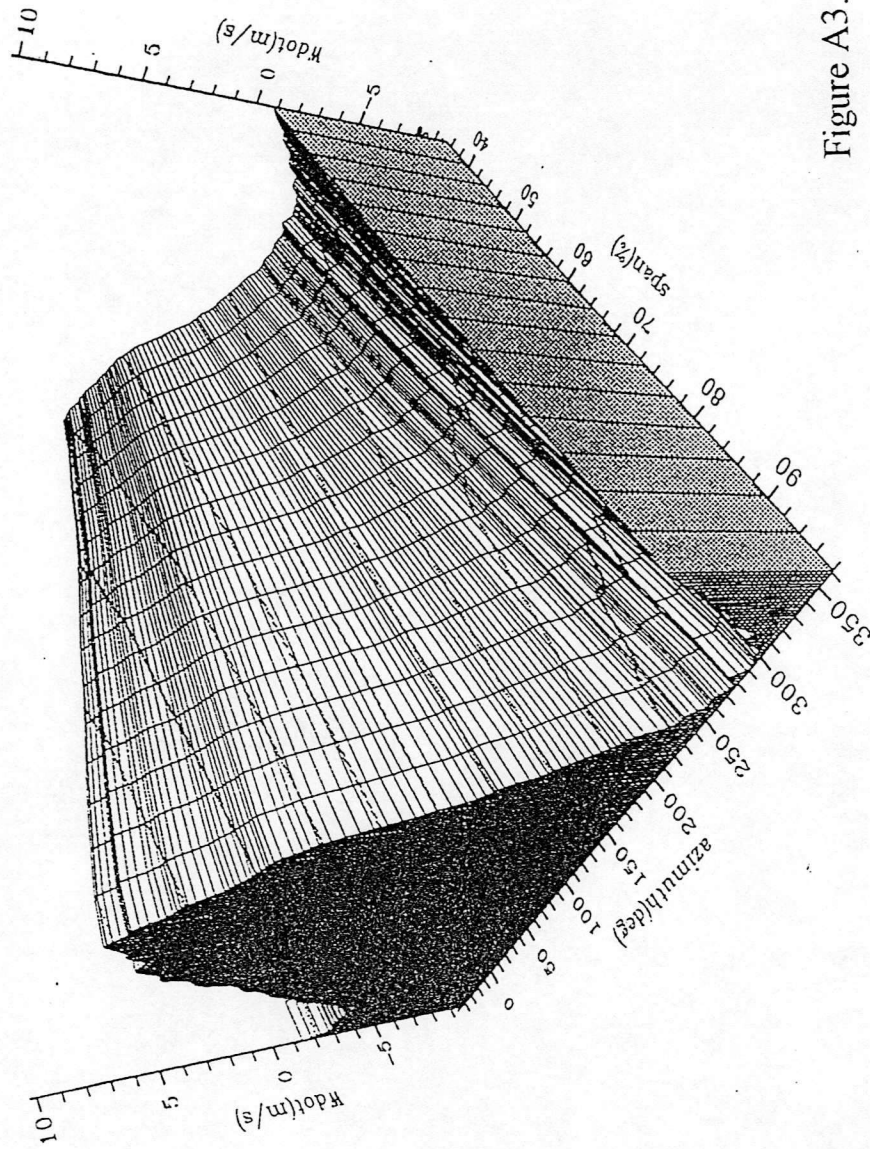
15 mS Filtering

Figure A3.3

Puma Blade Angle of Attack
Synthesised From Data Measured in the Hover
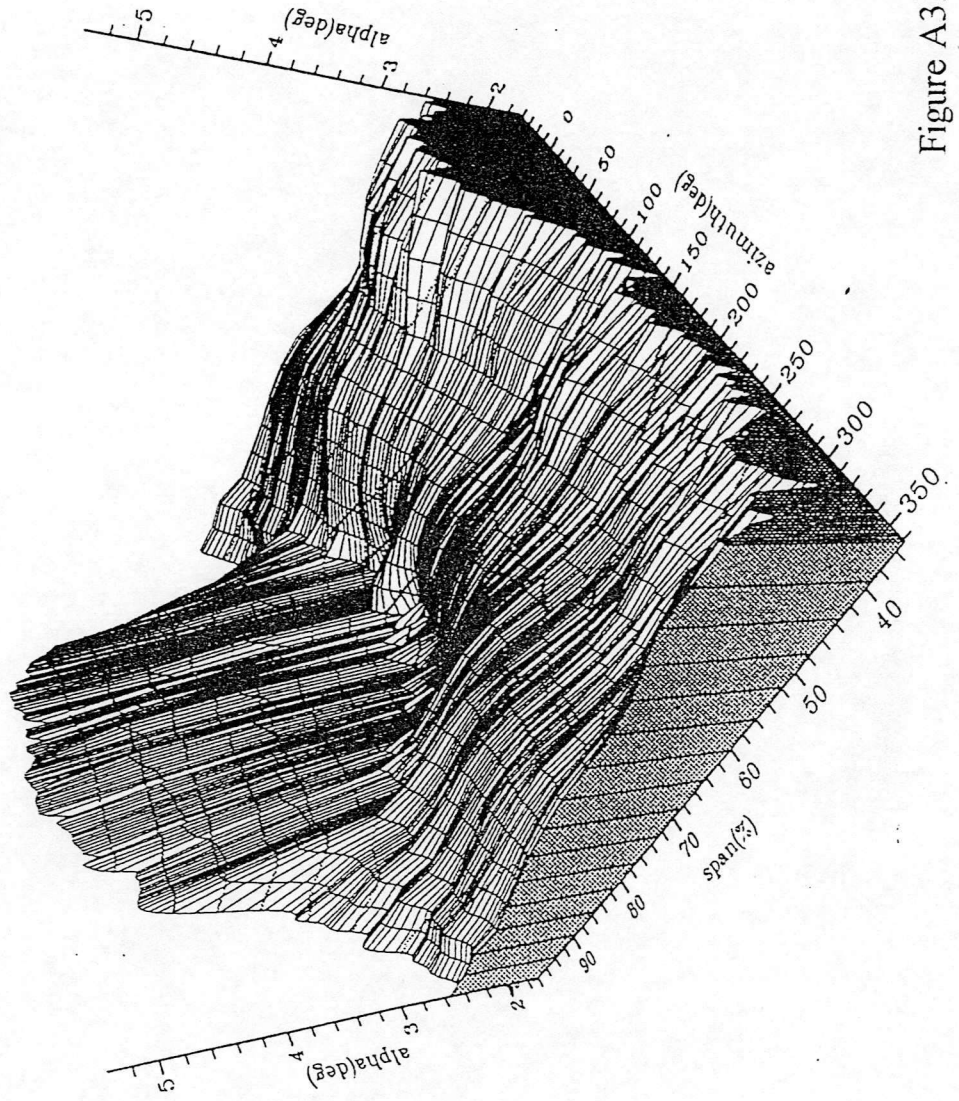
Figure A3.4

Puma Induced Flow
Synthesised from Data Measured in the Hover

15mS Filtering
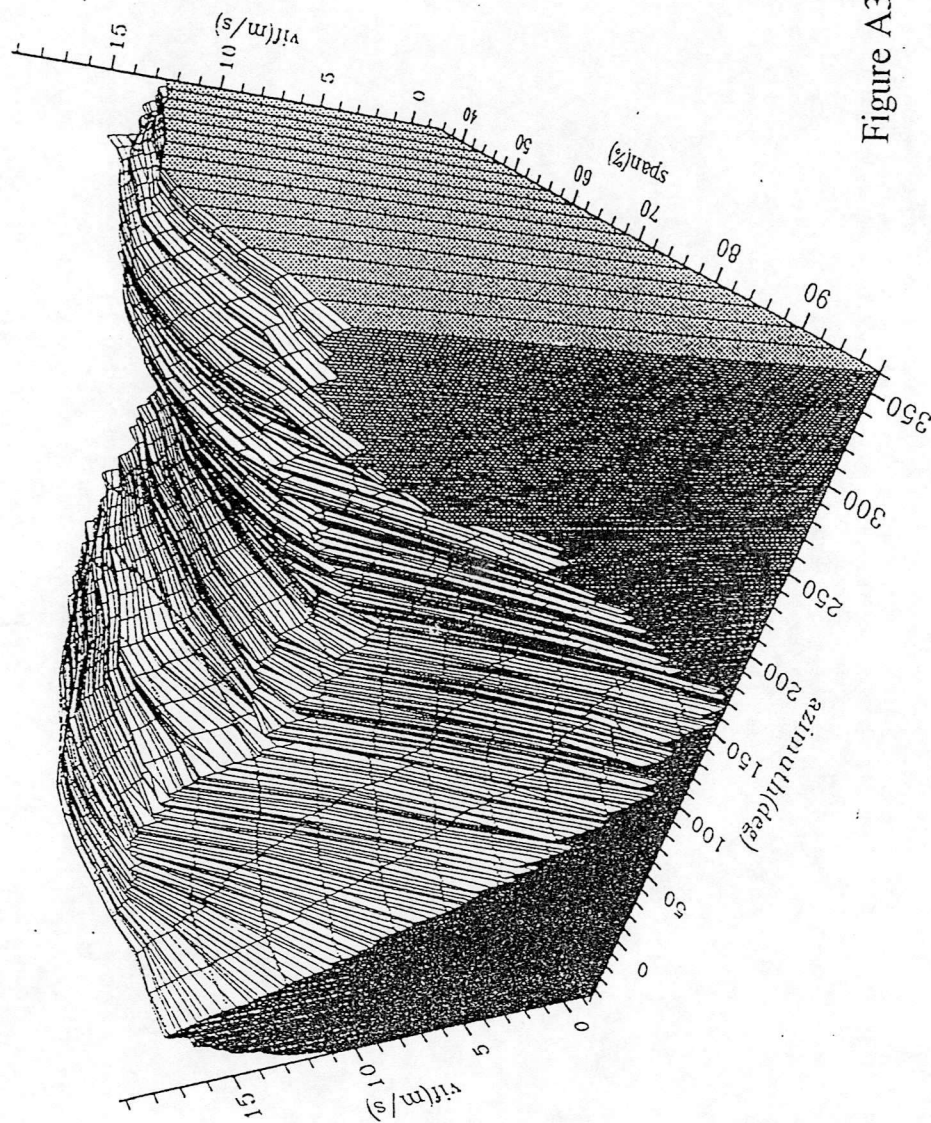
20m/s at 354deg

to

-2m/s at 165deg

Figure A3.5
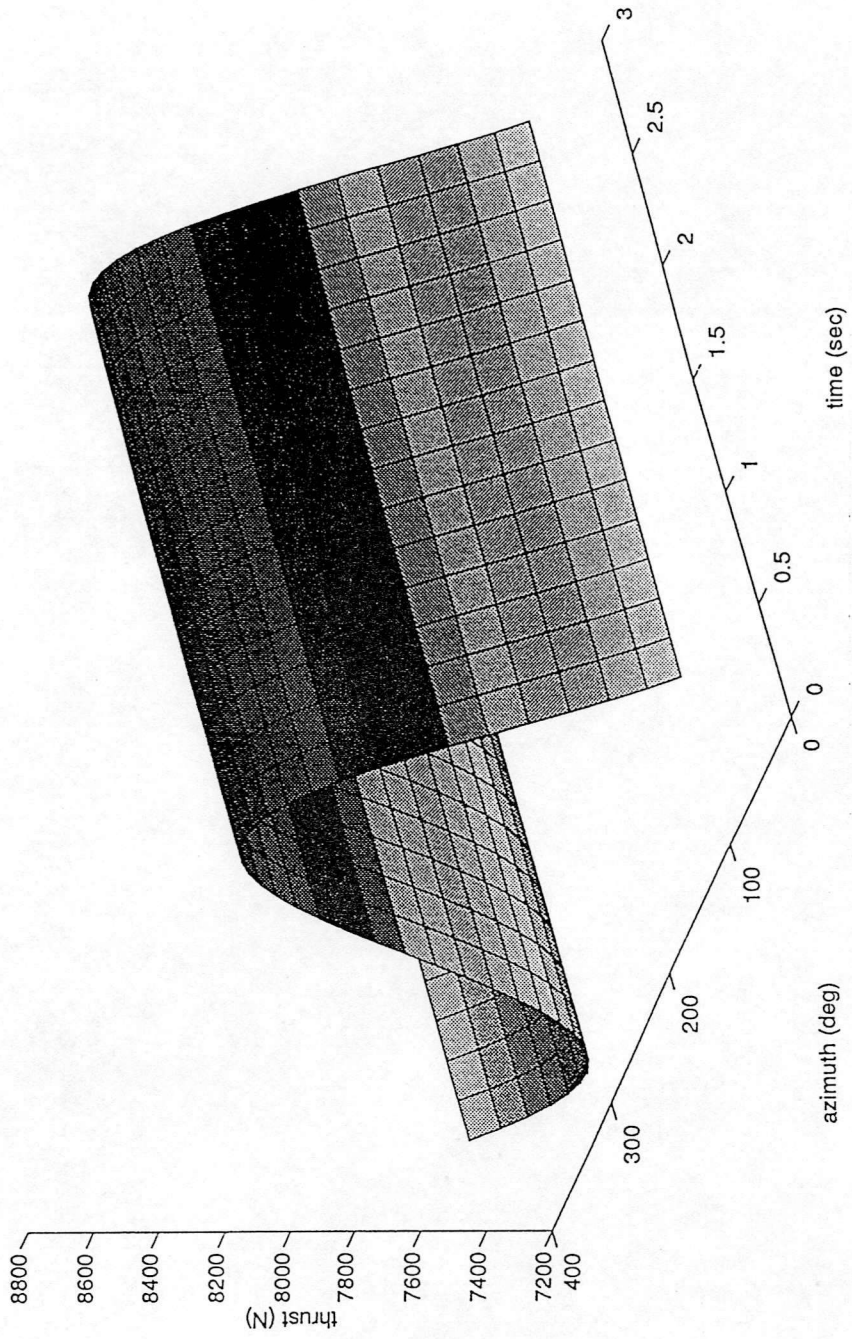
Figure A4.2 Look-Up Table for Blade Thrust - Steady Trim
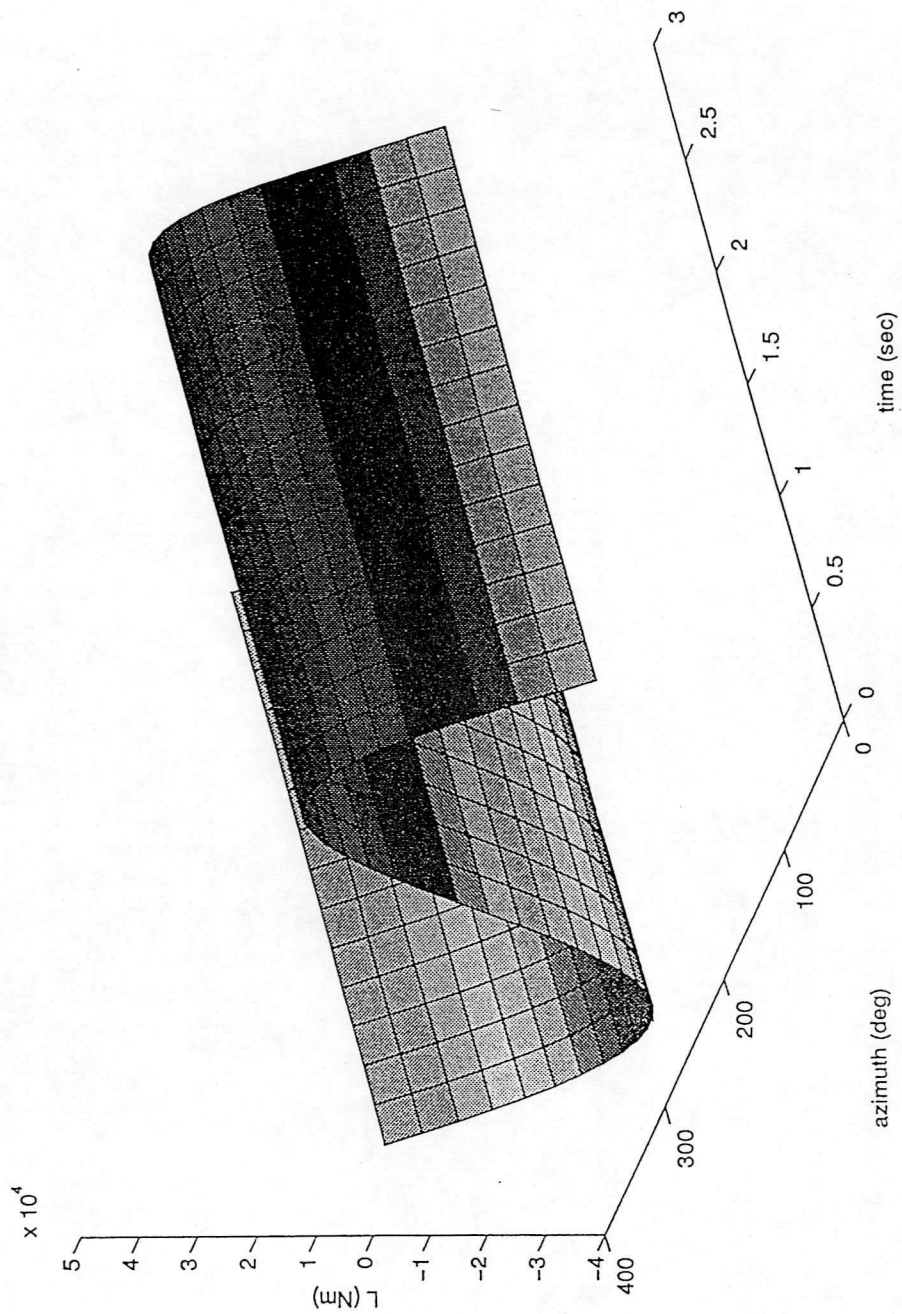
Figure A4.3 Look-Up Table for Blade Aerodynamic Rolling Moment - Steady Trim
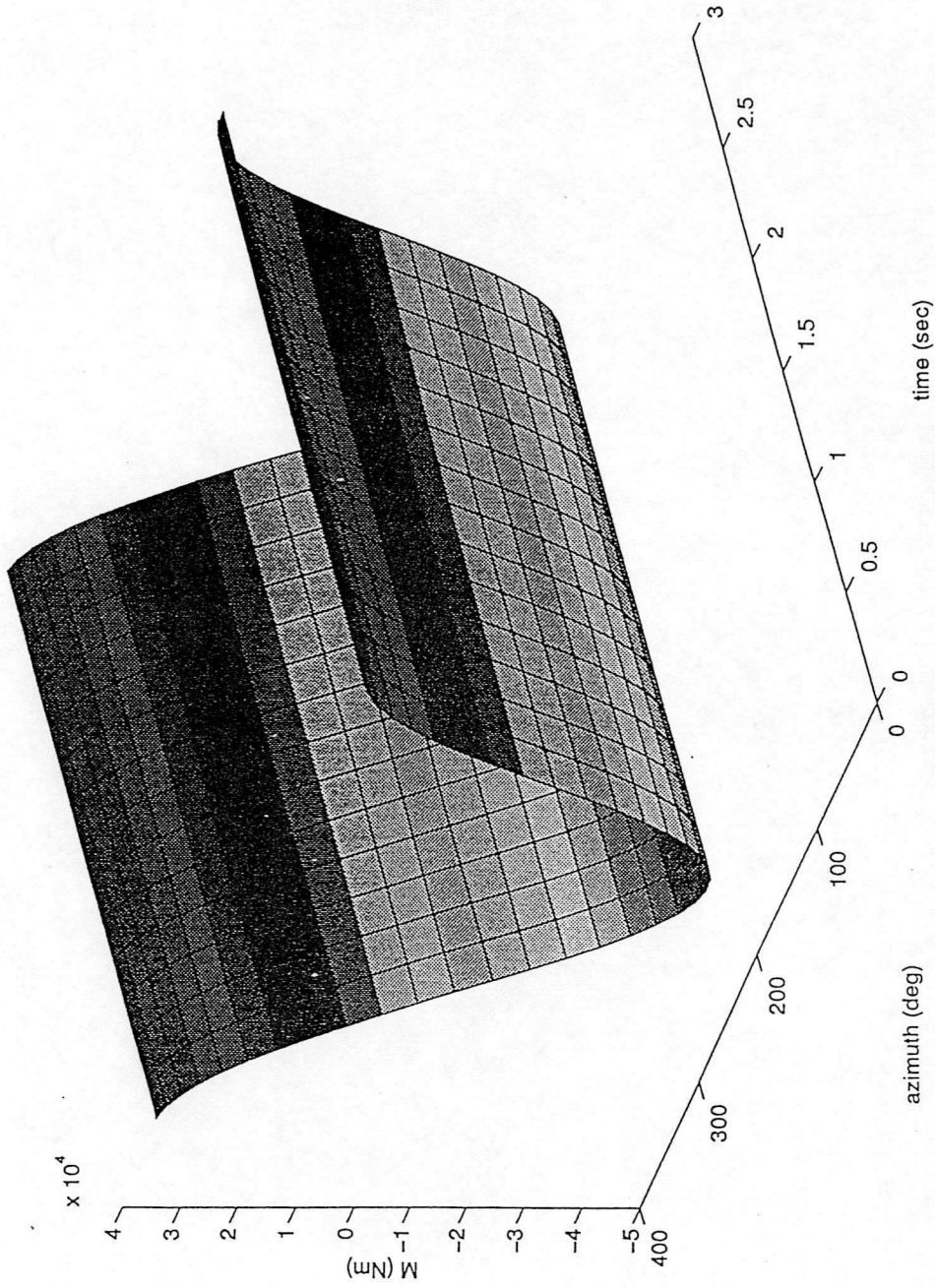
Figure A4.4 Look-Up Table for Blade Aerodynamic Pitching Moment - Steady Trim
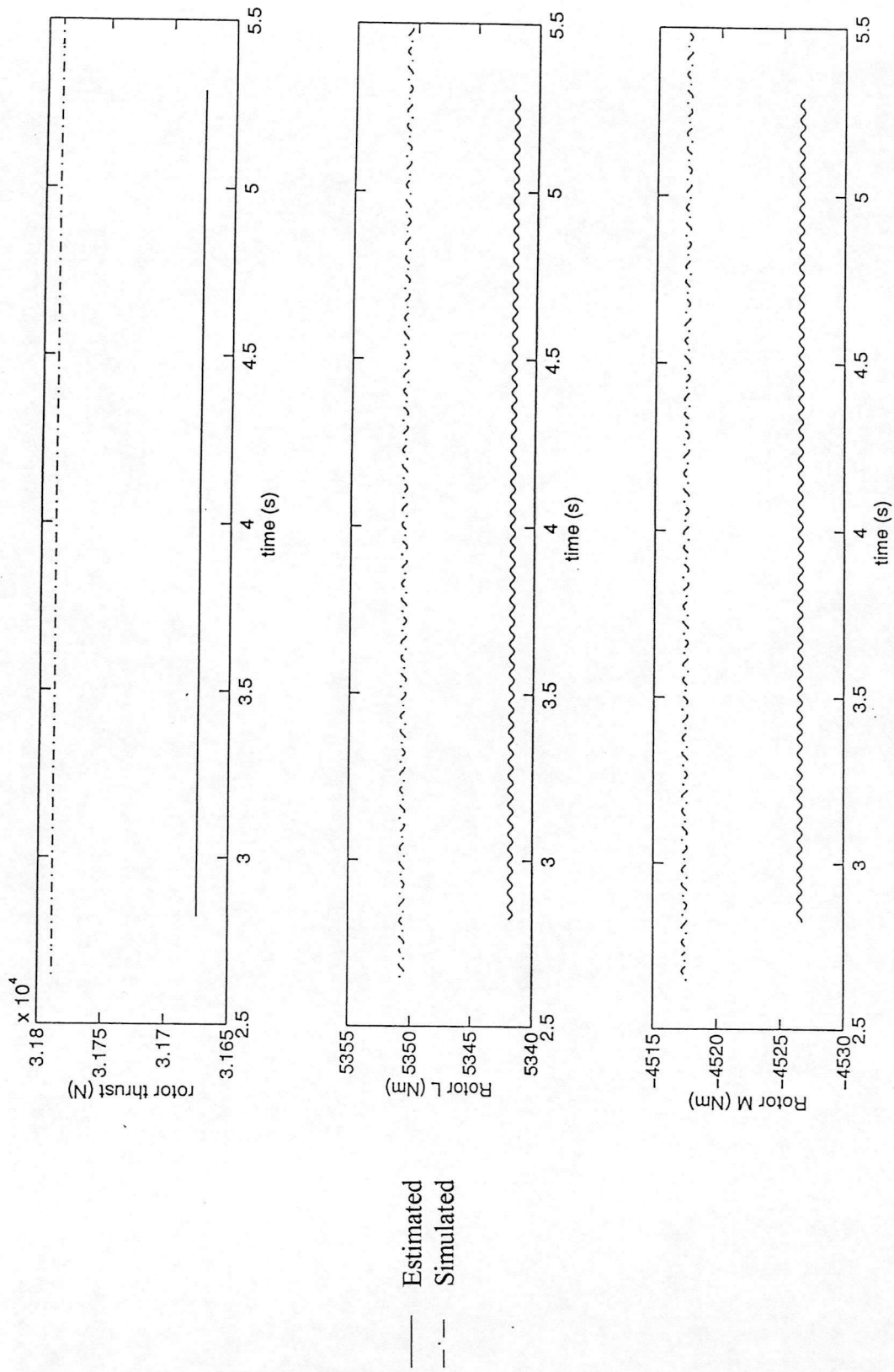
Figure A4.5 Comparison Between Simulated and Estimated Rotor Thrust/Moments - Steady Trim
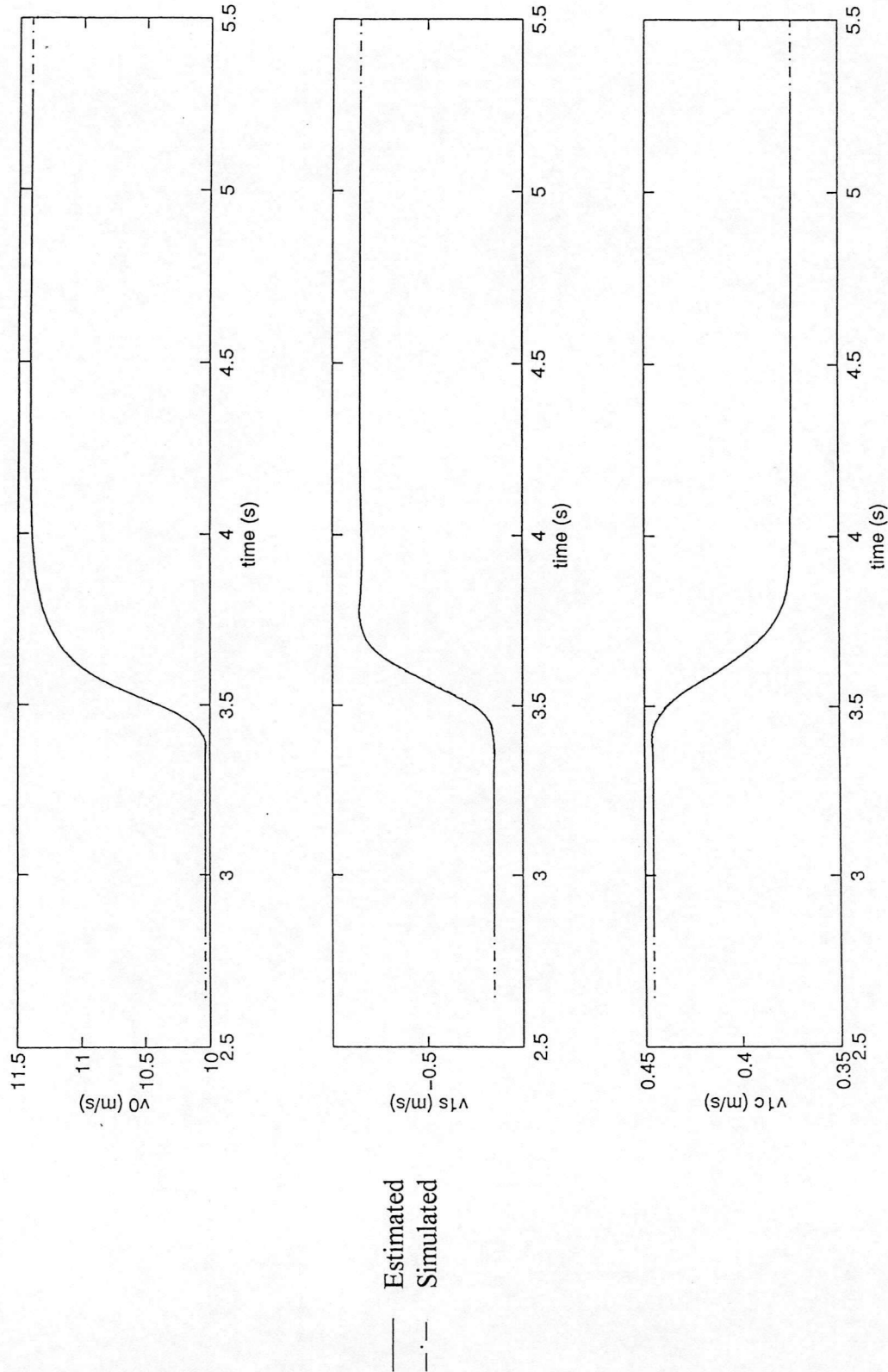
Figure A4.6 Comparison Between Simulated and Estimated Induced Flow States - Step to Collective
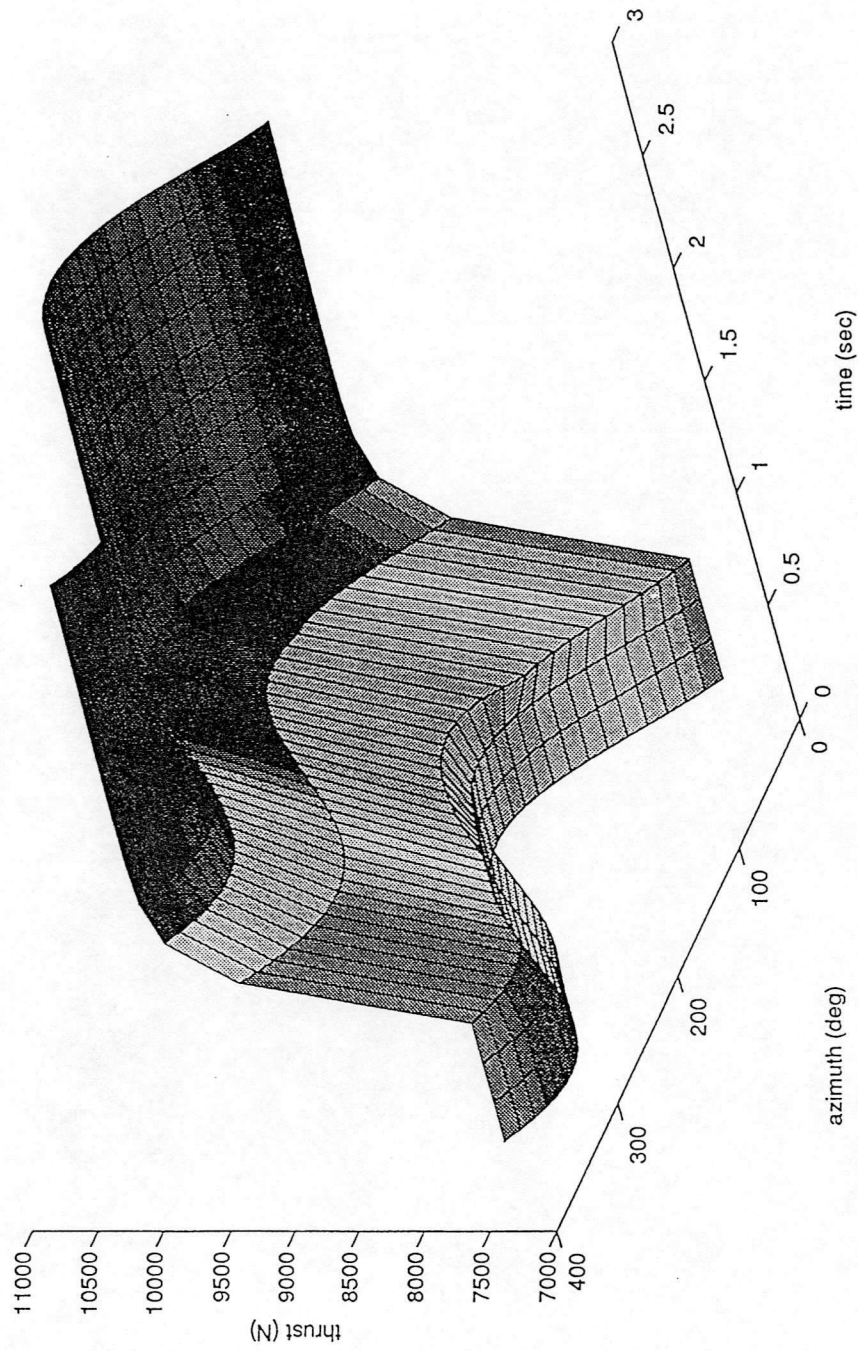
Figure A4.7 Look-Up Table for Blade Thrust - Step to Collective
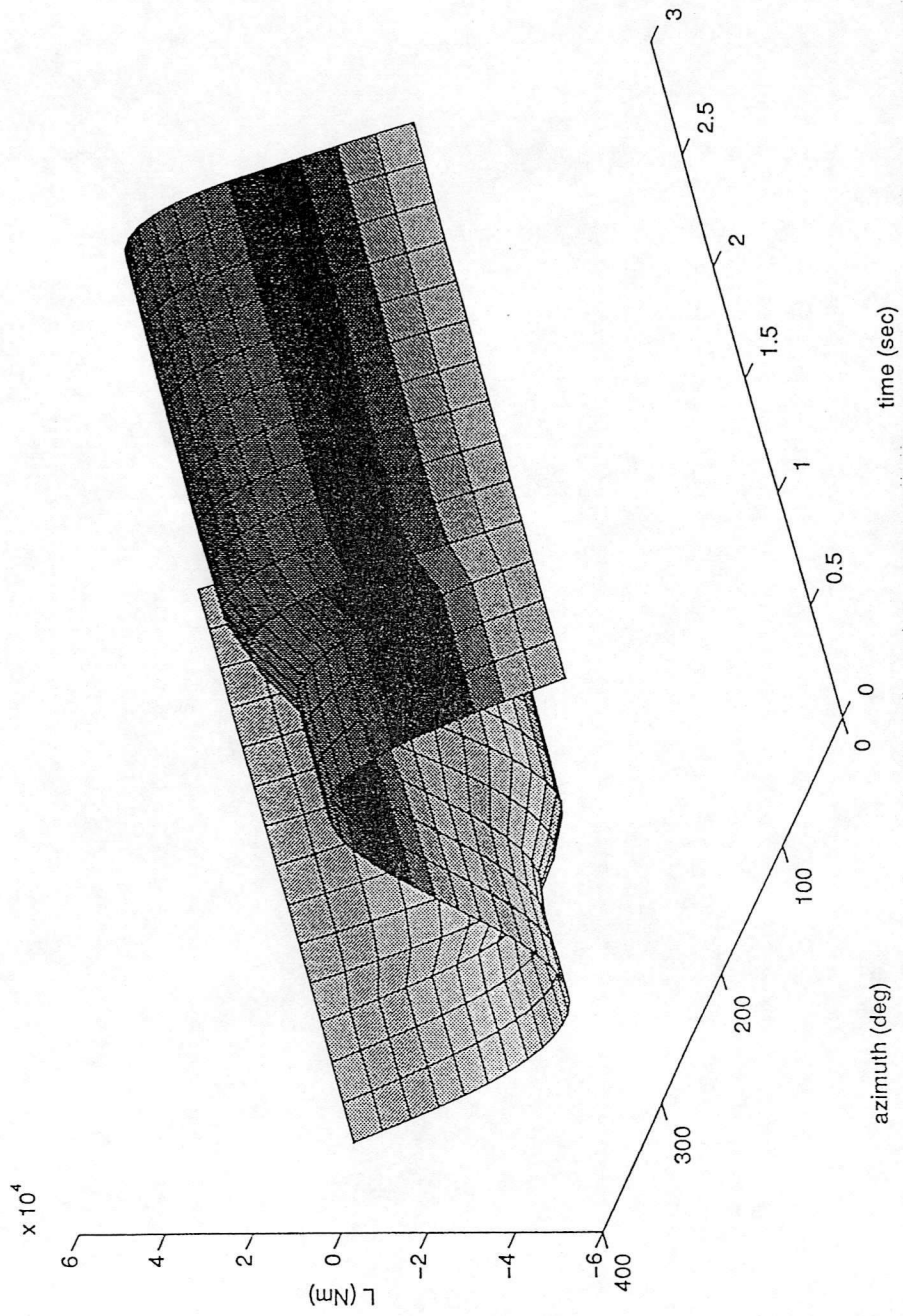
Figure A4.8 Look-Up Table for Blade Aerodynamic Rolling Moment – Step to Collective
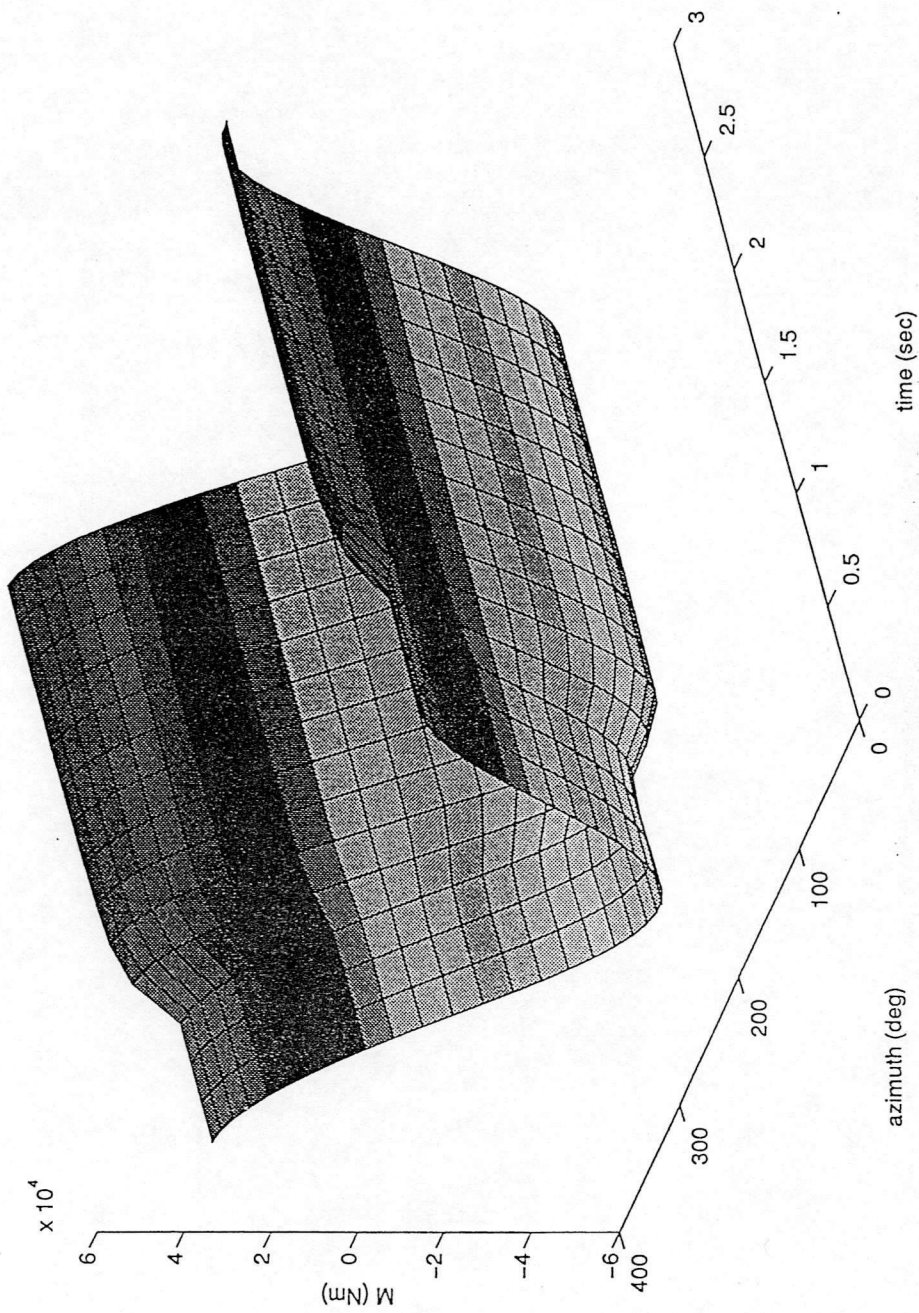
Figure A4.9 Look-Up Table for Blade Aerodynamic Pitching Moment - Step to Collective
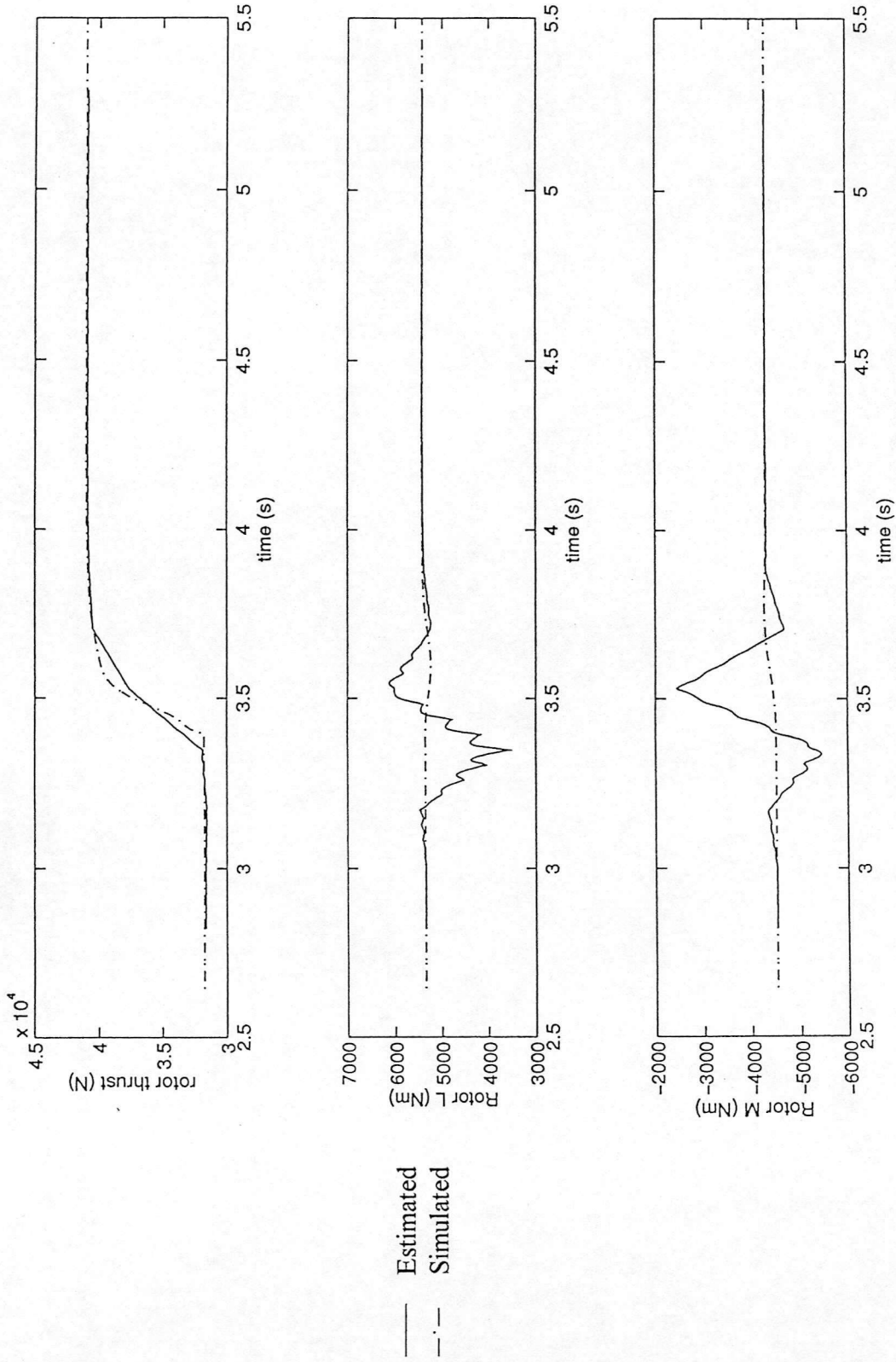
Figure A4.10   Comparison Between Simulated and Estimated Rotor Thrust/Moments - Step to Collective
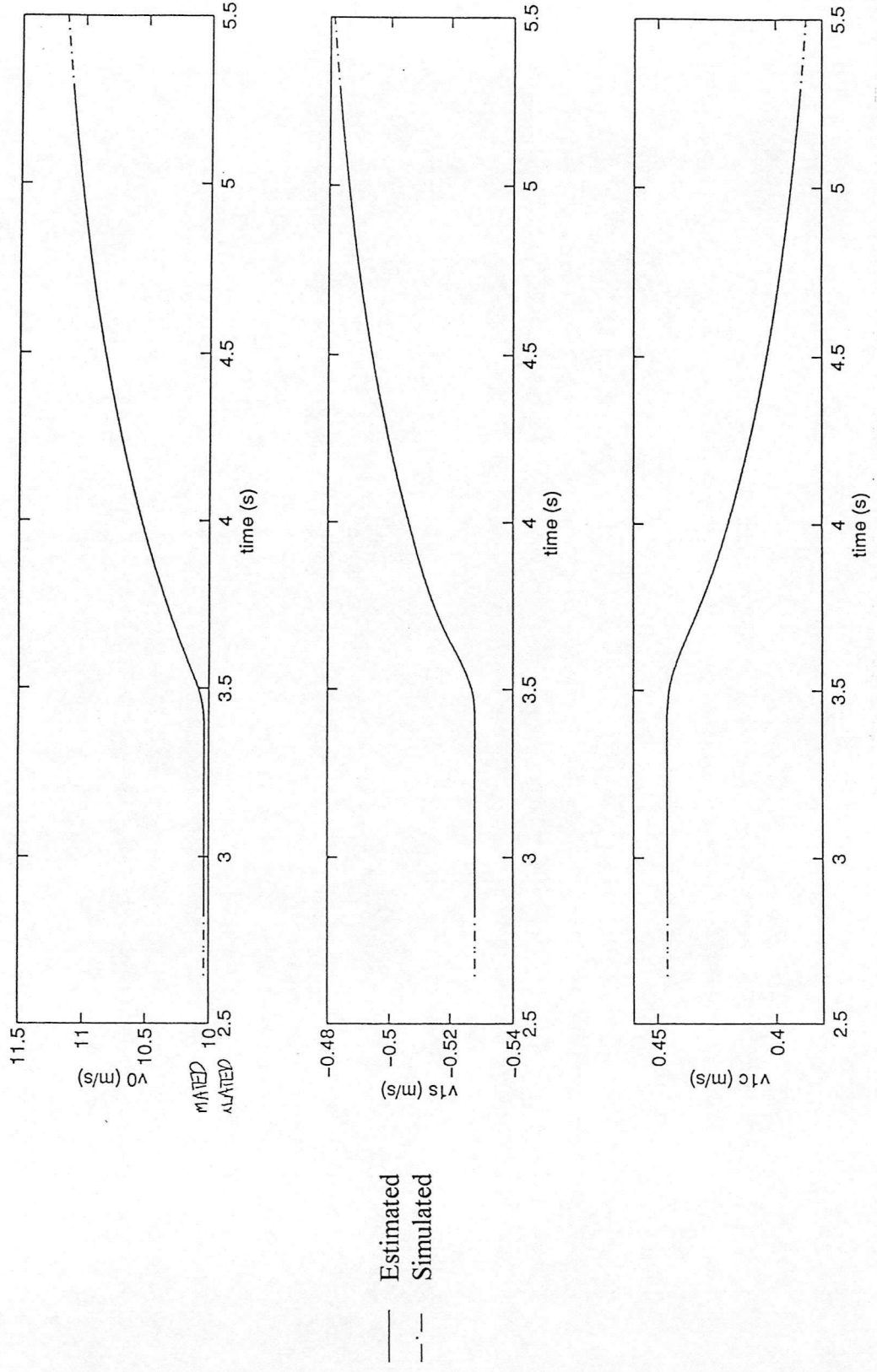
Figure A4.11   Comparison Between Simulated and Estimated Induced Flow States - Ramp to Collective

azimuth (deg)

time (sec)
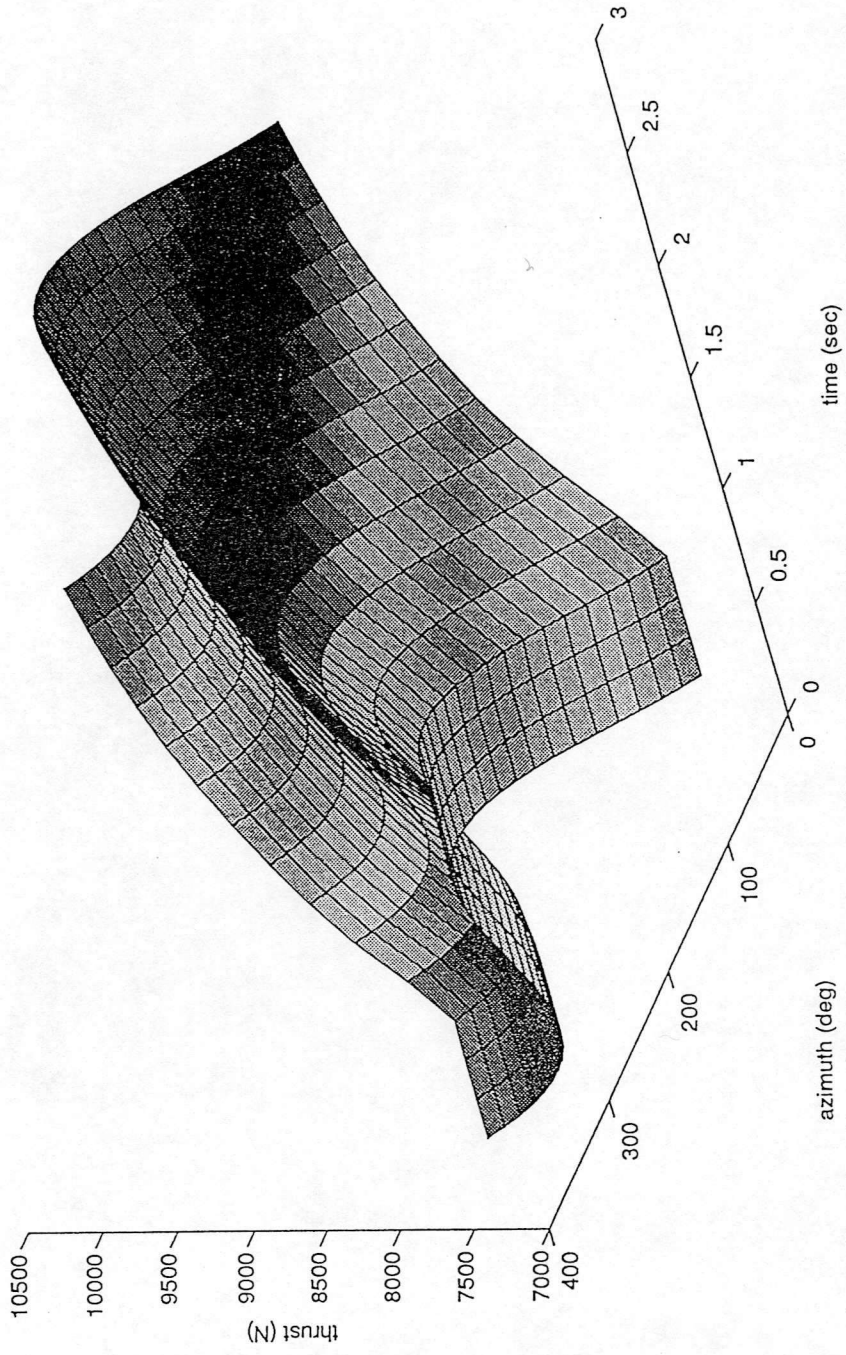
thrust (N)

Figure A4.12   Look-Up Table for Blade Thrust - Ramp to Collective
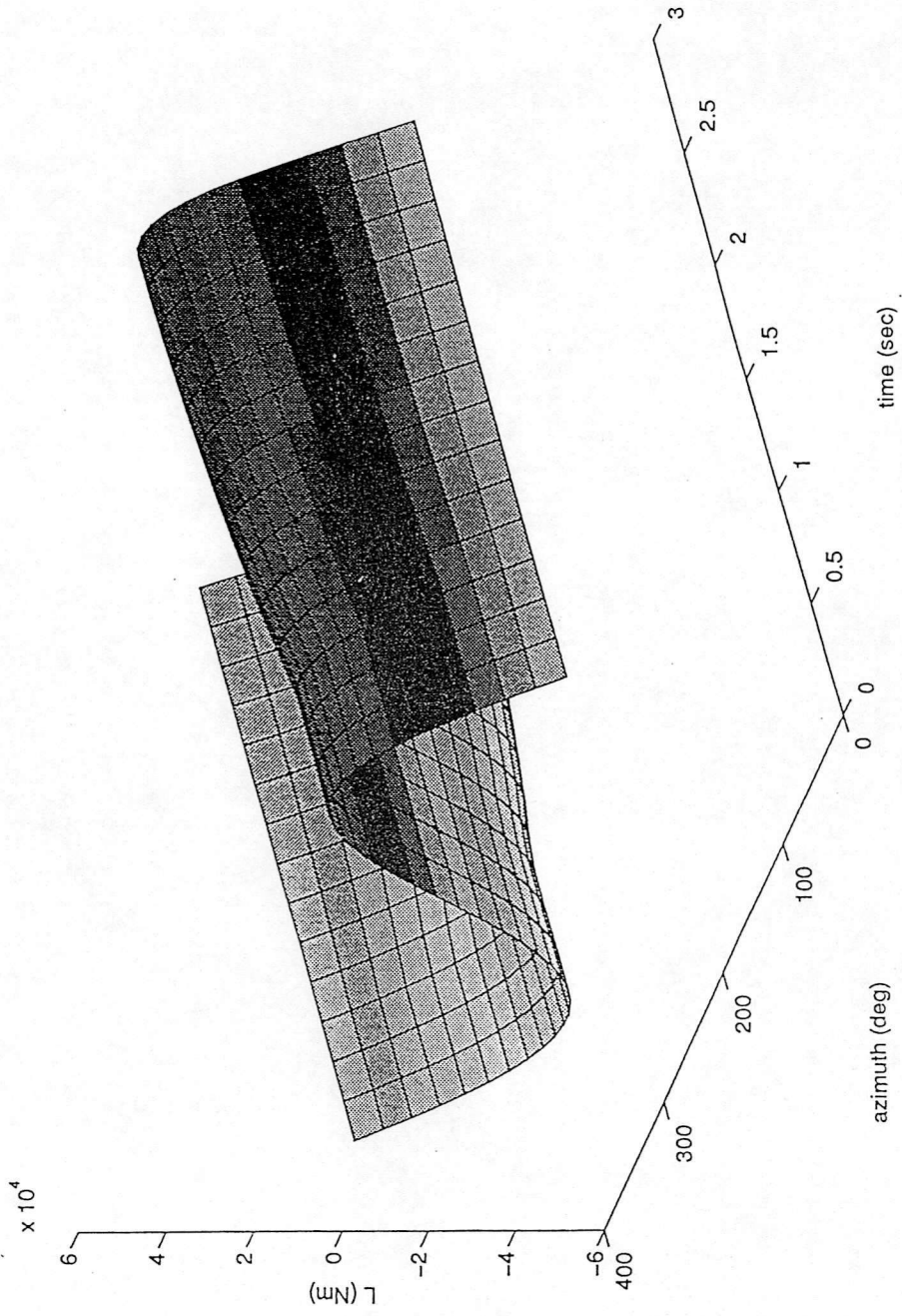
Figure A4.13   Look-Up Table for Blade Aerodynamic Rolling Moment - Ramp to Collective
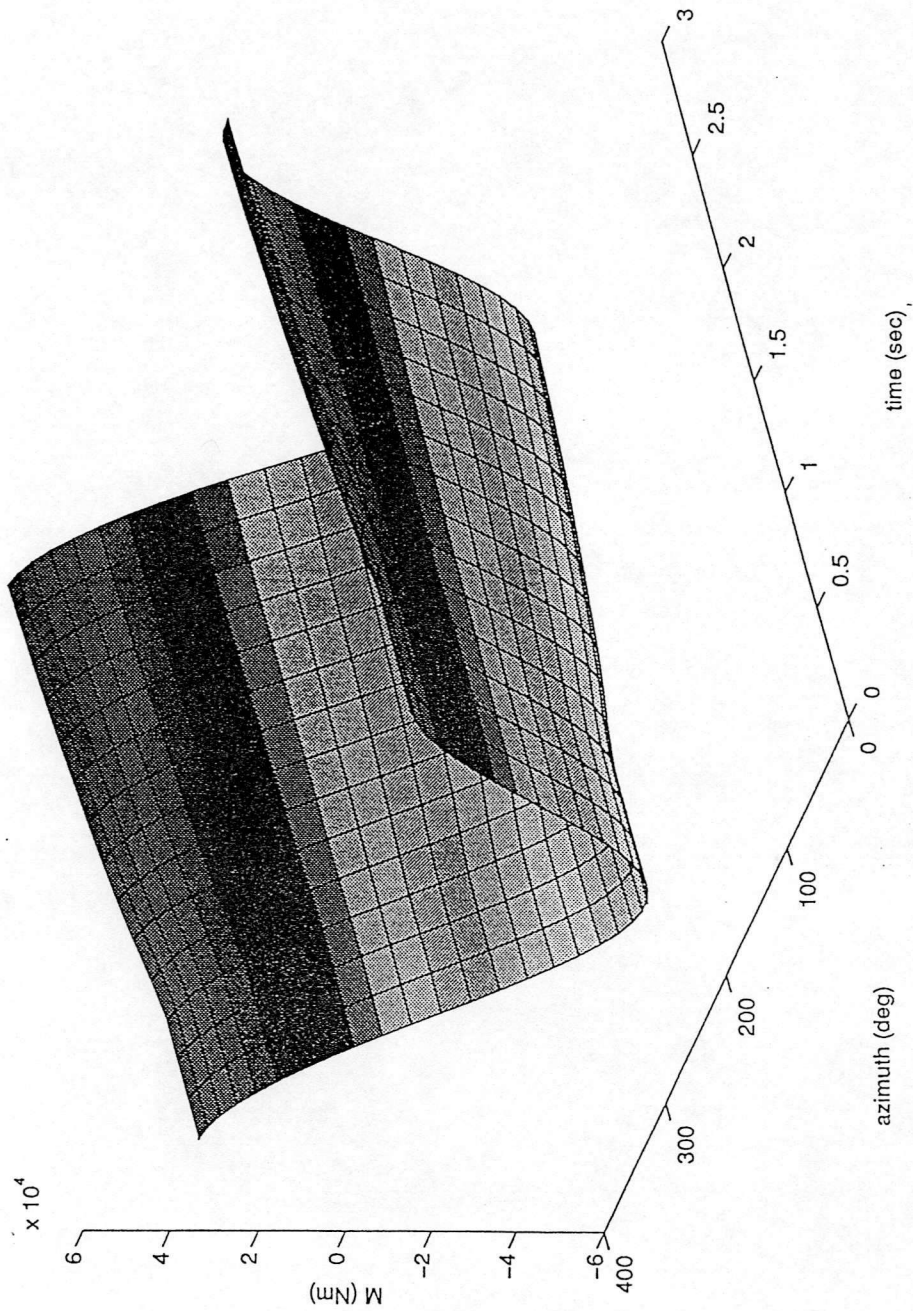
Figure A4.14   Look-Up Table for Blade Aerodynamic Pitching Moment - Ramp to Collective
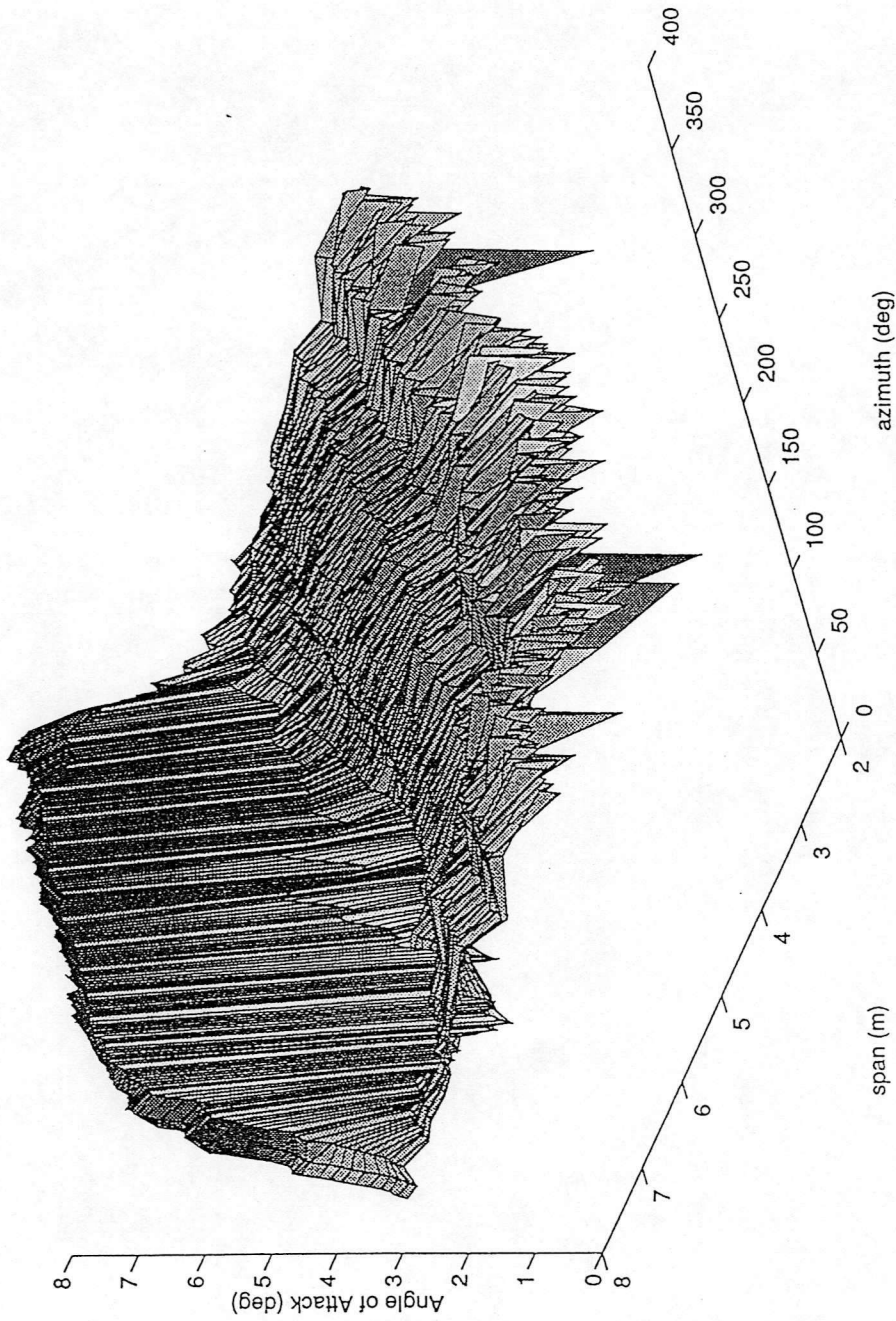
Figure A4.18   Estimated Angle of Attack Distribution for Puma in Hover
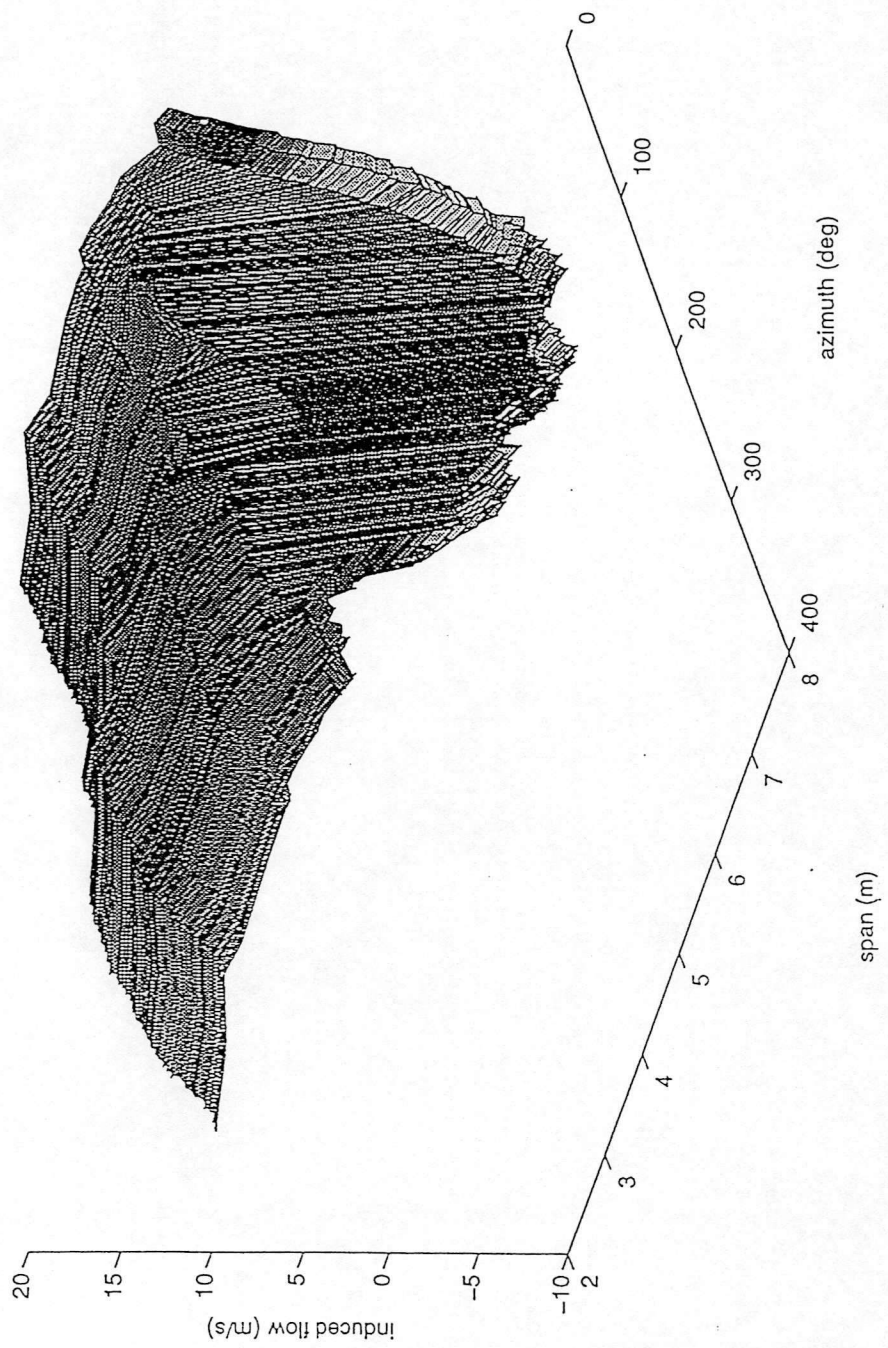
Figure A4.19   Estimated Induced Flow Distribution for Puma in Hover
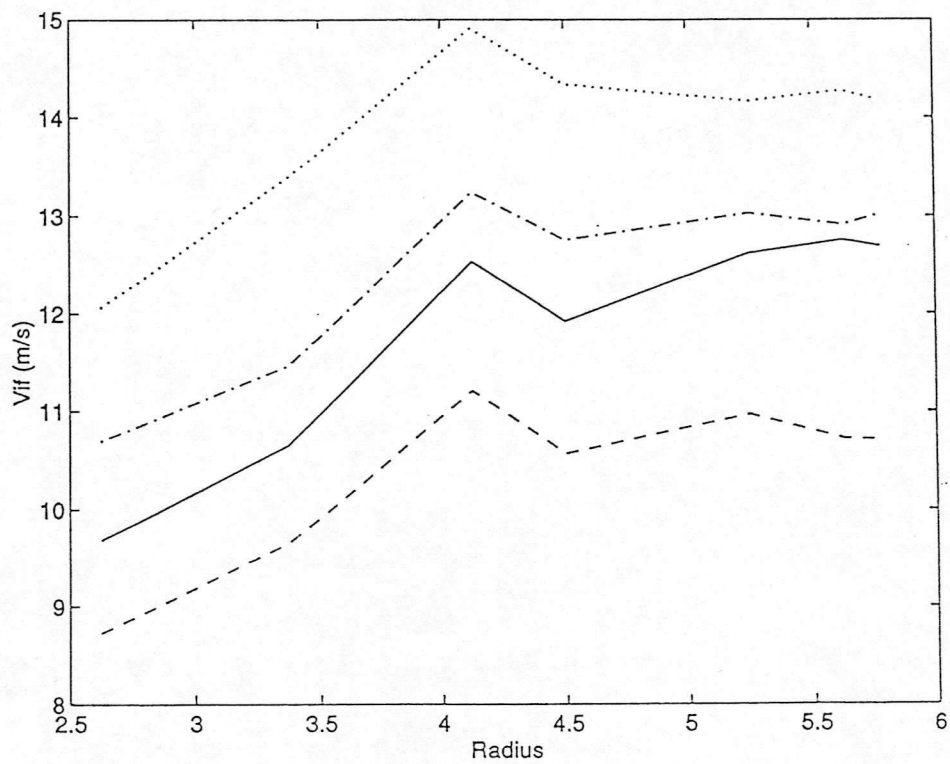
Figure A4.20 Spanwise Variation in Estimated Induced Flow Distribution
at 4 Azimuthal Stations
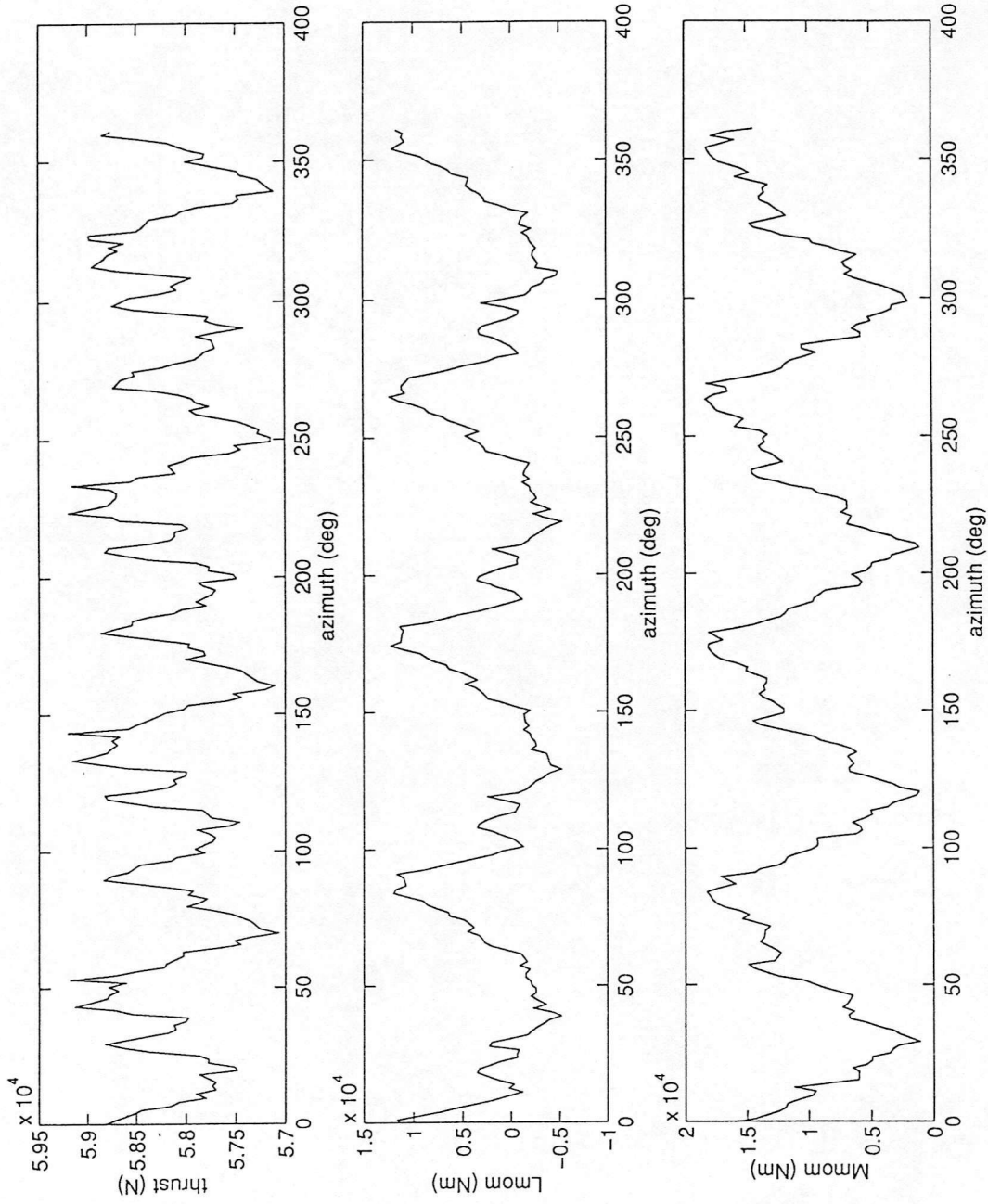
Figure A4.21   Estimated Rotor Thrust/Moments for Puma in Hover

integration of euler angles using rates as inputs

theta, phi, psi
to workspace

error to
workspace

error

phiout

thetaout

psiout

phim

measured bank angle

thetam

measured pitch angle

psim

measured track angle

Demux

Demux

eulsfn

integrator

inputs to
workspace

Mux

Mux

qinput

rinput

f(u)

Fcn

Mux

Mux1

imp

gain

bp

bias

prate

roll rate

timer

att_clock

time to workspace

E_Clock

Figure A5.1 SIMULINK Diagram for EULSIM

integration of velocities using measured accelerations, converged rates and attitudes as inputs
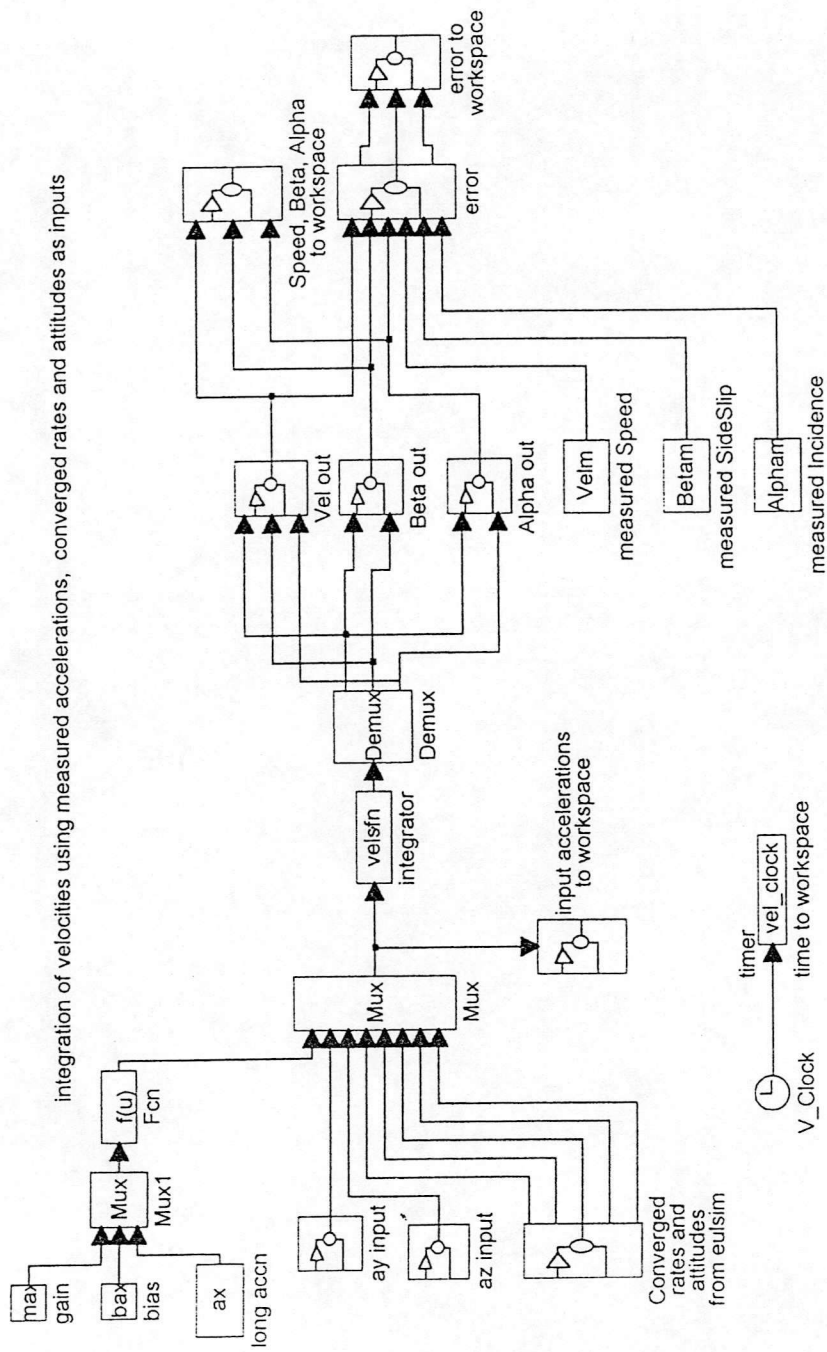
Figure A5.2 SIMULINK Diagram for VELSIM
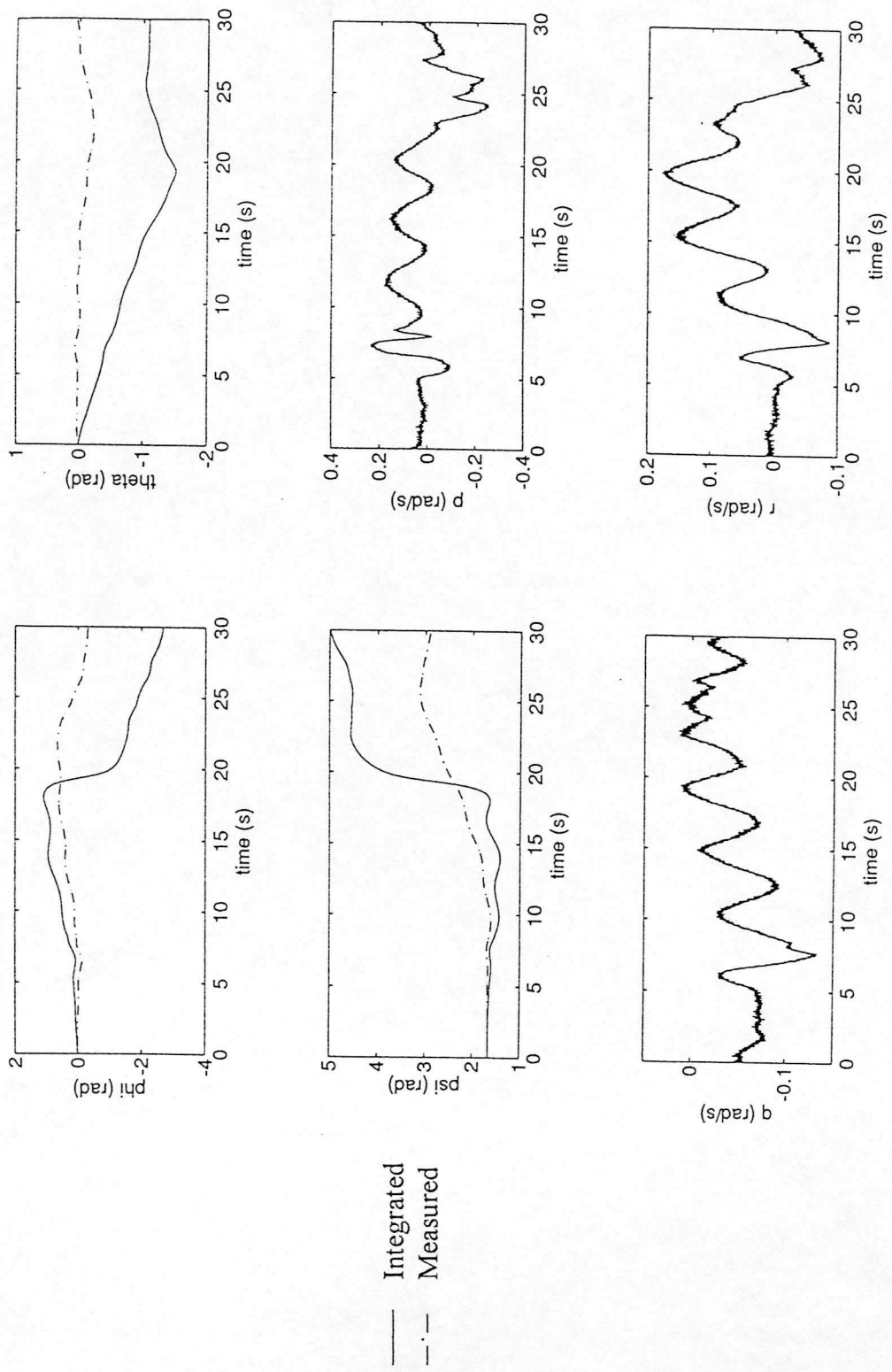
Figure A5.3 Event 8 - Correlation Before Attitude Pass is Performed
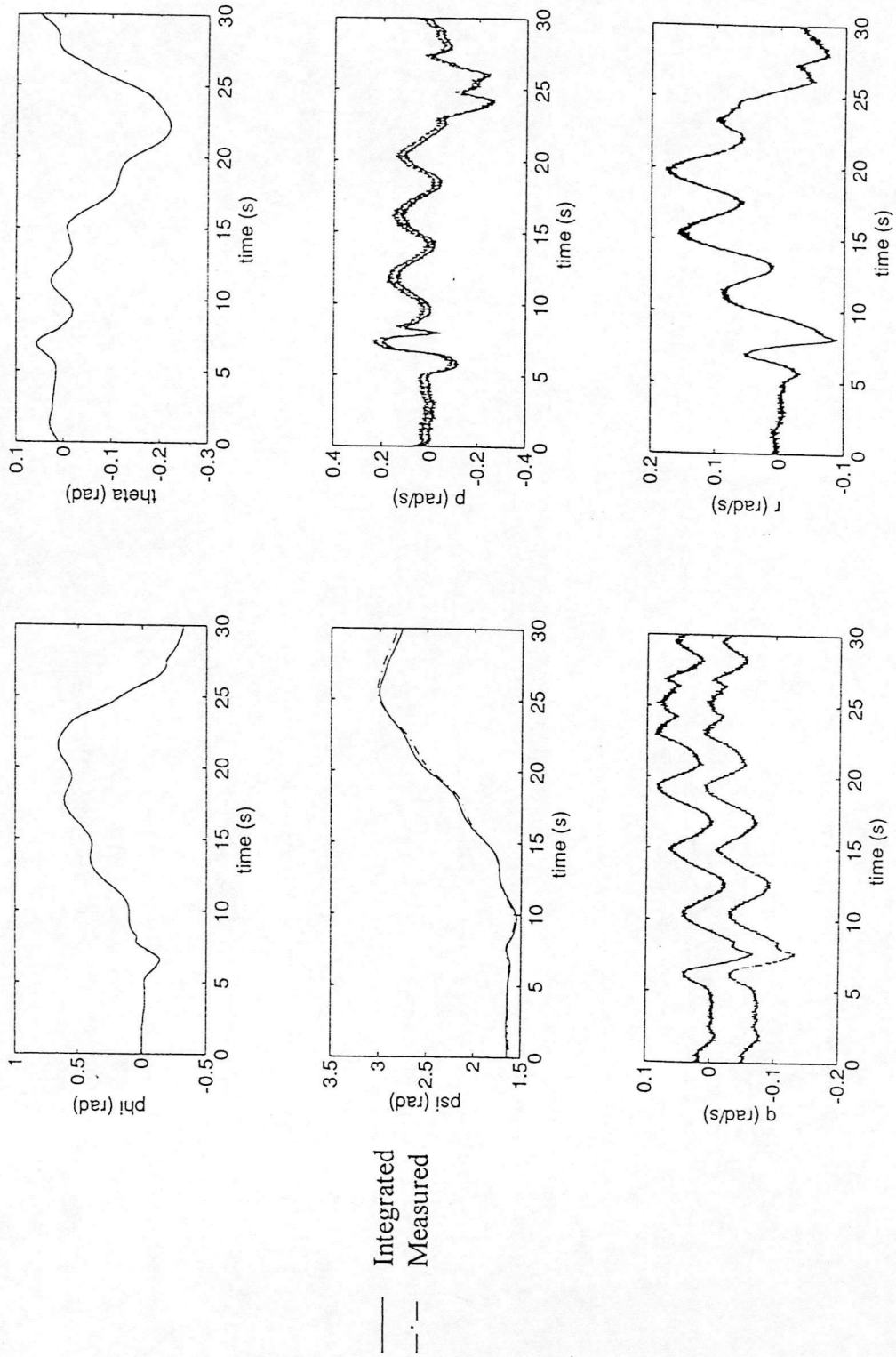
Figure A5.4 Correlation After Attitude Pass Has Been Performed
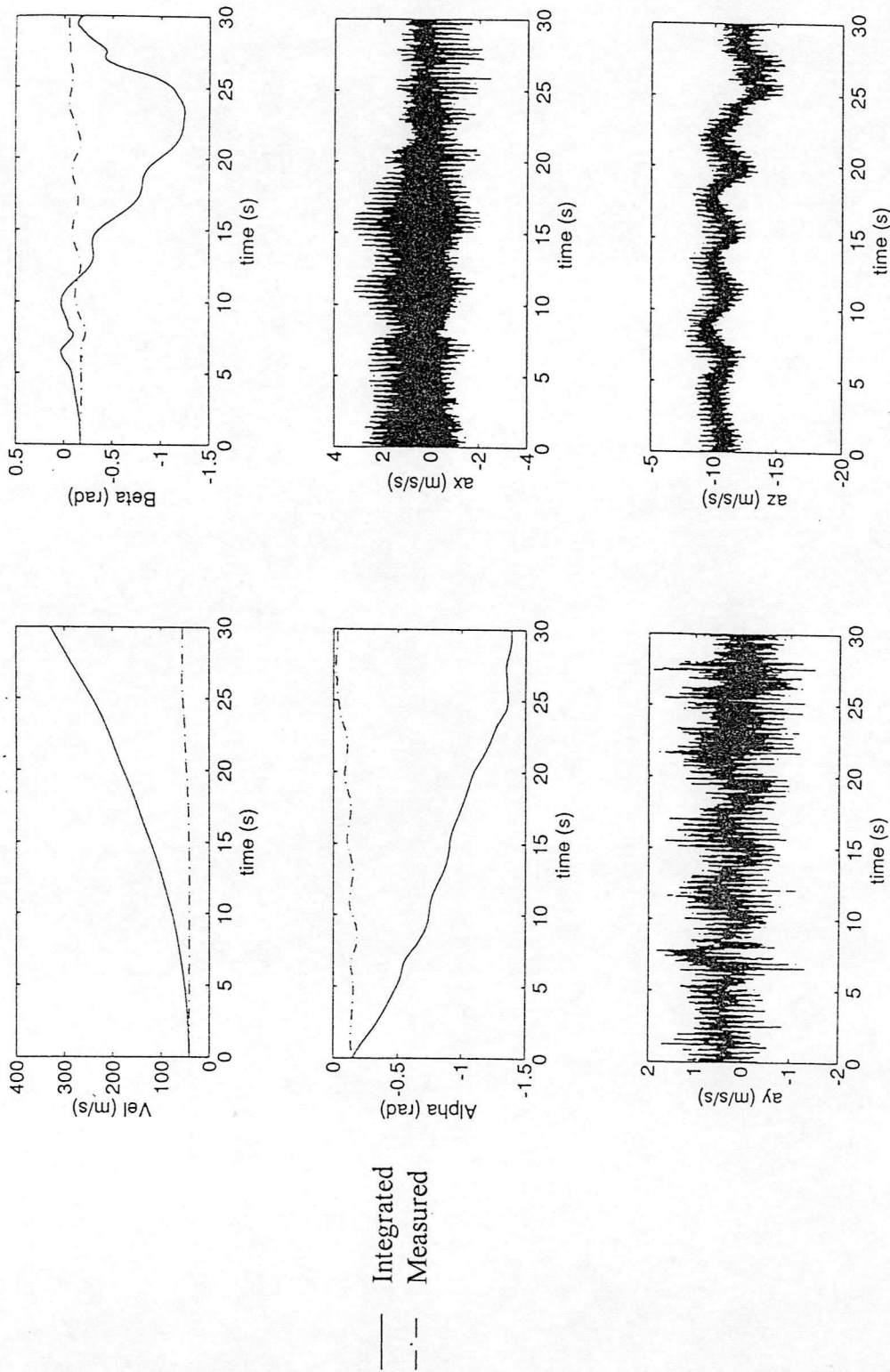
Figure A5.5 Correlation Before Velocity Pass is Performed

— Integrated
-·- Measured
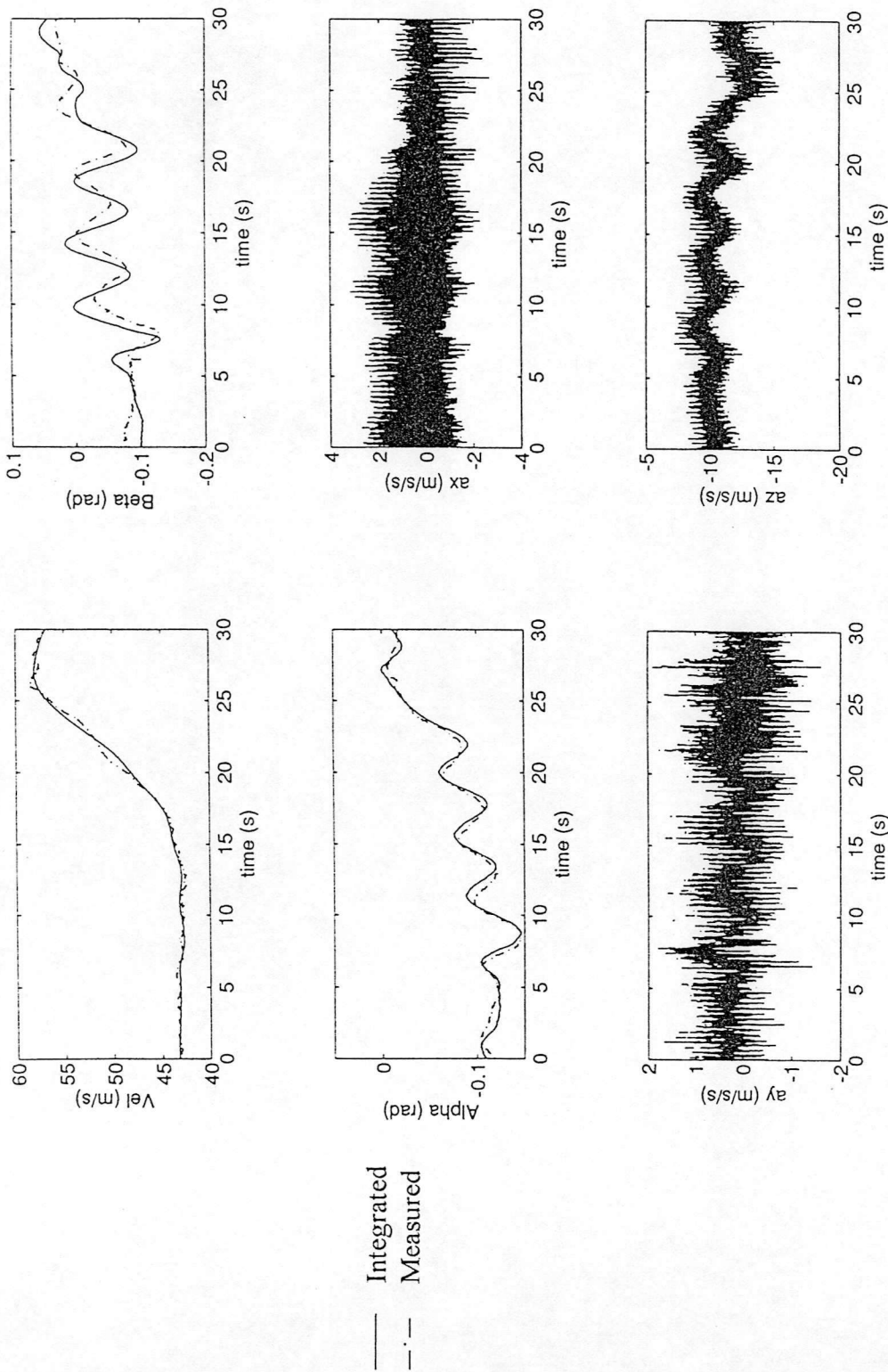
Figure A5.6 Correlation After Velocity Pass Has Been Performed
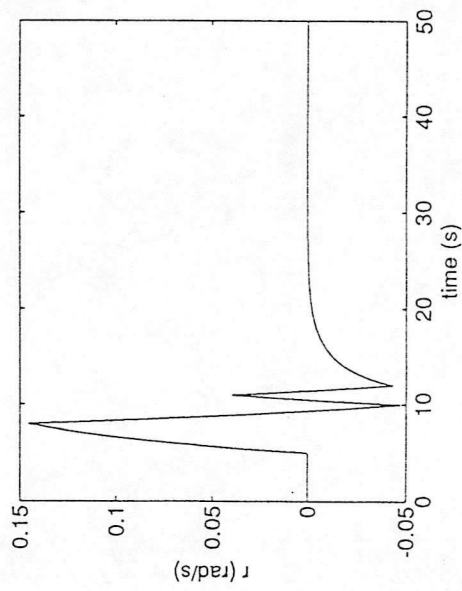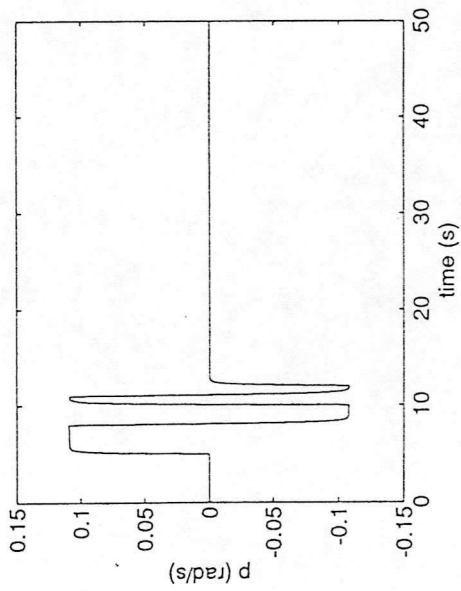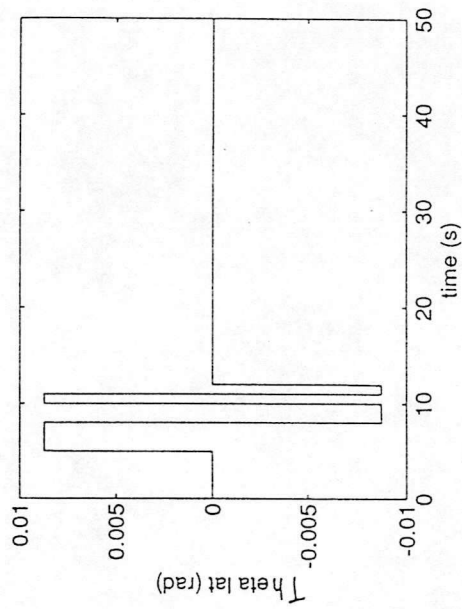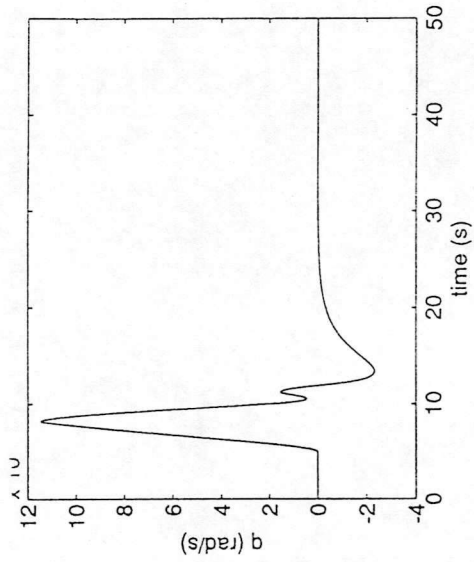
Figure A5.7 "Measured" Input/Output Signals from 3 State - Single Input Linear Model
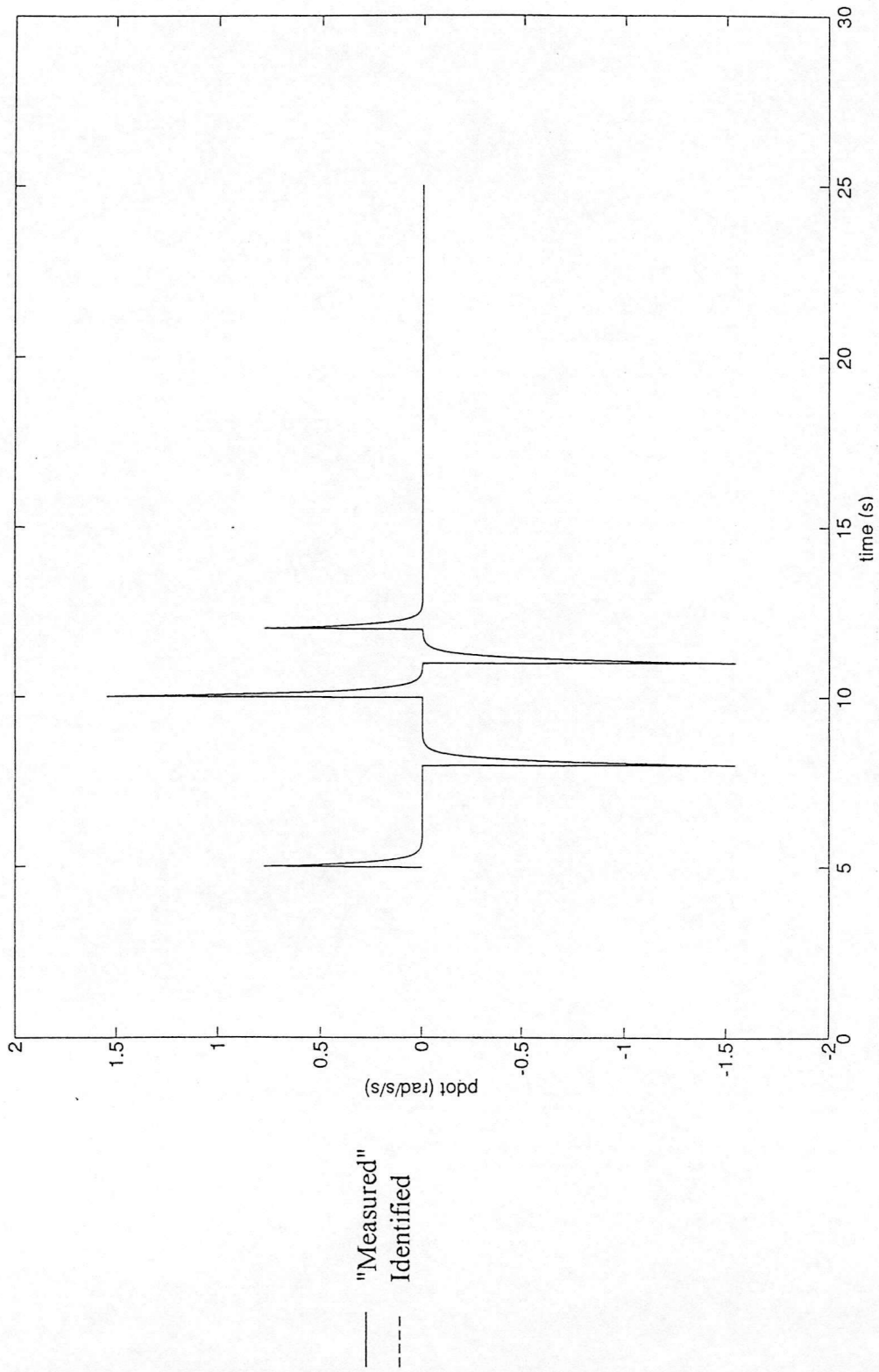
Figure A5.8 Comparison Between Identified and "Measured" $\dot{p}(t)$ With No Noise Present
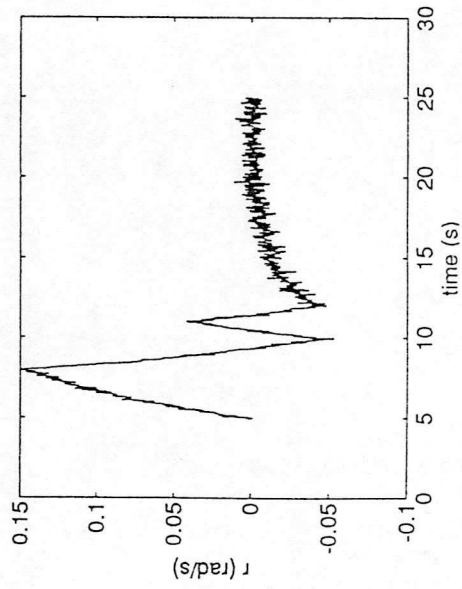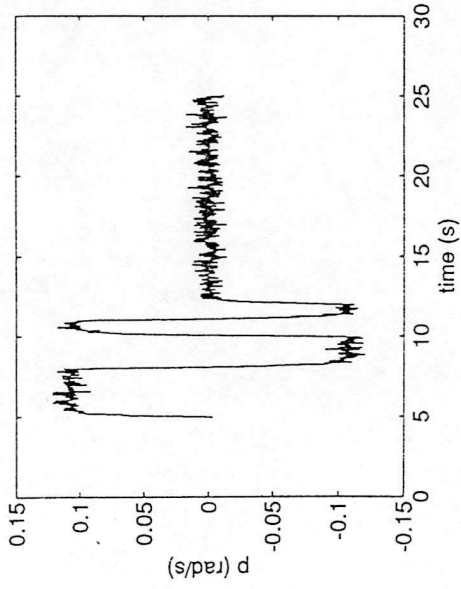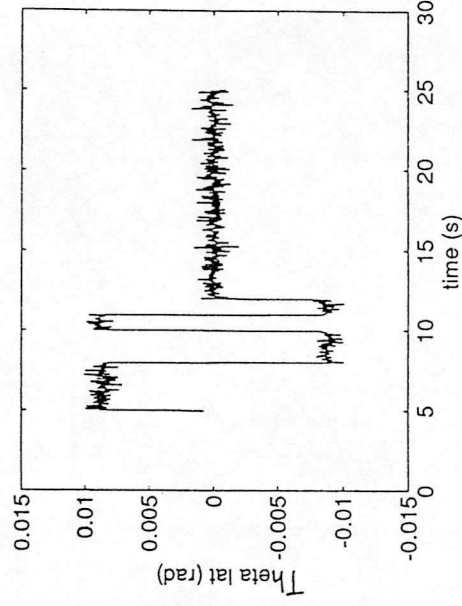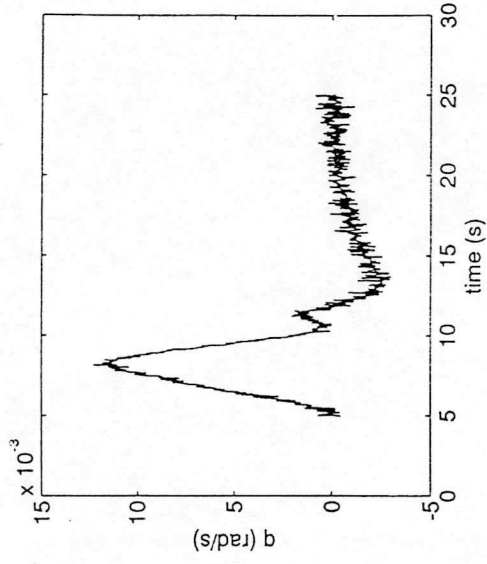
Figure A5.9 "Measured" Input/Output Signals from 3 State – Single Input Linear Model with Noise Added
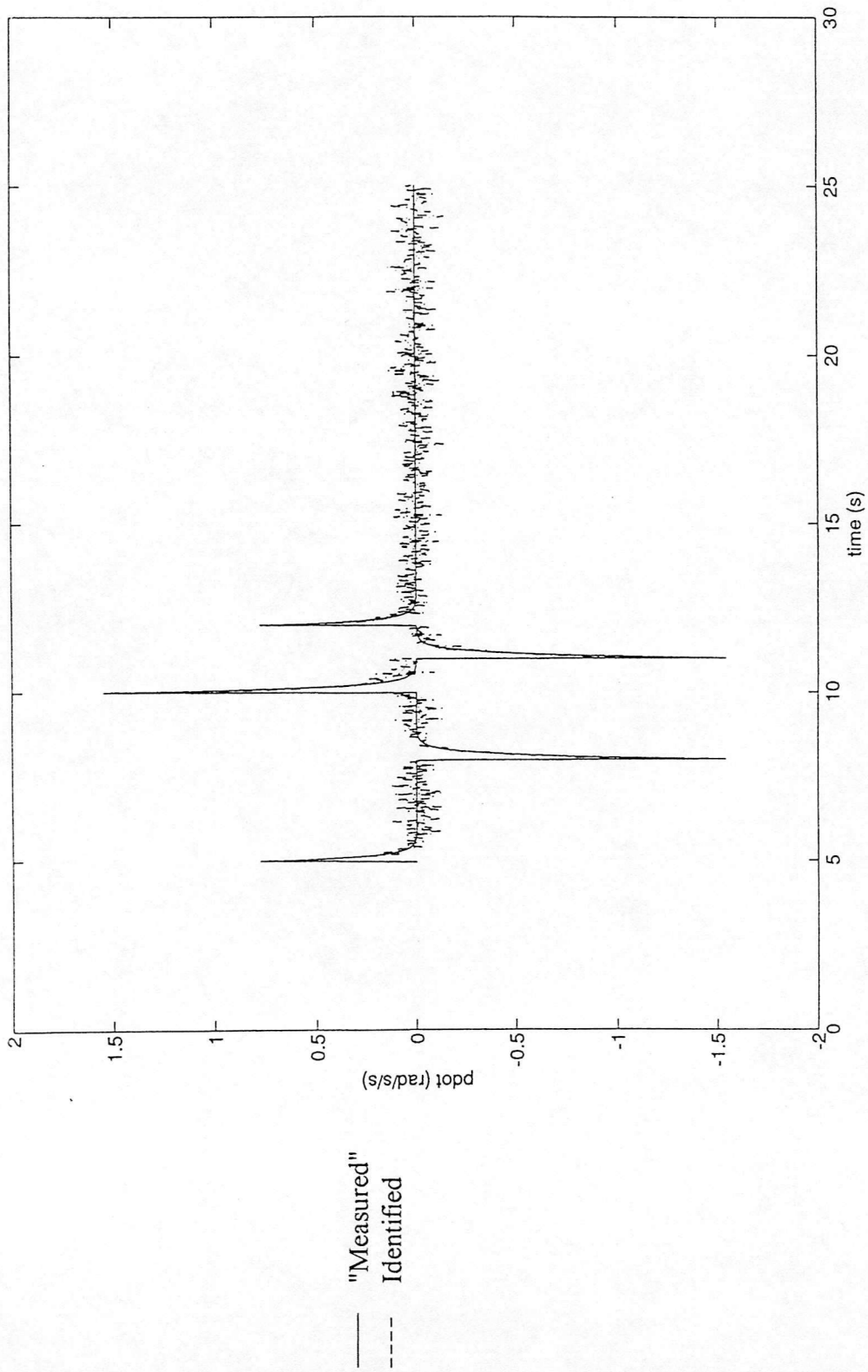
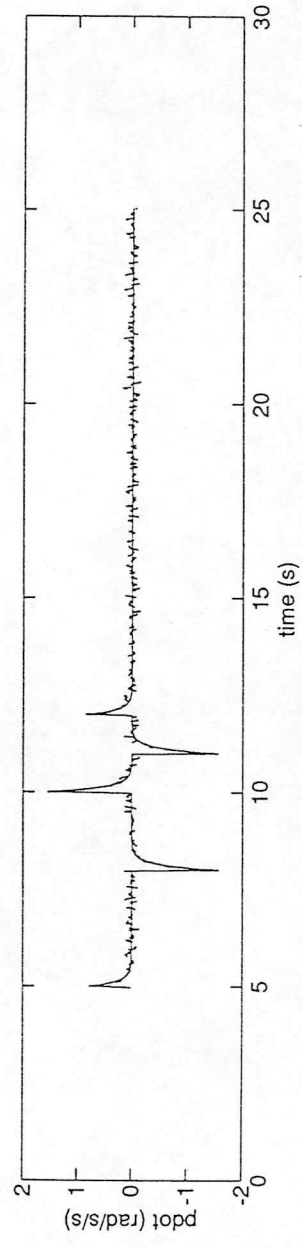Figure A5.10   Comparison Between Identified and "Measured" $\dot{p}(t)$ With Noise Present
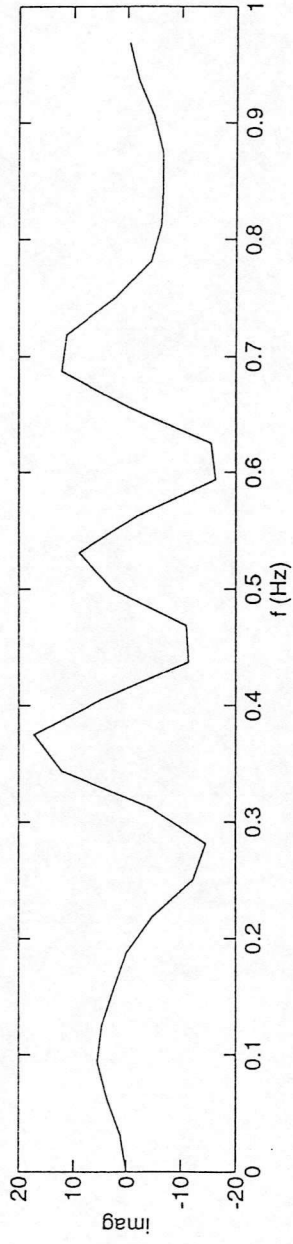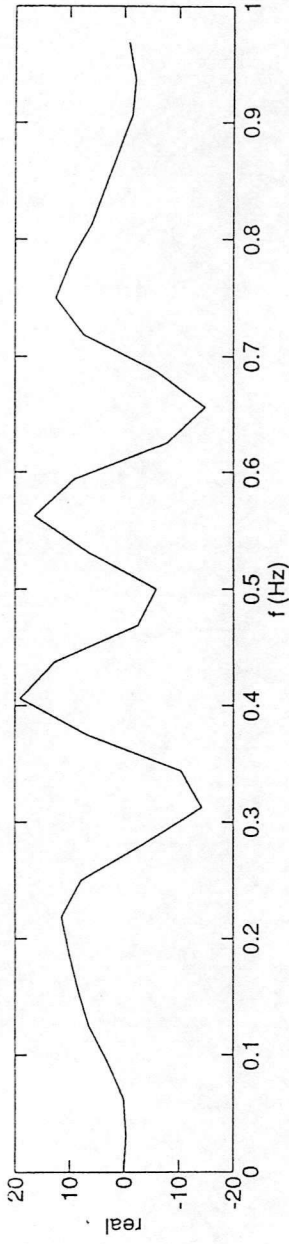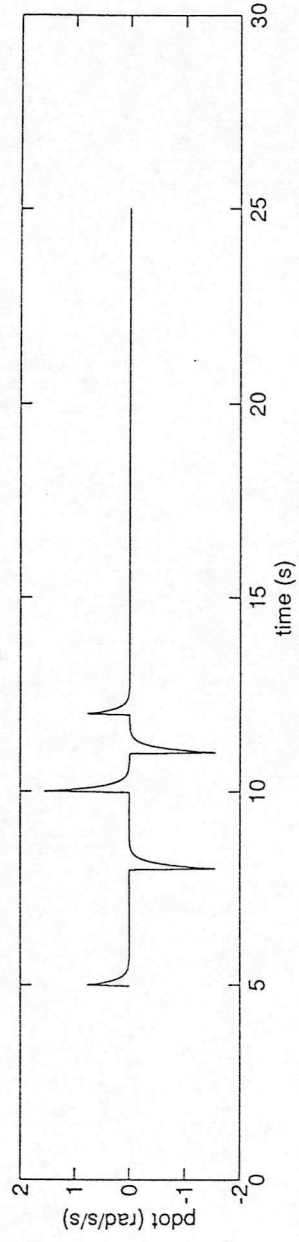
Figure A5.11   Comparison Between Identified and "Measured" $\dot{p}$ With no Noise Present
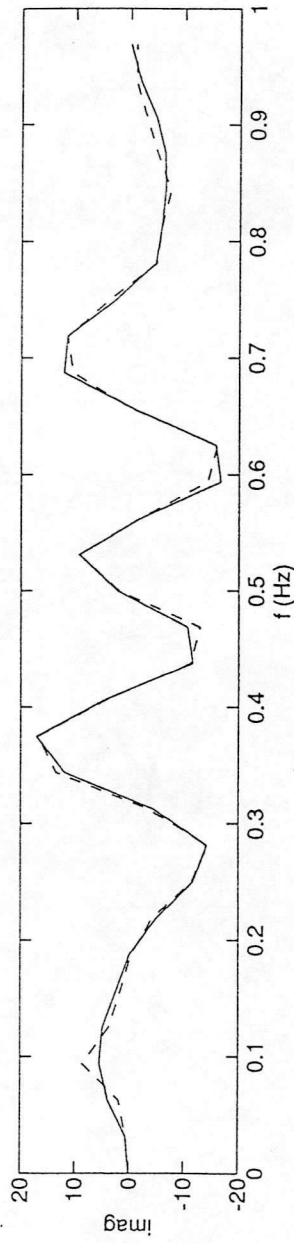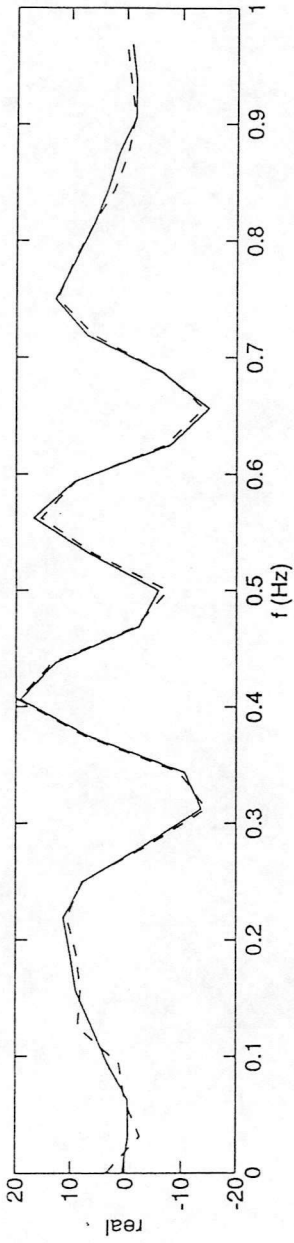
Figure A5.12   Comparison Between Identified and "Measured" $\dot{p}$ in the Presence of Noise
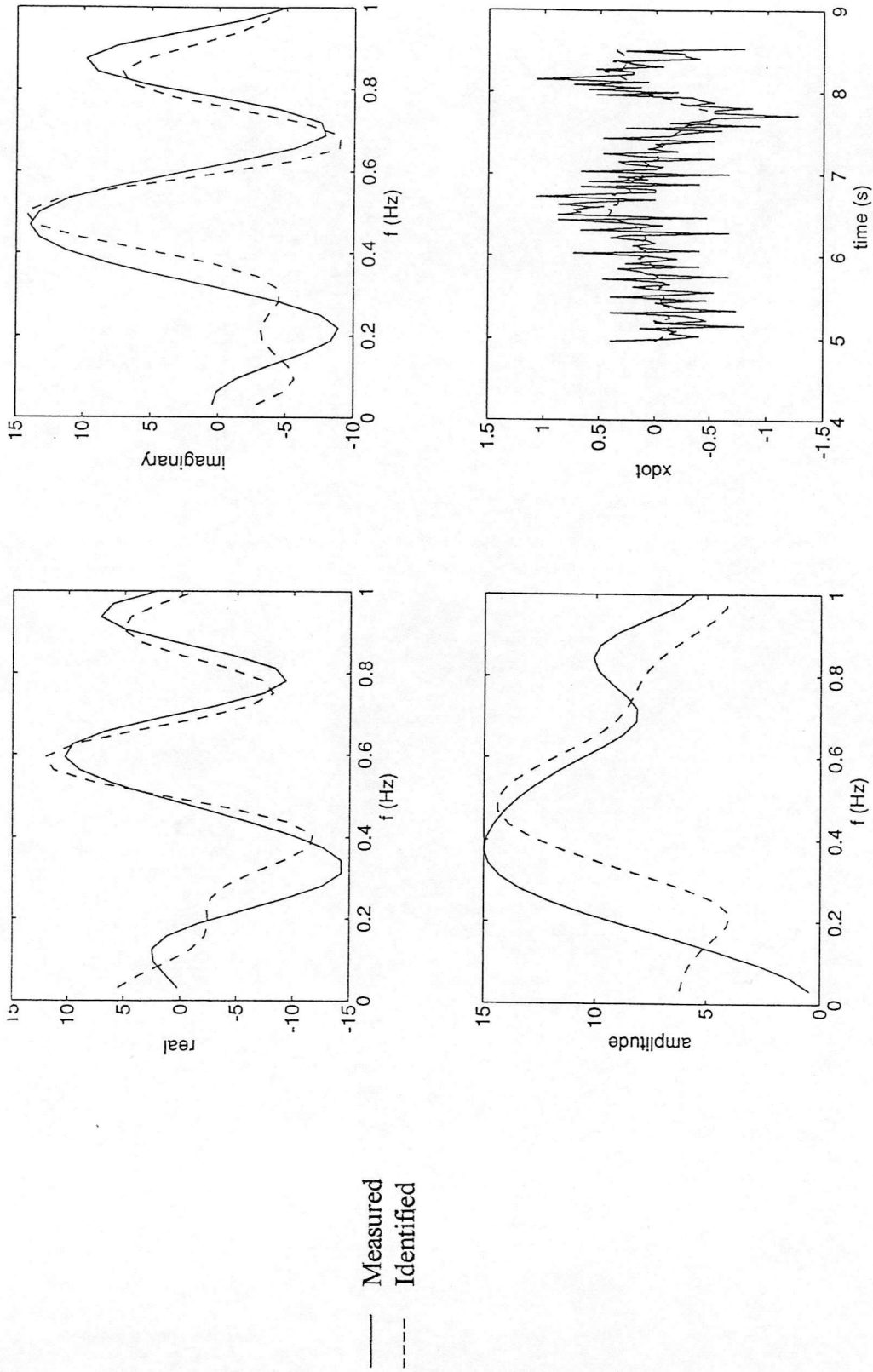
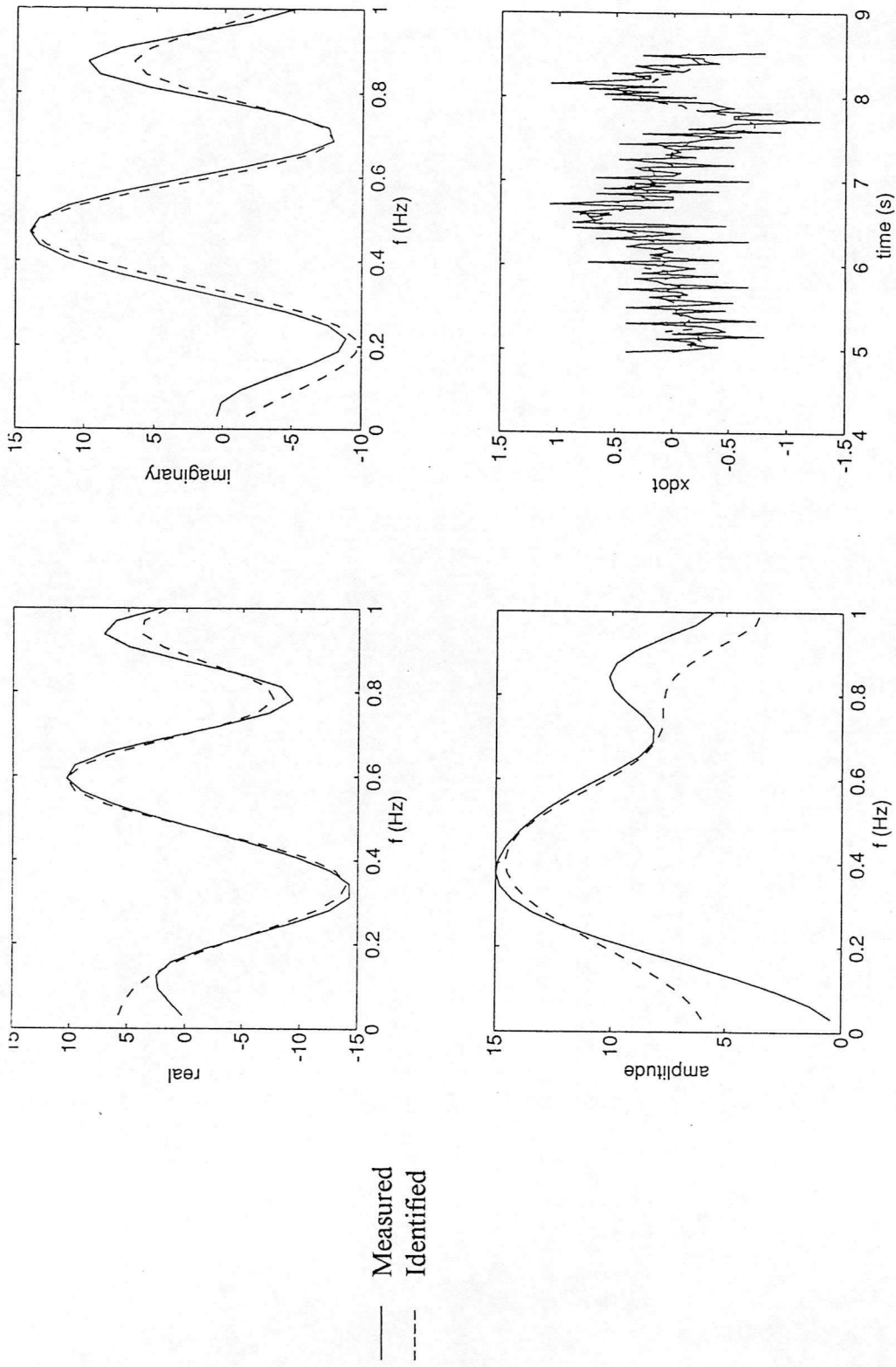Figure A5.13   Comparison Between Identified and Measured $\dot{p}$ Using Favoured 2 State Model Structure

Figure A5.14   Comparison Between Identified and Measured $\dot{p}$ Using 4 State Model Structure

Measured ———
Identified - - - -